EXPERIMENTAL STUDY OF DRAG FROM A

FLUTTERING FLAG

By

ADAM MARTIN

Bachelor of Science

Oklahoma State University

Stillwater, Oklahoma

2003

Submitted to the Faculty of the
Graduate College of the
Oklahoma State University
in partial fulfillment of
the requirements for
the Degree of
MASTER OF SCIENCE
May, 2006

EXPERIMENTAL STUDY OF DRAG FROM A

FLUTTERING FLAG

Thesis Approved:

Dr. Peter M. Moretti
Thesis Adviser

Dr. Andrew S. Arena

Dr. Frank W. Chambers

Dr. A. Gordon Emslie
Dean of the Graduate College

ACKNOWLEDGEMENTS

TABLE OF CONTENTS

LIST OF FIGURES

NOMENCLATURE

A Characteristic Area normal to flow field

C Chord length

C_D Drag coefficient

D Cylinder diameter

F_D Drag force

F_L Lift force

F_{Dp} Pressure drag force (form drag)

F_{Dv} Viscous drag force (skin friction)

f_{Hz} Flutter frequency (hertz)

g Acceleration due to gravity

L Stiff panel length (chord length)

m Mass per unit area

$\dot{m}$ Mass flow rate

p_{atm} Atmospheric pressure

p_1 Free-stream pressure upstream of disturbance

p_s Stagnation pressure where fluid velocity $V = 0$

Δp Pressure difference $\left(p_1 - p_s \right)$

Q Volumetric flow rate

R Universal gas constant for air

Re_D Reynolds number based on cylinder diameter, $U_0 D/(\mu/\rho)$

Re_L Reynolds number based on stiff panel chord length, $U_0 L/(\mu/\rho)$

S Span of web (flag width)

T_{room} Room temperature

U_0 Free stream fluid velocity

v Local fluid velocity

x Direction parallel to free-stream air velocity

y Direction normal to free-stream air velocity

μ Dynamic viscosity of air

mr, μ Mass ratio, $mr = \mu = \dfrac{m}{\rho_{air} C}$

ρ_{air} Density of air

CHAPTER I

INTRODUCTION

1.1   Background

Webs are defined as continuous, strip-formed, flexible materials such as paper, metal foils and polymer films. In many web-handling applications it is common that a web will be coated on one side (as in photography film or tape) such that when processing the web, it is necessary to have no mechanical contact on the coated side of the web during processing. One way to process a web in such a case, is with air bars. The web is "floated" and moved along its web line at high speeds. This air-web interacting creates many instability problems when transporting the web quickly through its production line. With increasing operation speed, the speed of the airflow around the web during processing also increases, and flutter occurs. A web can oscillate uncontrollably when one or several parameters dealing with tension, turbulence, and web non-uniformity are not met. Such an oscillation can become violent very quickly, often tearing the web. This occurrence is catastrophic in the production industry, where an entire web line will be shut down, cleaned, and restrung, resulting in significant "down" time and financial loss.

Another common instability problem that occurs in high-speed printing operations is sheet flutter, sometimes called "flag flutter". Unlike web flutter, sheet flutter has a

short chord length, and is unsupported at one or both ends. In printing presses, when a continuous web is cut into sheets (leaflets), moments of flutter instability are common when the sheet is cut or during its non-contact (floated) travel to the stack, where undesirable touchdown or jamming can occur. With typical newsprint machines running as fast as 1800 m/min (30 m/s), unsightly flutter can cause huge pileups and substantial production downtime. *Watanabe* (2002) provides detailed diagrams and explanations of the printing process. Through the efforts of many researchers studying such flutter phenomena, it hoped that critical operational parameters can be applied in industry from what work has been done to understand and predict the negative flutter phenomenon.

1.2   Objectives and Scope of Study

Flutter instability has been studied in varying degrees of detail and emphasis. Some studies have emphasized material dimensions, others on various material properties, yet others on mode deflections. Most studies have been conducted in a manner that study a very wide range of materials, dimensions, and operating conditions in generalized detail to understand the physics, and/or to look for underlying trends. Additionally, it appears that most studies have been conducted in small-scale wind tunnels using small specimen samples. This experiment is likely the most elaborate to date for a single test specimen, with a dedicated wind tunnel and measurement system designed for the purpose of flutter experimentation. After preliminary trial and error wind tunnel runs, a suitable specimen was found that would flutter consistently in two dimensions, (no irregular 3-D deflection modes) over a wide wind tunnel velocity range. This study focuses its attention on this successful specimen, and seeks to understand the

induced component of drag during steady flutter oscillations. Additionally the characteristics of the flutter mode (frequency, phase, amplitude, and wavelength) are important and have only been partially uncovered by other researchers. The main objectives of this study are listed as follows:

(1) To experimentally verify the components of drag for a fluttering specimen.

(2) To relate characteristic mode properties (frequency, phase, amplitude, and wavelength) and investigate their role with changing material stiffness.

(3) To qualitatively describe the physics of flutter by relating experimental results and compare closed form theoretical models with experimental results.

This study does not attempt to compare a wide range of fluttering specimens, but to accurately and completely study one consistent flutter case. Because this is an experimental study, detailed theoretical work will not be discussed, however it should be noted that most theoretical analysis to date has been done via extensive numerical simulation. To this avail, few closed form approximations and/or experimental correlations have been presented.

1.3   Methods of Study

To understand the effects of dynamically induced tension in a fluttering specimen we can build off classical studies of drag. First we can mathematically quantify the drag force on our attachment pole, "flag pole", by solving the classical drag problem of a cylinder subject to cross flow; perpendicular to the pole's axial axis. This first test primarily serves as a check to validate the accuracy of our measurement system with that of a classical solution. Secondly, we can add a rigid vane (a stiff panel incapable of

flutter) to the attachment pole and measure the drag force at the pole to quantify the combined effects of pressure drag (from the flagpole) and minute viscous drag (skin friction from the rigid panel). By studying the effects of a rigid panel attached to the flagpole (an experimental constant for all flutter tests) the effect of the combined pressure (form) drag can be accessed. Furthermore, the dominance of pressure drag over viscous drag can be confirmed. With a baseline measurement of the "rigid" panel, we can attach a flexible web material (flag) with the same dimensions and note the change of drag. The difference between the drag of the flag specimen, to that of the rigid panel is the dynamically induced drag.

CHAPTER II

LITERATURE REVIEW

The literature relevant to the present study comes from various authors presenting analytical and experimental results of the "flag flutter" phenomenon. This topic has been studied in detail, but still the sometimes random phenomena of flutter poses many unknowns. Over the years however, many researcher have confirmed and reported some of the same fundamental observation and experimental trends. This chapter will present some of the results of past and help provide an underlying understanding of flutter and the drag it creates.

2.1   Flutter phenomena

Flutter phenomena changes with varying specimen dimensions and "aspect ratios". The widely accepted (non-dimensional) definition of a specimen's relative span and chord dimension is called the "aspect ratio".

$$\text{Aspect Ratio} \ = \ \frac{Span}{Chord} \ = \ \frac{S}{C}$$

This definition is made clear in Figure 1, where the aspect ratio is shown among other terminology that will be used throughout this paper.
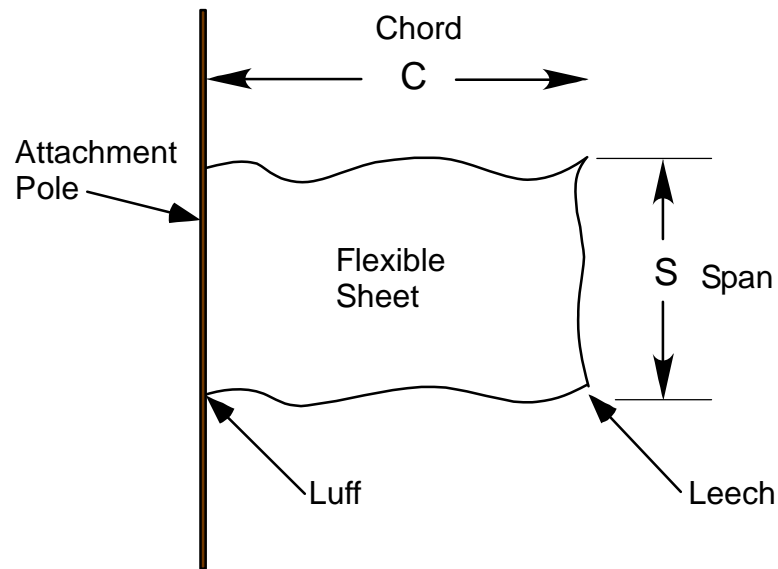
Figure 1. Flexible sheet diagram illustrating span and chord length

In addition to aspect ratio, a common non-dimensional mass property, called mass ratio, is frequently used to categorize a specimen's mass when comparing multiple test specimens with varying aspect ratio parameters

$$mr = \mu = \frac{m}{\rho_{air} C}$$

where :
$m =$ mass per area
$\rho =$ air density
$c =$ chord length

<u>Fundamental Trends</u>

To review the underlying physics of what has been learned from flag flutter studies of past, a compilation of several fundamental research trends is presented below in diagram form with underlying conclusions stated below the diagram.
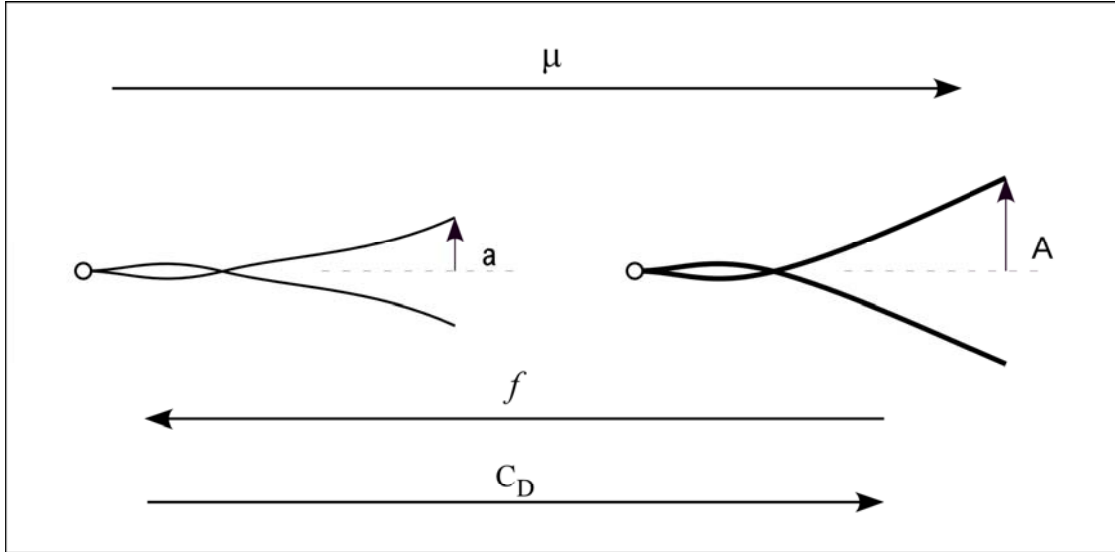
Heavy flags oscillate at larger amplitudes, but at lower frequencies. Heavier flags yield larger drag coefficients.
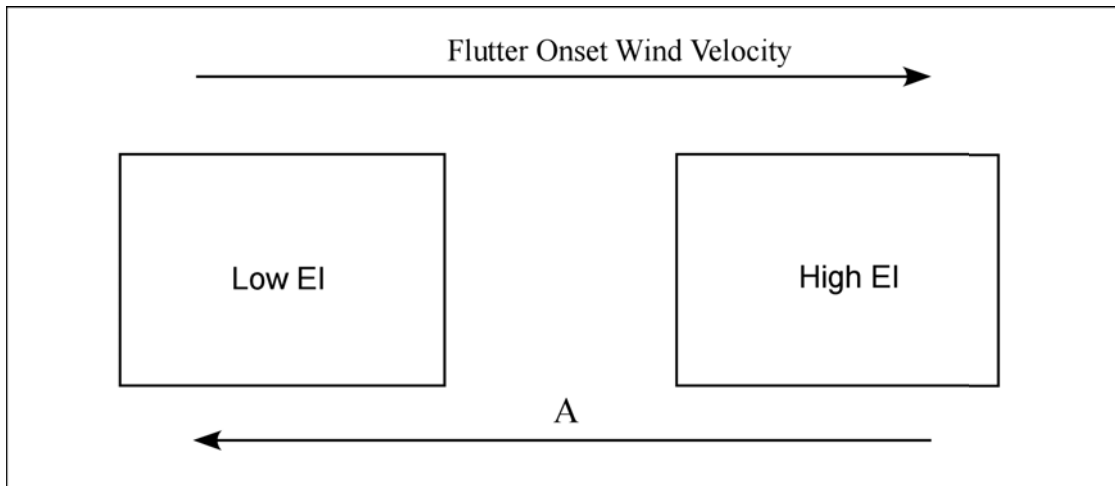
Flags with higher structural stiffness require higher wind speeds to initiate flutter and flutter at lower amplitudes.
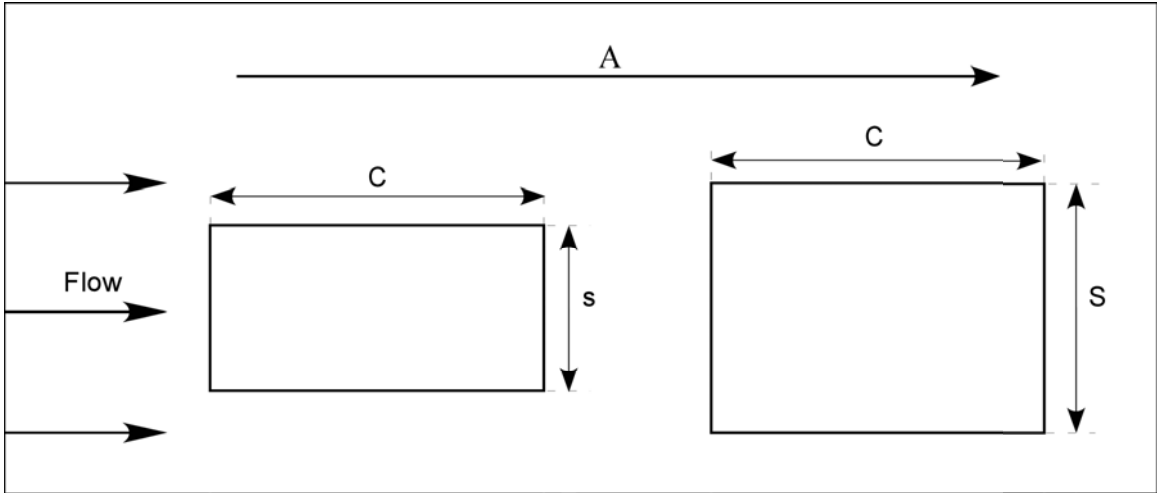
Flags with identical chords but larger spans experience larger amplitudes of

oscillation.
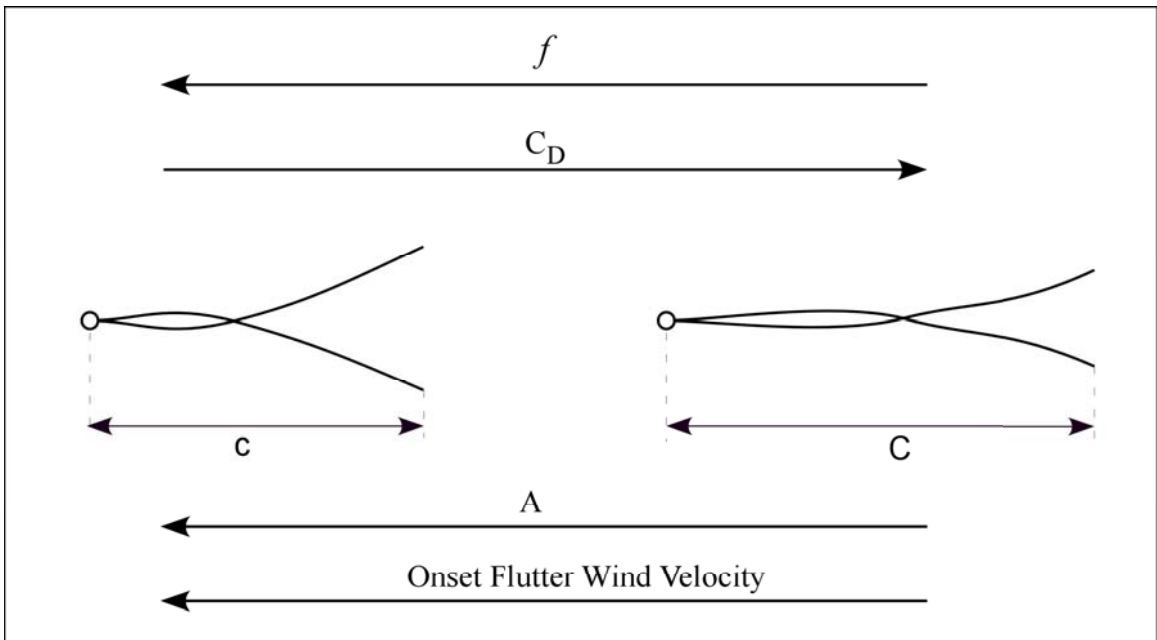
Flags shorter in length (chord) require larger wind velocities to initiate flutter, flutter at a

higher frequency, and have larger amplitudes. Additionally, the drag coefficient has been

found to increase with chord length as a consequence of increased area, mass.

Streamlined Flow Along Specimen

F_D
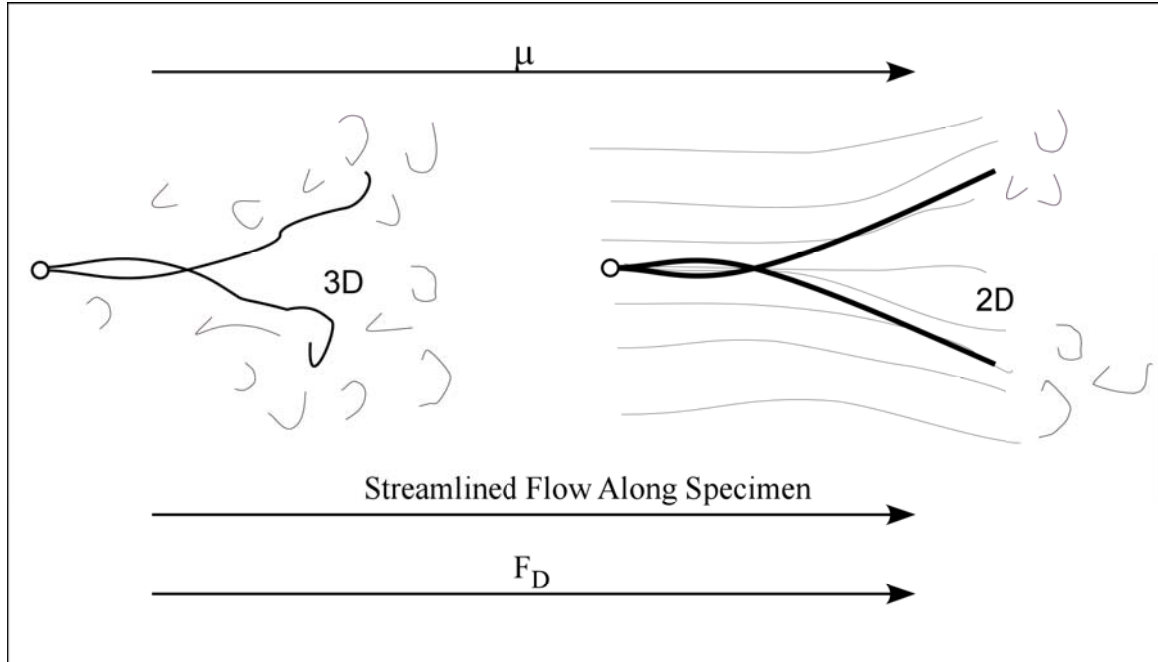
Heavier flag materials experience more streamlined flow along their surface contour and are more stabile (2D oscillations). Additionally, drag force drops when a flag flutters irregularly (in 3D).

Flutter Overview

Many researches have studied the waving motion of flag instability. Many agree that a traveling wave is formed, with the waveform growing in amplitude as it progresses to the leech. *Hoerner* (1958) and *Thoma* (1939 a) suggest that the instability occurs as the boundary layer changes, and flow separation occurs. *Hoerner* suggests it is this flow separation that creates the initial instability; creating the flutter phenomenon. *Taneda* (1968) observed laminar flow along non-fluttering flags with a Karman vortex street being formed behind the specimen. Under flutter conditions however, he observed fluid separation from the specimen surface, and significant twirling in the wake.
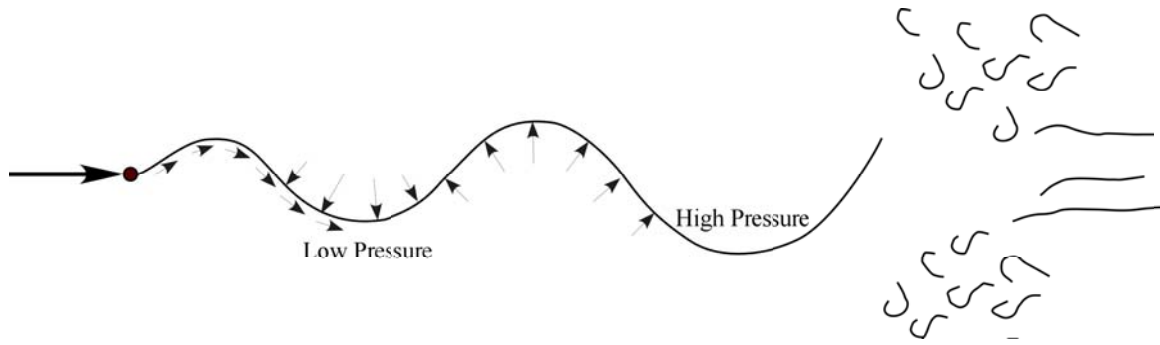
Figure 2. Diagram of a fluttering specimen

Figure 2 above shows high pressure regions in the troughs and low pressure regions over the crests. This intuitive phenomenon was first mentioned by *Thoma* (1939 a), and can help characterize the mechanism of flutter. *Thoma* goes on to suggest that additional pressure feedback from the vortex street causes the extreme whipping phenomenon at the leech. *Uno* (1973) describes the phenomena of tail whip-up by relating classical lift coefficient curves for plates, noting that at a critical angle of attack, the lift coefficient drops dramatically (similar to stall angle in an airfoil). For a discretized model, as the last segment (dC) reaches the critical angle, the lift on that segment is negligible, while the lift on the segment preceding it (having a smaller angle of attack) could be substantial. *Uno* suggests this is the cause of tail-whip, but does not mention the cause of the initial instability.

(*Watanabe*, 2001) performed wind tunnel experiments on thin webs of various materials placed vertically in the wind tunnel. Test results showed that flutter occurred suddenly at a critical wind speed and thereafter the amplitude and frequency was increased with increasing wind speeds. Flutter frequency was found to be hysteric, where

the flag would become stable when ramped down at a wind speed about 25% lower than its critical wind speed. For sheets with a larger chord length, the wind velocity at which flutter occurred was lower than that of sheets of small chord lengths. Additionally *Watanabe* found stiffer materials (EI), required faster wind speeds to initiate flutter than those web materials that were thinner, having smaller mass ratios and structural stiffness. Using a cable wire as the attachment support to conduct flutter experiments, *Watanabe* found no significant air flow separation around the sheet, but significant disruptions in the wake of the flutter (behind the flag). For web materials with relatively large thickness (0.235 mm or greater) there was simple 2D flow (potential), while thinner materials (0.028 mm or less) exhibited complex three dimensional flutter modes. That is for the thicker sheets, the flow appeared to follow the contour of the waving motion, remaining streamlined along the length of sheet and experiencing only small scale vortices downstream of the luff. The thinner sheets however, experience three-dimensional deformation, causing vortices to form along the deforming surface.

Drag Approximations

One of the first researcher to study induced drag, did so out of concern of thrust for airplanes pulling large banners. *Fairthorne* (1930) performed an experimental study of drag for large rectangular flags where most his published data was for a specimen with a span of 4 ft.

Fairthorne found two important variables affecting the drag of flags: 1.) the specimen's aspect ratio relative to the wind velocity. 2.) The areal density of the flag material ω, in $\left(lb / ft^2 \right)$. *Fairthorne* summarizes the results of his experimental study by

providing an empirical correlation equation for the drag coefficient as a function of these parameters. The constant (0.012) in Equation (2-1.1) comes from experimental data for the viscous drag (skin friction coefficient) obtained at Göttingen aerodynamic laboratory, for similar flexible sheets.

$$C_d \approx \frac{\omega}{S \cdot \rho} \cdot 0.39 \cdot \left(\frac{C}{S}\right)^{-1.25} + 0.012 \qquad\qquad (2\text{-}1.1)$$
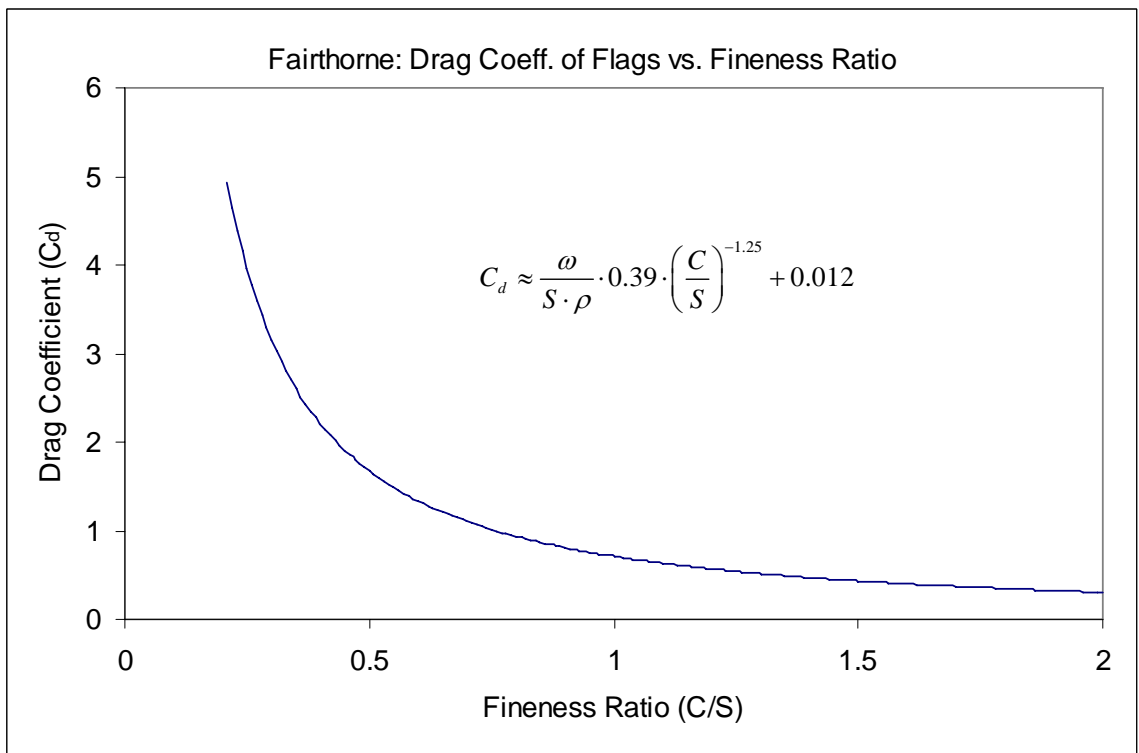
Figure 3. Drag Coefficient vs. fineness ratio as presented by *Fairthorne* (1930)

From Fairthorne's experimental study, he concluded:

1.) Drag of flags is a function of both pressure drag and skin friction
2.) Dynamic drag coefficients increase with increasing area density ω, in $\left(lb/ft^2\right)$
3.) Dynamic drag coefficients increase with decreasing fineness ratios $FR = (C/S)$
4.) The amplitude of oscillation increases with decreasing fineness ratios

5.) Flutter frequency of flag increases with decreasing fineness ratios
6.) Drag coefficients are nearly independent of the free stream Reynolds number for flags of the tested geometric type (fineness ratio).

Shifting the discussion from empirical correlations with approximations deduced analytically from physics; *Moretti* (2003) suggests that the large curvature of the fabric at the leech, as a result of the flutter motion, generates centrifugal forces that induce the largest tension (drag) force at the attachment. From *Thoma's* paper (1939 b) of tension in a rope, Moretti postulates a closed form time averaged approximation of drag for a fluttering flag.

Thoma (1939 b) expresses the average tension per unit segment (ds) in a rope as:

$$\frac{d\bar{T}}{ds} = -\frac{m_f}{2} \cdot \frac{d}{ds}\left(\bar{V}^2\right) \tag{2-1.2}$$

Upon integration, and applying the bounds over a flag length $(s = L)$:

$$\bar{T} = \frac{1}{2} m_{flag} \bar{V}^2_{leech} \tag{2-1.3}$$

which is to say that the largest effect of tension comes from the kinetic energy dissipation at the leech, where the velocity is a maximum. *Moretti* goes on to approximate the average tension at the luff (attachment pole), by differentiating an assumed deflection profile (waveform) and inserting the velocity (evaluated at the leech) into Equation (2-1.3). Assuming a simplified waveform motion (deflection) as $z = \frac{Ax}{L}\cos(\omega t - kx)$, *Moretti* (2003) predicts the average dynamically induced tension in a flag by Equation (2-1.4).

$$\bar{T} = \frac{1}{4} m_{flag} A^2 \omega^2 \tag{2-1.4}$$

where :

m_{flag} = mass-per-unit-length

A = amplitude at the leech (half)

ω = circular frequency (rad/s)

For stiff panels (incapable of flutter) drag is produced from skin friction acting along both surfaces. *Hoerner* (1958) found the skin friction drag coefficient to be very low; typically in the order of $C_d \approx 0.01$. The dynamic effect of a fluttering flag however, has proven to gives rise to much larger drag forces than just skin friction alone. *Moretti* (2003) postulates that not only is the dynamic tension significantly larger, but is also distributed much more broadly over the specimen length. Comparing the relative contribution and distribution of drag per unit length produced from a flexible specimen, *Moretti* creatively non-dimensionalizes laminar skin friction as:

$$\frac{T}{L\rho_{air}U^2} \cong 1.328\sqrt{\frac{\mu_{air}/\rho_{air}}{UL}} \bullet \left[\frac{\sqrt{L}-\sqrt{x}}{\sqrt{L}}\right]$$

and the dynamically induced tension distribution from Equation (2-1.4) as:

$$\frac{T}{m_{flag}A^2\omega^2} \cong \frac{1}{4}\left[1-\left(\frac{x}{L}\right)^2\right]$$

The distribution of time-averaged drag from the dynamic approximation theory versus the component of skin friction drag is shown in Figure 4.

14
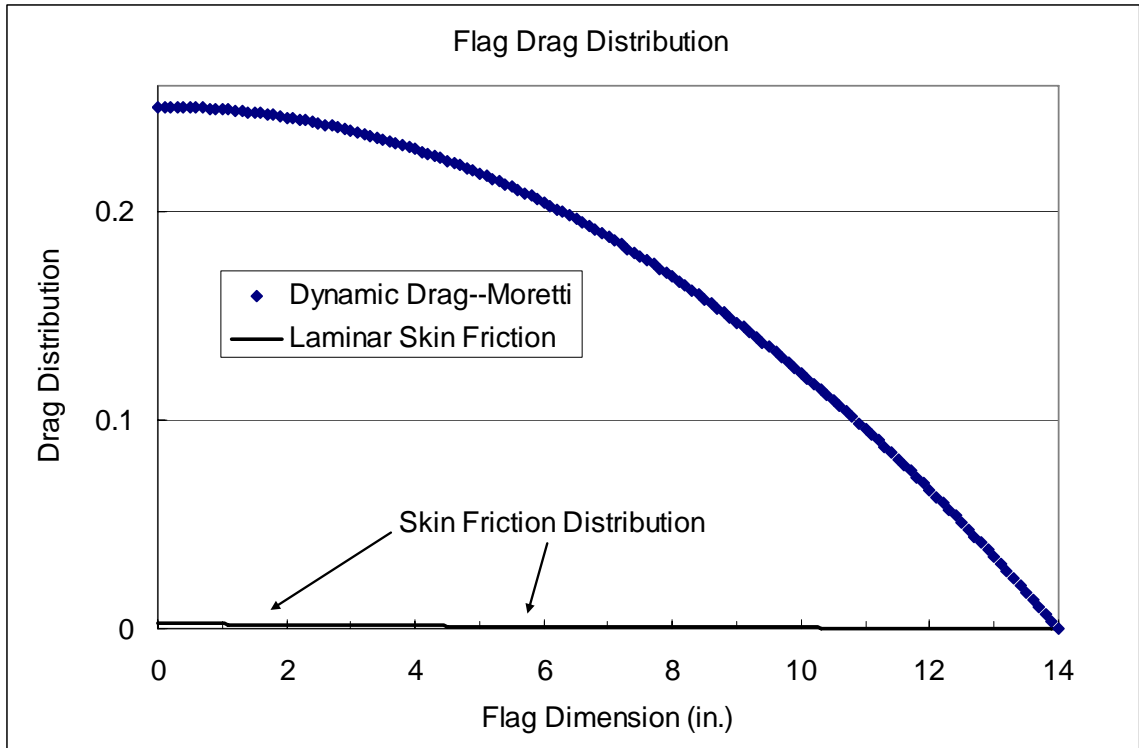
Figure 4. Relative magnitude and distribution of dynamically induced tension vs. skin friction (viscous) drag.

Clearly, the dynamically induced tension prediction yields a much broader distribution of drag over the length of the specimen, with the maximum drag occurring at the attachment pole $(x = 0)$ and tapering to zero at the leech. The drag imposed by viscous skin friction, yields a small spike at the luff and quickly tapers toward zero, thus further confirming the minute contribution of drag in comparison with dynamic approximations.

CHAPTER III

THEORIES

3.1   Fundamentals of Drag and Lift

Classical Drag of a cylinder in a fluid stream

Pressure drag is the drag associated with the pressure disturbance of the fluid as it passes over a body and separates into a turbulent wake. Pressure drag is a function of the shape/orientation of the body, the surface quality of the object, and the fluid's Reynolds number. Pressure drag is sometimes referred to as form drag, because significant drag variations can occur by changing the form (shape) of the object *Mott* (2000). A streamlined object effectively changes the separation point of the boundary layer, creating a smaller wake, and thus reducing the net drag force. Additionally, the roughness of the objects surface can significantly affect the separation point of the fluid at different Reynolds numbers. A rough surface finish changes the nature of the fluid boundary layer from laminar to turbulent at lower Reynolds numbers, moving the separation point further back on the body, decreasing the size of the turbulent wake, and thus decreasing the drag force at lower Reynolds numbers. A second component of drag, friction drag, can be found by integrating the shear stress distribution along the object's surface. It is this shearing force, between the object and the fluid stream, that decelerates the fluid near the object's surface, thus creating a boundary layer. At very low Reynolds

numbers, $(\mathrm{Re} < 1)$ the drag is due almost entirely to friction, while at higher Reynolds numbers flow separation and the turbulence in the wake of the object make pressure drag predominant *Mott* (2000). Classically, drag forces are expressed in the form

$$F_D = C_D \left(\frac{1}{2} \rho U_0^{\,2} \right) A \qquad (3\text{-}1.1)$$

where:
C_D = drag coefficient
ρ = density of the fluid
U_0 = freestream fluid velocity
A = characteristic area of the body

The drag coefficient (C_D) is a dimensionless number based on the shape of the body and its orientation to the fluid stream. The characteristic area (A) is the effective frontal area perpendicular to the free stream flow. The combined term $\left(\frac{1}{2} \rho v^2 \right)$, is called the dynamic pressure and comes from Bernoulli's equation. Consider the classical case of a cylinder oriented with its axial axis perpendicular to a cross flow as shown in Figure 5. As the fluid stream hits the surface of the object $(\text{at location } p_s)$, the velocity of the fluid stops thus creating a "stagnation point" and a corresponding stagnation pressure (p_s). This point creates the largest pressure differential from free stream static pressure (p_1).
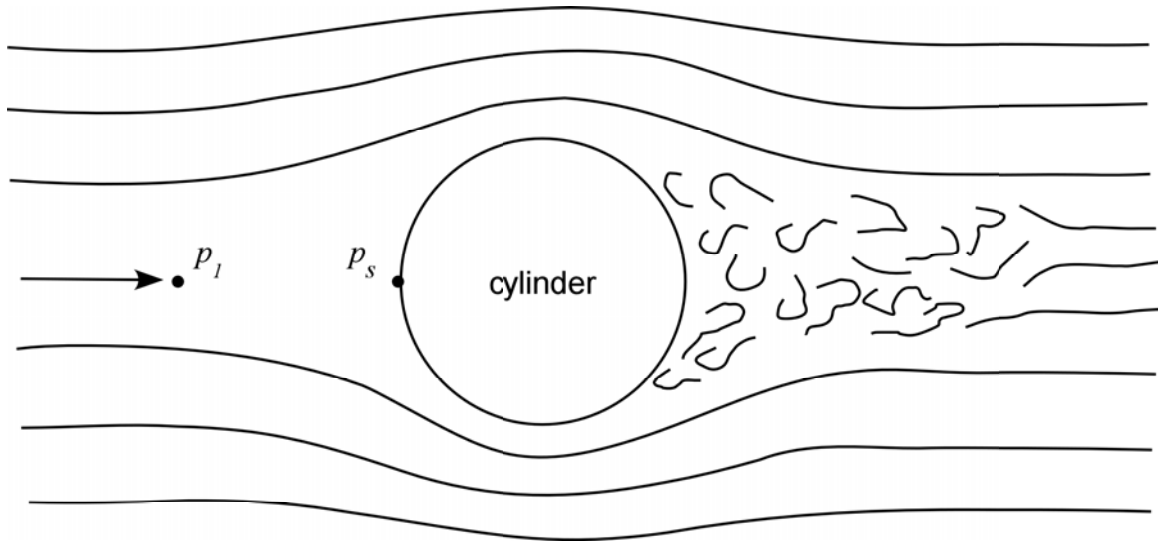
Figure 5 Cross-section of a cylinder in a fluid stream

The relationship between these two pressures can be found from Bernoulli's equation as follows:

$$(1.) \qquad \frac{p_1}{\gamma} + z_1 + \frac{v_1^{\,2}}{2g} = \frac{p_s}{\gamma} + z_s + \frac{v_s^{\,2}}{2g}$$

Where: elevation is constant and the fluid velocity is zero at location s, $\left(v_s = 0\right)$, giving:

$$(2.) \qquad \frac{p_1}{\gamma} + \frac{v_1^{\,2}}{2g} = \frac{p_s}{\gamma}$$

Solving for the stagnation pressure and substituting $\rho = \dfrac{\gamma}{g}$, the stagnation pressure (total pressure) is greater than the static pressure in the free stream by the magnitude of the dynamic pressure $\left(\dfrac{1}{2}\rho v_1^{\,2}\right)$.

$$(3.) \qquad p_s = p_1 + \frac{1}{2}\rho v_1^{\,2} \qquad\qquad\qquad\qquad (3\text{-}1.2)$$

The increased pressure at the stagnation point and the sudden pressure drop in the fluid wake behind the object creates an unbalance of pressures around the body, thus creating a reactive force opposing the fluid motion. The magnitude of this drag force (pressure drag) not only depends on the free stream static pressure (p_1) and the stagnation pressure (p_s), but also on the pressure in the wake of the object. Because the turbulence of the fluid in the wake is unsteady and hard to predict, a constant coefficient (a drag coefficient based on experimental data, C_D) is used to adjust drag calculations. Experimental drag coefficient data is commonly presented in texts as a plot of the drag coefficient on the ordinate versus the Reynolds number on the abscissa. The Reynolds number calculation is unique to the geometry of the object. Instead of using the fluid conduit diameter or hydraulic radius to compute the Reynolds number, the dimension of the body parallel to the fluid stream is used when referencing drag coefficient data from charts.

$$\text{Re} = \frac{U_0 D}{(\mu/\rho)} \tag{3-1.3}$$

where :
$\rho = $ density of fluid stream
$U_0 = $ free stream fluid velocity
$D = $ characteristic dimension (diameter for cylinders)
$\mu = $ dynamic viscosity of fluid steam

As is evident from Equations (3-1.1) and (3-1.3), it becomes critical to understand the properties of the fluid (air), which consequently is time dependent. As with all gases,

the properties of air change with temperature and altitude. Using a mercury barometer, the local atmospheric pressure can be computed as:

$$p_{atm} = \rho_{Hg}(g)h_{barometer} \qquad \text{(3-1.4)}$$

where:

ρ_{Hg} = density of mercury

g = gravitational acceleration

$h_{barometer}$ = height of mercury

and with the local atmospheric pressure, the density of air can be computed as:

$$\rho_{air} = \frac{p_{atm}}{RT_{abs}} \qquad \text{(3-1.5)}$$

where:

p_{atm} = local atmosheric pressure

R = univeral gas constant

T_{abs} = absolute temperature

The Sutherland equation can be used to compute the dynamic viscosity of the air by measuring the local temperature.

$$\mu_{air} = \frac{b\sqrt{T_{absolute}}}{\left[1+\left(\dfrac{S}{T_{absolute}}\right)\right]} \qquad \text{(3-1.6)}$$

where:

$b = 1.458 \times 10^{-6} \dfrac{kg}{m-s-K^{1/2}}$

$S = 110.4\ K$

$T_{absolute}$ = absolute local temperature

An excel spreadsheet calculator (courtesy of F.W. Chambers), was used to compute air properties from barometer temperature and pressure readings. This sheet and related

formulae are shown in Appendices I-J. Combining the physical properties from above, the drag force on a cylinder subject to a cross flow is defined as:

$$F_{D_{cylinder}} = C_D \left(\frac{1}{2} \rho_{air} U_0^{\ 2} \right) DL \qquad (3\text{-}1.7)$$

where :

$\mathrm{Re}_D = \dfrac{U_0 D}{(\mu/\rho)}$ for circular cylinder

$C_D = $ drag coefficient $\left[C_D = f\left(\mathrm{Re}_D\right) \right]$ (from experimentally published data)

$\rho_{air} = $ density of fluid stream

$U_0 = $ free stream fluid velocity

$D = $ diameter of cylinder (flag pole)

$L = $ length of cylinder normal to fluid stream

From tables, a smooth cylinder has a drag coefficient $C_D \approx 1.0$ for $10^3 \leq \mathrm{Re}_D \leq 10^4$. Figure 6 compares theoretical drag data for a classical cylinder in a cross-flow with that measured experimentally for the attachment pole. The attachment pole; with diameter $D = 0.375 \ in = 0.0127 \ m$, and length $L = 36 \ in = 0.939 \ m$ is a smooth stainless steel rod. A center "half section" of the rod is removable and serves to clamp various test specimens. Screw recesses were filled with putty to keep the round contour and thin scotch tape was placed over the leading edge of joint. A picture of the attachment pole is given in Figure 18 on page 40.
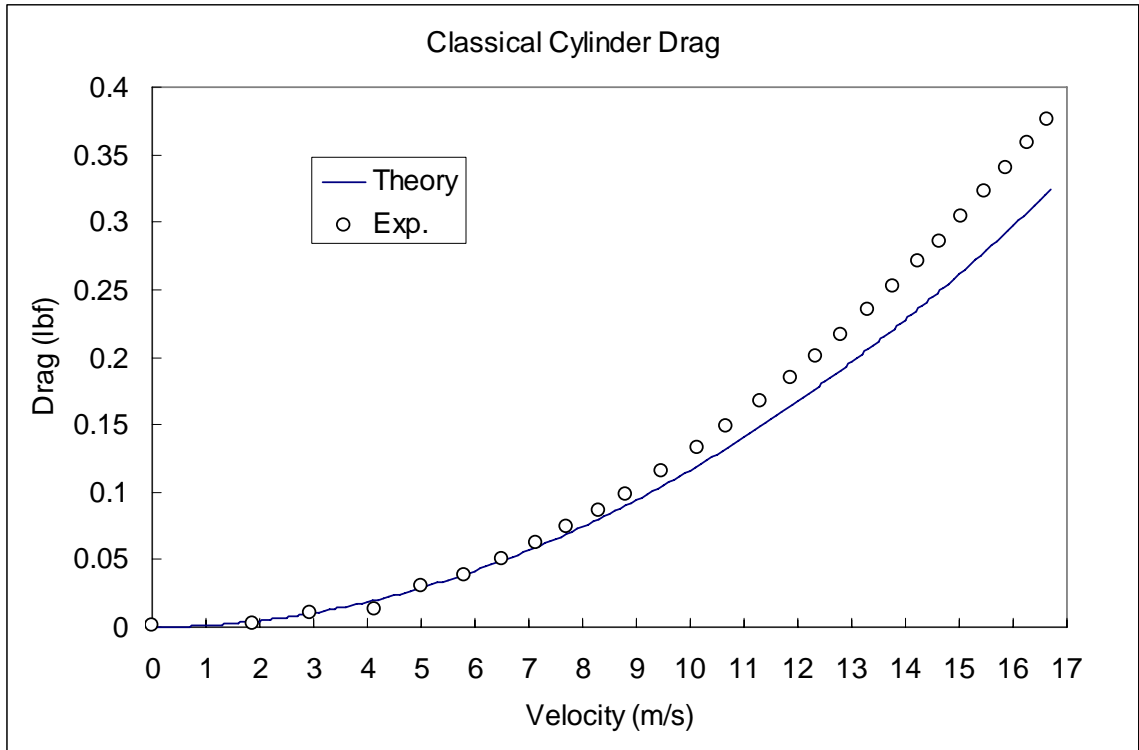
Figure 6. Theoretical and experimental profile of drag vs. velocity for a circular cylinder $\left(C_D = 1.0\right)$

When computing the theoretical drag with $C_D = 1.1$, the experimental drag data agrees very well as shown in Figure 7. This "nudge" in theoretical drag may be realistic considering the imperfection of the 'two-half' flagpole. The significance of this result shows the transducer setup/instrumentation is appropriate, and accurately reproduces theoretically known drag cases. In either case $\left(1 \leq C_D \leq 1.1\right)$, flutter experiments were performed at wind velocities less than 10 m/s, to which both theoretical cases agree very well.
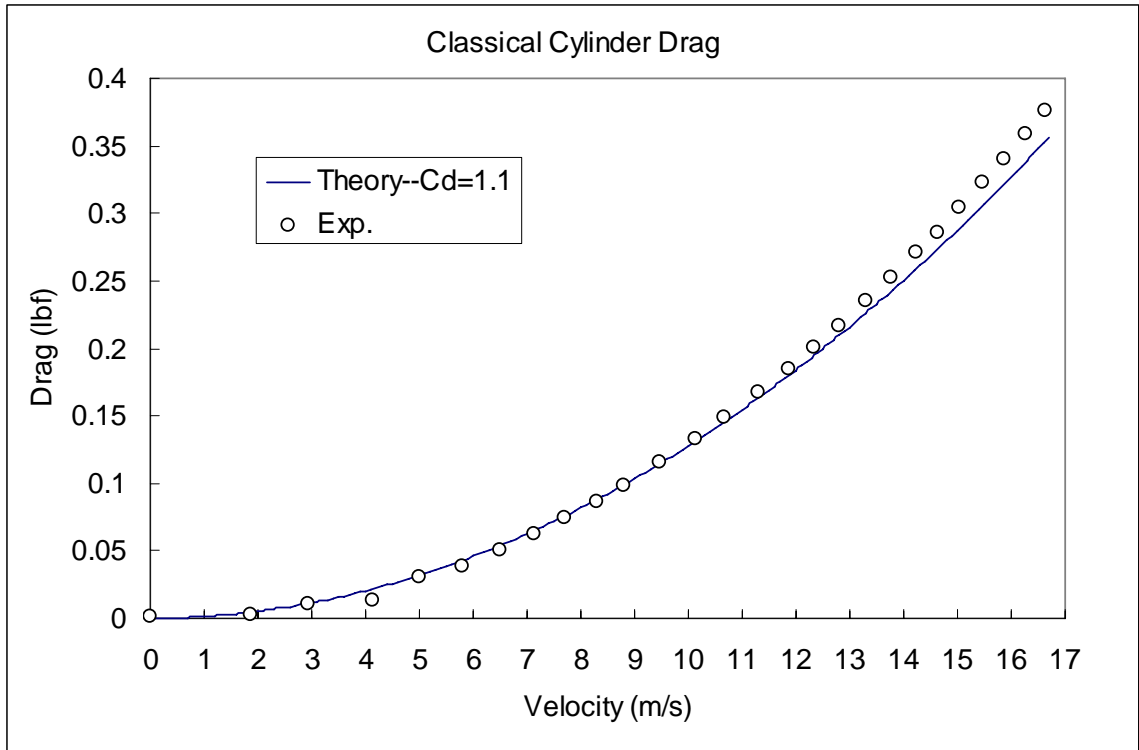
Figure 7. Experimental accuracy with a known drag case

Classical Lift

The drag force in the previous section was defined as the force acting parallel to the fluid stream, and now we consider the component of the force that acts perpendicular to the fluid stream. This lift force is present on objects placed in a fluid stream at an angular reference α, with respect to a characteristic chord. Consider the cross section of an airfoil in a fluid stream as shown in Figure 8.

Induced Drag

Lift

Vector (Net) Drag

Flow

α
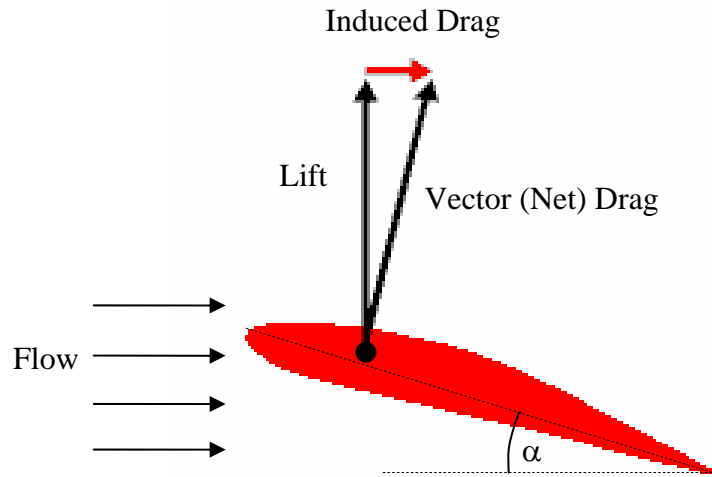
Figure 8. Classical airfoil diagram of forces

The airfoil placed at an "attack angle" α, is subject to two component forces: lift and drag. As the fluid hits the underside of the foil, pressure forces act normal to the surface contour. These normal pressure forces, net drag, are resolved into component x and y forces. The vertical component of force is lift, and the horizontal component is the drag. Both of which, are a result (dependent) of the object's angular orientation to the fluid stream α. It should be emphasized, that the induced component of force is a consequence of lift forces, generated by the fluid stream or other external lift forces.

3.2   Stiff Vane Drag in a Fluid Stream

For the second phase of experimentation, a rigid panel ($\frac{1}{16}$" aluminum sheet), incapable of flutter, was attached to the pole. The panel was oriented such that its planar surface was parallel to the flow stream. In comparison to the cylinder in a cross flow (flag pole only), we anticipate a larger net drag force due to the addition of skin-friction

(viscous drag), caused by the shearing stress within the thin boundary layer along the stationary plate. That is, the net drag force for the rigid panel connected to the flagpole will be a function of pressure drag (form drag from the flagpole), and viscous drag (skin-friction drag from the rigid panel: $(F_D)_{\text{Rigid Panel}} = F_{Dp} + F_{Dv}$. Recall from the previous section, the pressure drag of the flagpole is defined as:

$$(F_D)_{cylinder} = C_D \left(\frac{1}{2} \rho_{air} U_0^2 \right) DL = F_{Dp} .$$

Laminar Boundary Layer

Now we will consider the viscous drag on the rigid panel, F_{Dv}. Because the stiff panel is a streamlined object, we expect the fluid to attach to the surface of the panel reducing the turbulence associated with blunt body objects. This streamlined effect creates a thin film boundary along the surface of the panel, known as the boundary layer. The layer of fluid in the boundary layer has undergone a change in velocity as a result of the shearing stress at the surface. Traditionally, the boundary layer on the flat panel starts at the leading edge of the panel and grows in thickness along the length of the panel until the fluid stream becomes unstable and separated into a turbulent boundary layer. For the traditional case of only a flat panel subject to a flow stream where $\text{Re}_L < 10^5$, and assuming the velocity distribution along the panel does not vary $(dp/dx = 0)$, the frictional resistance (drag) due to viscous shearing in a laminar boundary layer can be computed as follows:

Given the classical relationship of shear stress relating absolute viscosity and the velocity gradient of the boundary:

$$\tau_0 = \mu \frac{du}{dy} \qquad (3\text{-}2.1)$$

The velocity gradient for a laminar boundary layer is approximated as:

$$\frac{du}{dy} = 0.332 \frac{U_0}{x} \operatorname{Re}_L^{1/2}$$

And the shear stress at the boundary becomes:

$$\tau_0 = 0.332 \mu \frac{U_0}{x} \operatorname{Re}_L^{1/2}$$

The shearing force on one side of the plate can be written as:

$$F_D = \int_A \tau_0 dA \quad = \quad w \int_0^L 0.332 \mu \frac{U_0}{x} \operatorname{Re}_L^{1/2} dx$$

$$\left(F_D \right)_{panel} = 0.664 w \mu U_0 \operatorname{Re}_L^{1/2} \qquad (3\text{-}2.2)$$

where :
$w = $ panel width
$\mu = $ dynamic viscosity
$U_0 = $ free stream fluid velocity
$$\operatorname{Re}_L = \frac{U_0 L}{\left(\mu / \rho \right)}$$

A dimensionless shear stress coefficient can be presented as:

$$c_f = \frac{\tau_0}{\frac{1}{2} \rho U_0^{\,2}}$$

And from above, the localized drag force becomes:

$$F_D = \int_A c_f \left(\frac{1}{2} \rho U_0^{\,2} \right) dA \quad = \quad \frac{\rho U_0^{\,2}}{2} \int_A c_f dA$$

In terms of an average shear stress coefficient, we have:

$$\frac{F_D}{wL} = \frac{\rho U_0^{\;2}}{2}\left[\frac{\displaystyle\int_A c_f \, dA}{wL}\right]$$

And the average shear stress coefficient becomes:

$$C_f = \left[\frac{\displaystyle\int_A c_f \, dA}{wL}\right] = \frac{F_D}{wL\left(\rho U_0^{\;2}/2\right)} \tag{3-2.3}$$

Combining Equations (3-2.2) and (3-2.3):

$$C_f = \frac{1.328}{\mathrm{Re}_L^{\;\frac{1}{2}}} = \frac{1.328}{\sqrt{\dfrac{U_0 L}{(\mu/\rho)}}} \tag{3-2.4}$$

The generalized viscous drag force for a flat plate subject to drag along both faces can be written as:

$$\left(F_D\right)_{panel} = 2\left[C_f\left(\frac{1}{2}\rho_{air} U_0^{\;2}\right)wL\right]$$

And the total viscous drag on a flat plate with a laminar boundary layer is:

$$\left(F_D\right)_{panel} = \left[C_f\left(\rho_{air} U_0^{\;2}\right)wL\right] \tag{3-2.5}$$

$where:$

$C_f = \dfrac{1.328}{\mathrm{Re}_L^{\;\frac{1}{2}}}$, average laminar boundary layer viscous friction coefficient

$\mathrm{Re}_L = \dfrac{U_0 L}{(\mu/\rho)}$, reynolds number given by the panel chord length

$\rho_{air} = $ density of fluid stream

$U_0 = $ free stream fluid velocity

$w = $ panel width

$L = $ panel length

Turbulent Boundary Layer

By applying momentum equations to a turbulent boundary layer, detailed by *Roberson* (1997), the average turbulent boundary layer viscous friction coefficient for a flat plate can be expressed as:

$$C_f = \frac{0.074}{\text{Re}_L^{1/5}} \quad \text{for } \text{Re} < 10^7 \qquad (3\text{-}2.6)$$

The skin friction due to the turbulent boundary layer from equation (3-2.6) above, can be inserted into the generalized viscous drag force given by equation (3-2.5). The total viscous drag on a flat plate with a turbulent boundary layer $(\text{Re} < 10^7)$ is:

$$\left(F_D \right)_{panel} = \left[C_f \left(\rho_{air} U_0^{\ 2} \right) wL \right] \qquad (3\text{-}2.7)$$

where:

$C_f = \dfrac{0.074}{\text{Re}_L^{1/5}}$, average turbulent boundary layer viscous friction coefficient

$\rho_{air} =$ density of fluid stream

$U_0 =$ free stream fluid velocity

$w =$ panel width

$L =$ panel length
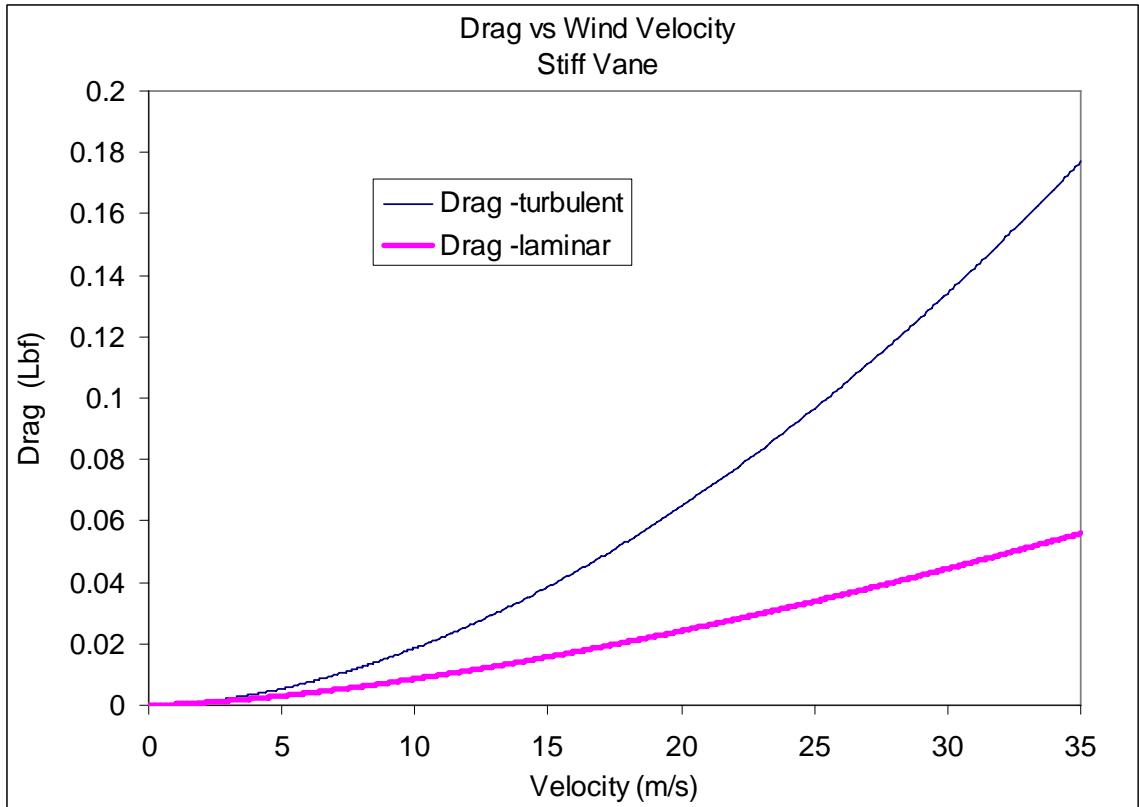
Figure 9 Comparison of laminar and turbulent boundary layer drag for a stiff panel.

From the plot in Figure 9 we see that the viscous drag on a stiff vane is dependent on the boundary layer type. A turbulent boundary layer will produce a higher drag force than that for a laminar boundary layer along the surface of the plate. Noting the ordinate scale, we see that viscous drag (skin friction) is small in magnitude even over a large free-stream velocity range. This point is emphasized in Figure 10, where the effects of the pressure drag from the pole dominate the net drag force for a pole with a stiff vane attachment.
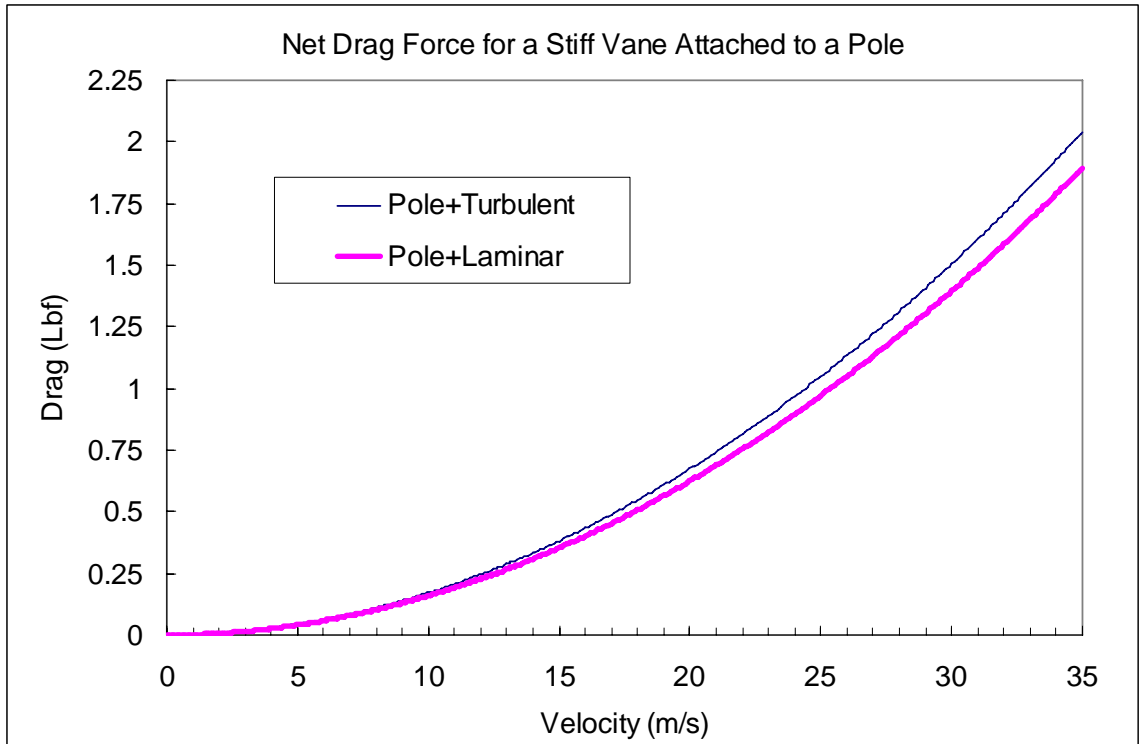
Figure 10 Combined Drag force of pole and stiff vane attachment

Experiments for the stiff panel were completed with a $\frac{1}{16}$ *in.* thick sheet of aluminum, with identical dimensions for the fabrics tested in proceeding sections. Figure 11 shows the chord and span dimension used for every test case. Additionally, the stiff panel setup is shown in its tested condition in Figure 12.
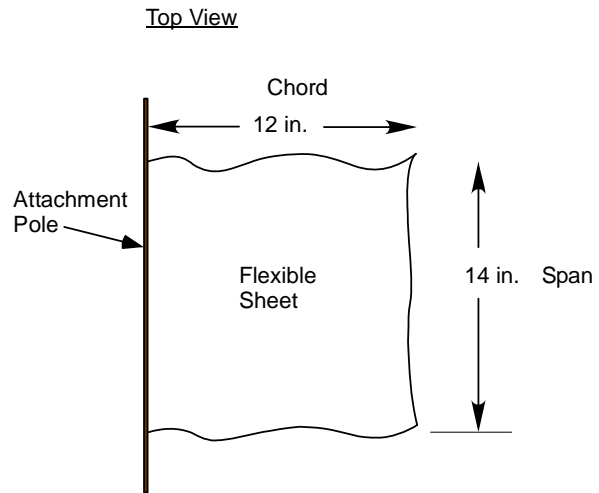
Figure 11. Specimen dimensions for all experimental drag tests
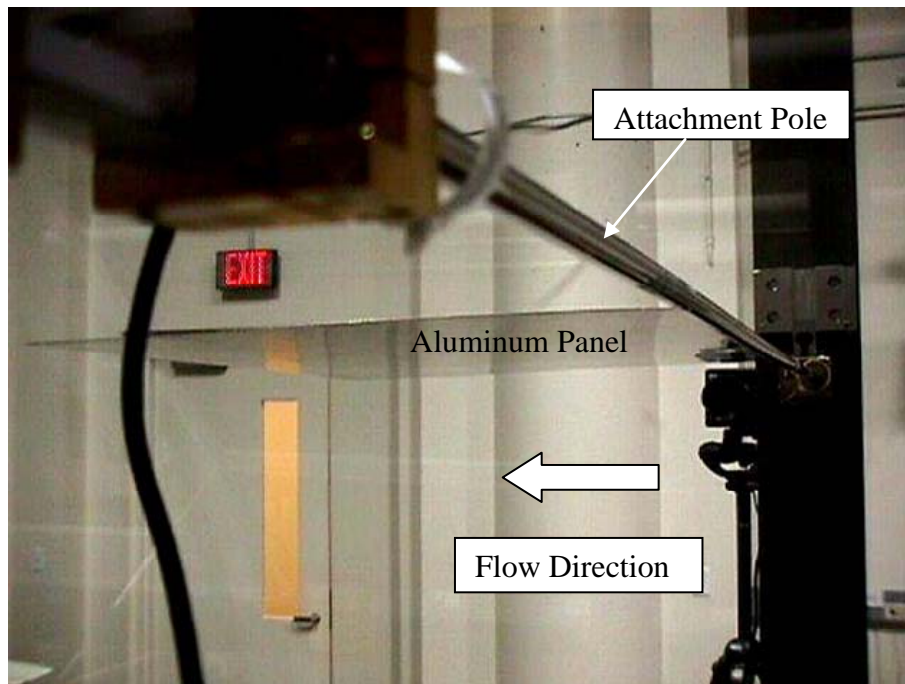
Figure 12. Stiff panel specimen (aluminum) with no air supply
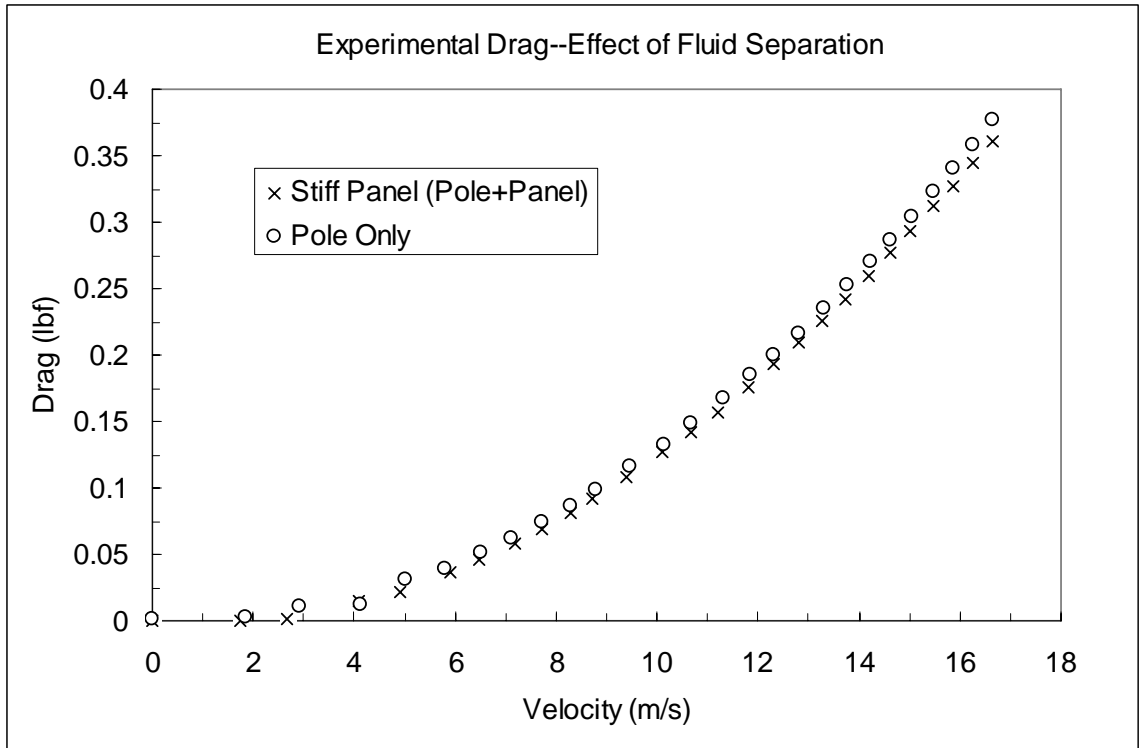
Figure 13. Pole drag dominating stiff panel drag

An important comparison between experimental drag results for the attachment pole (cylinder) and the stiff panel (pole + panel) is shown in Figure 13. Interestingly, we see that the drag force drops as a result of the stiff vane. This decrease in drag is likely the result of fluid being straightened and attaching to the panel, leaving a small wake behind the panel. When the pole is fixed by itself, the turbulence in the wake of the pole is free to mix (swirl) which likely produces a larger pressure drop, which translates to a larger pressure differential across the pole, and thus increased drag. We can then infer that the flow field around the object, that comes from the 'form' of the obstructing object (form drag, or pressure drag), is more important than considering boundary layer skin friction.

Understanding now, that previously discussed theoretical predictions are inconsistent with the observed experimental phenomenon. That is, it is inaccurate to predict the net drag on stiff-vane supported by a pole by taking the sum of its individual components (theoretical) of drag; pressure drag from the pole and viscous drag from sheet. This result should also serve as a warning when using experimental coefficients from texts when the experiment at hand is not precisely as presented via text. This point is made clear in Figure 14.
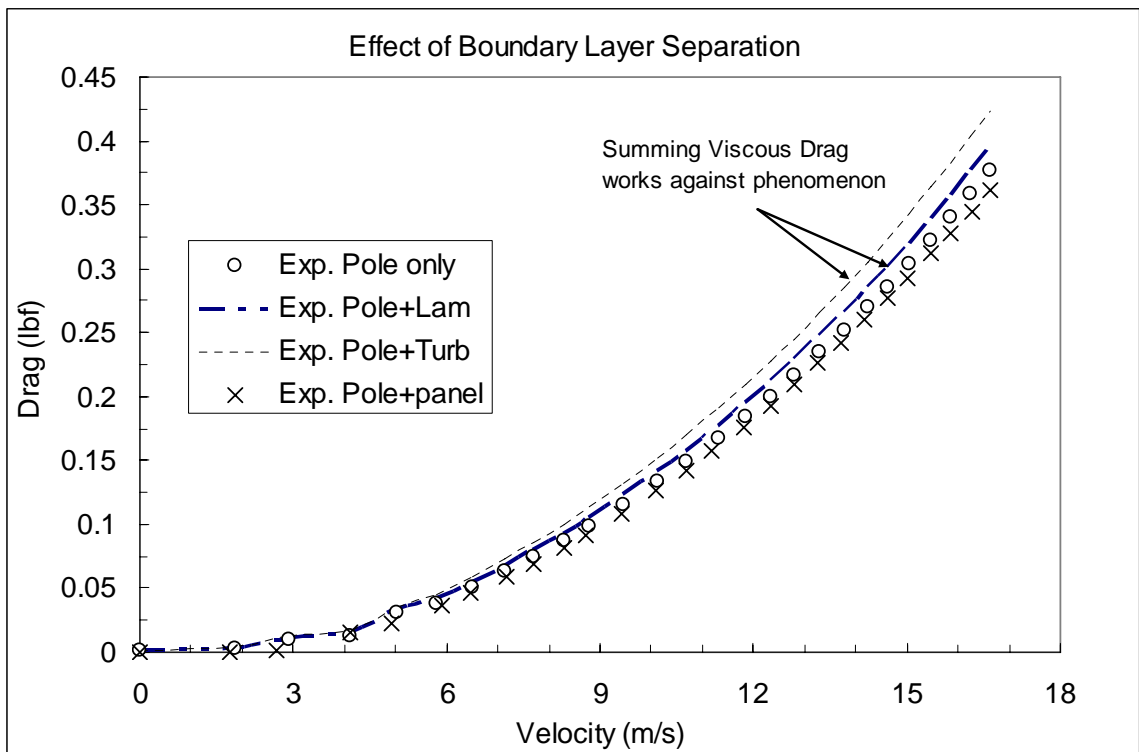
Figure 14. Proof superposition of drag cases is inaccurate

The stiff vane case (pole + panel) is still insightful, in that we can compare the net drag produced by flexible flags with identical dimensions, and thus infer the component of dynamically induced drag by the fluttering flag.

3.3   Flexible Vane Drag in a Fluid Stream

For the case of a flexible vane (flag), there are three drag components that comprise the net drag force exerted at the attachment point (flagpole). The flagpole exerts pressure (form) drag, while the flag contributes both pressure and viscous (skin friction) drag. A flag in a fluid stream is accelerated by normal pressure forces which impart an out-of-plane curvilinear motion. As a result of this "flutter" motion, centrifugal forces induce in-plane tension in the fabric. This tension acts to "flatten" the flag thereby opposing the fluid pressure forces which generate the out-of-plane curvature (motion). This process dynamically transforms the lift forces (from the flow field) into tension forces, felt as a dynamic drag at the attachment. The breakdown of component forces on an undulating specimen is illustrated in Figure 15. A very small contribution of drag comes from viscous shear stress acting drag along the curved surface of the flag (skin friction). The viscous drag is a function of the fluid boundary layer along the curvilinear chord length, which consequently could be a combination of both laminar and turbulent boundary layers. Experiments from the stiff panel vane have clearly shown the dominance of pressure drag (of the pole) over viscous drag (of the panel), and in proceeding chapters we will show that the net drag from a fluttering flag (from induced in-plane tension) is even more dominant than the pressure drag from the pole.
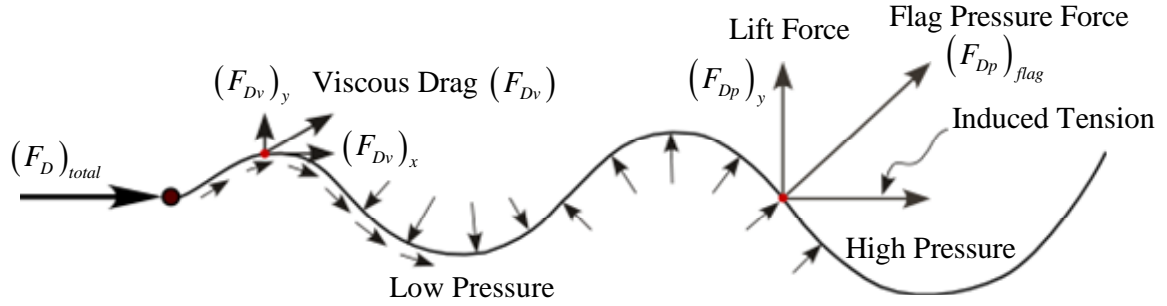
Figure 15 Diagram of forces on a flexile web

From the free body diagram in Figure 15, the net drag force is given by:

$$\left(F_D\right)_{total} = \left[\left(F_{Dp}\right)_{pole} + F_{Dv} + \left(F_{Dp}\right)_{flag}\right]$$

(3-3.1)

The flutter phenomenon is a complicated balance of forces that continually exchange energy. *Moretti* (2003) suggests that the large curvature of the fabric at the leech, as a result of the flutter motion, generates centrifugal forces that induce the largest tension and corresponding drag force at the attachment, above and beyond the magnitude of skin friction drag. It has been well documented, that flags with a larger span exhibit larger amplitudes of oscillation than that of a flag with same chord length but smaller span. Applying what we just described, the larger amplitudes of oscillations come from the pressure forces acting normal to the flow field (and flag), spread over a larger area which generates the deflections needed to create the centrifugal forces which *Moretti* mentions, ultimately limits the amplitude of oscillation.

CHAPTER IV

EXPERIMENTAL STUDY

In this chapter, the methods used to capture various experimental variables, the procedure used, and the results are presented. This chapter is organized into five sections. Section 4.1 presents the experimental setup, specifically designed for the study of drag forces imparted from an attachment specimen. This section further discusses the experimental methods used to capture/compute each experimental variable. Section 4.2 provides a step-by-step procedure used to capture experimental data for each test specimen. Section 4.3 describes the estimation of uncertainty of the experimental drag data. Finally, the experimental results are presented in Section 4.4.

4.1   Experimental Setup

Wind Tunnel Test Section

Wind tunnel experimentation was performed using a downdraft wind tunnel and a removable test section with a $3 \times 3\,ft$ cross-section. A new section was designed and fabricated specifically for the purpose of this experiment. An assembly drawing, serving as the model for detailed fabrication drawings is shown in Figure 16.
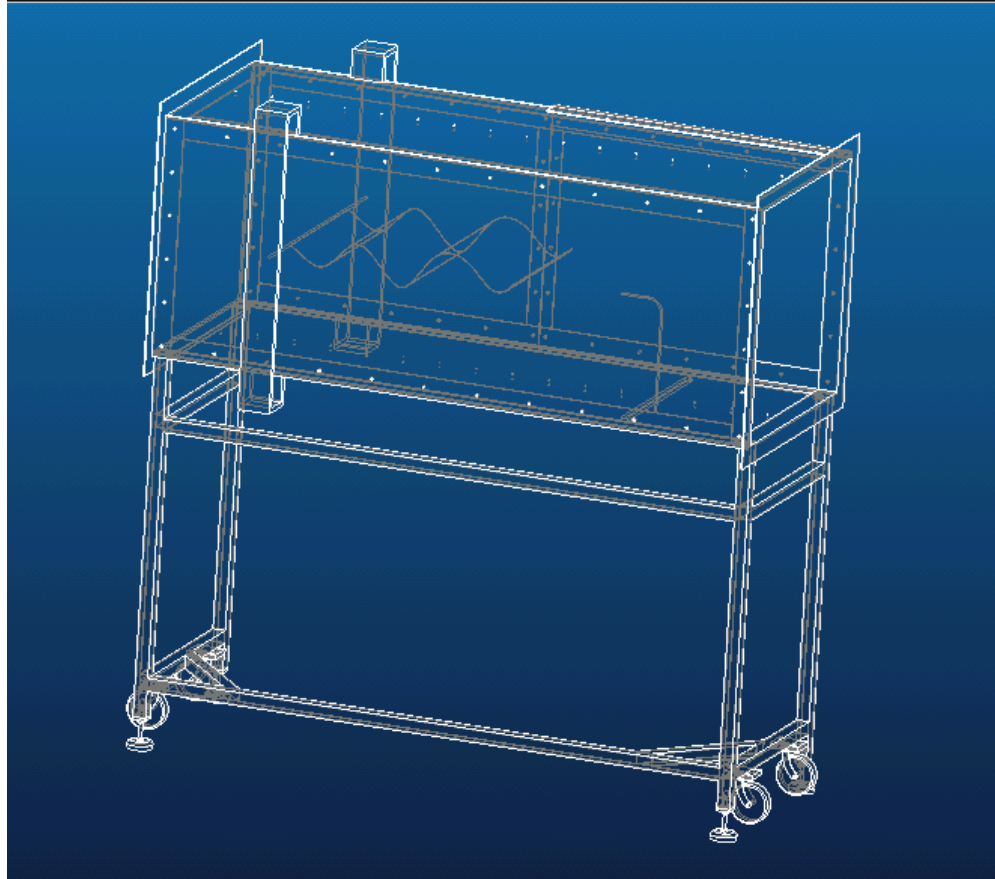
Figure 16 Wind tunnel test section illustration with specimen and pitot tube probe.

The removable test section features rigid mounting pillars for load cell attachment, pitot tube traverse, half panel access door, adjustable vibration damping feet, and acrylic viewing panels. The section was constructed of three-inch angle iron and has a step-less inner cross-section. The angle iron section serves as a 'shell' for the routered edges of the acrylic panels to fit snugly into place. The base of the test section was constructed of two inch square tubing and has one open side for easy user/equipment access. Detailed part lists and assembly drawings can be found in Appendix A. The

completed test section is shown inserted into the wind tunnel with related experimental

instrumentation in Figure 17.
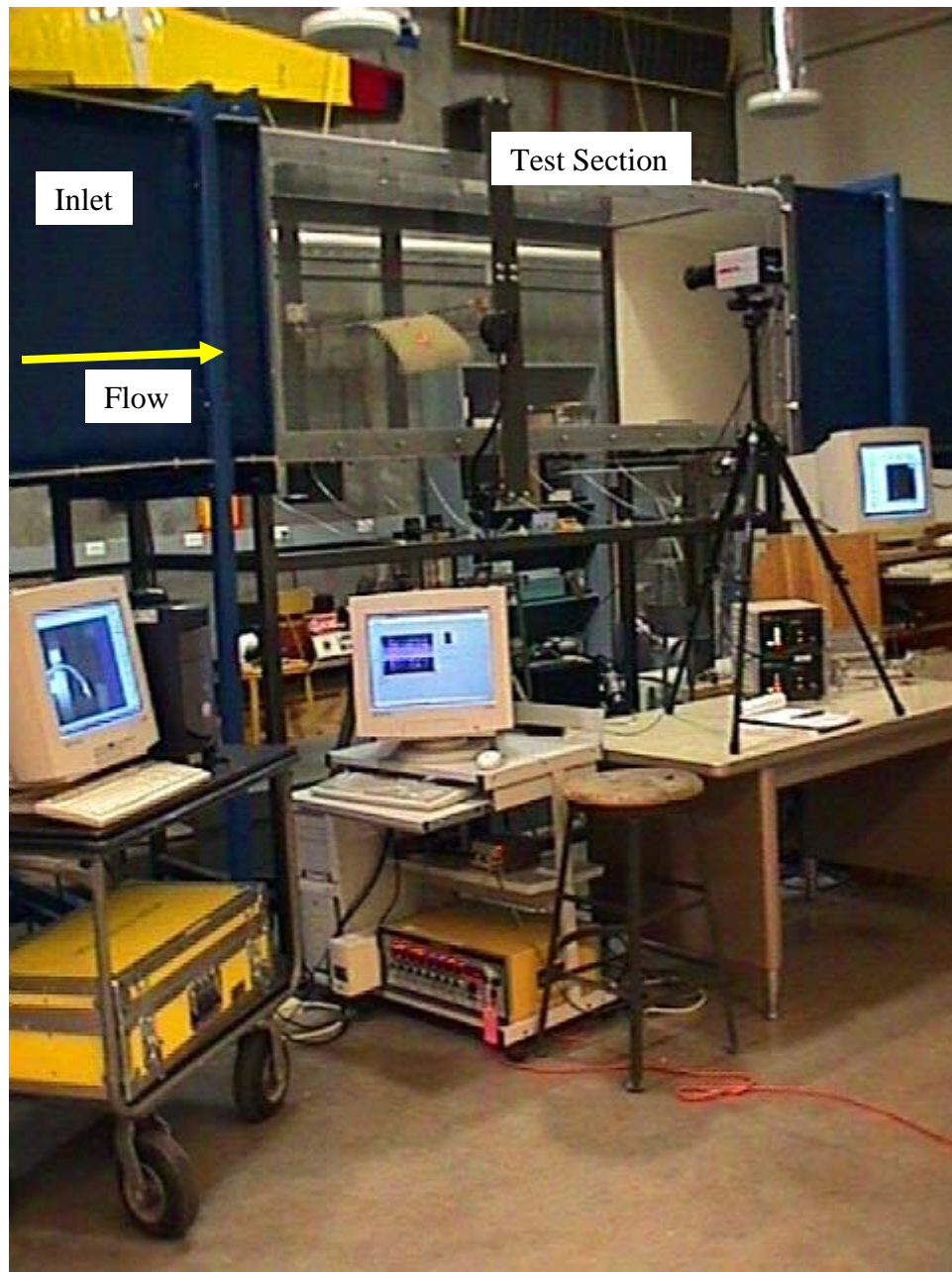
Figure 17. Wind tunnel experimental set-up

<u>Attachment Pole</u>

A critical component used throughout the course of this study was a $\frac{3}{8}$" diameter stainless steel (AISI 302) rod, machined to allow interchangeability between test specimens. The rod features a removable center section that utilized six tapered machine screws to secure the rod half, and effectively pinch the specimen securely into place. This interchangeable design was necessary from an experimental standpoint, in that a consistent method (and attachment geometry) was used to attach test specimens, such that experimental inconsistencies when attaching specimens could be reduced. With the machine screws securely fastened, formable tack putty was molded into the tapered screw recesses, such that the rod retained its seamless round contour. A thin transparent tape was then stuck along the center section such that it covered the putty holes and "slot" created from the two halves joining. The attachment pole with and without a specimen is shown in Figure 18. The rod was marked on one end, such that the rod was orientated in the same position, with consistent clamping tension for each test specimen.
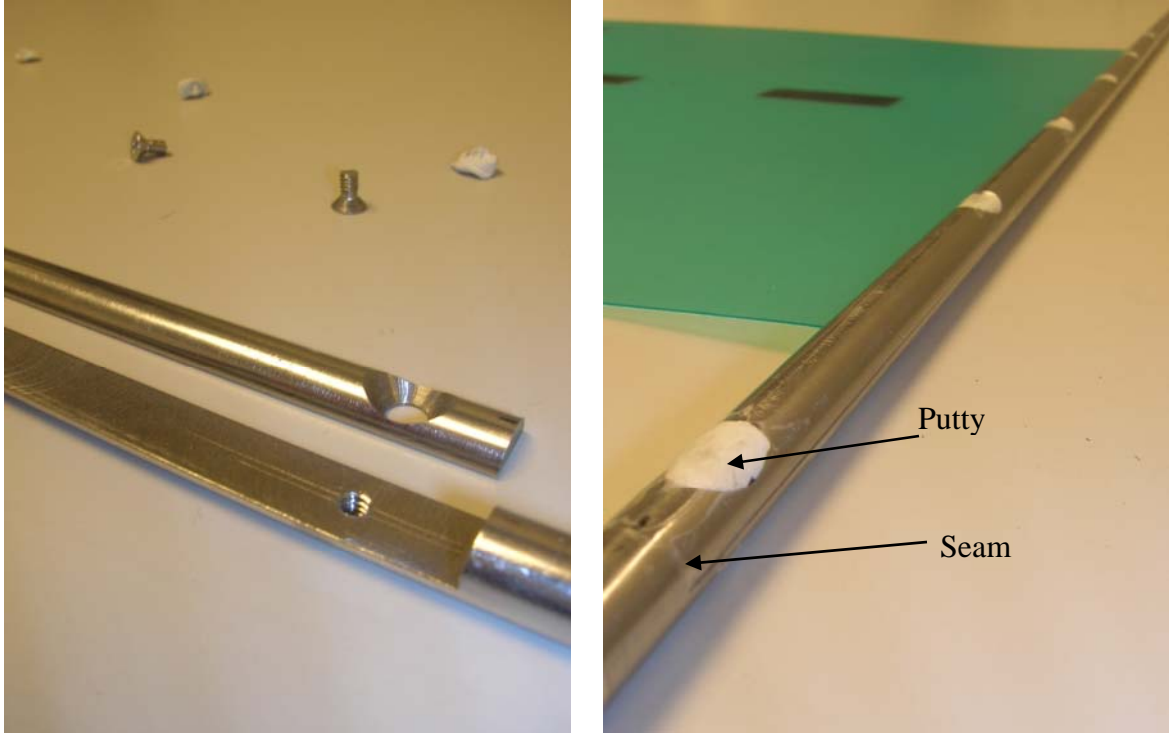
Figure 18. Attachment pole

Figure 19. Flag pole with flexible specimen μ=1.88

Drag/Lift Measurements

Drag and lift was simultaneously measured by coupling two commercially available 'beam type' load cells. As shown in Figure 20 below, each load cell is dedicated to measure force in one direction. By manufacture design, slight out of plane forces cancel, and the resulting output comes solely from the generated in-plane forces.
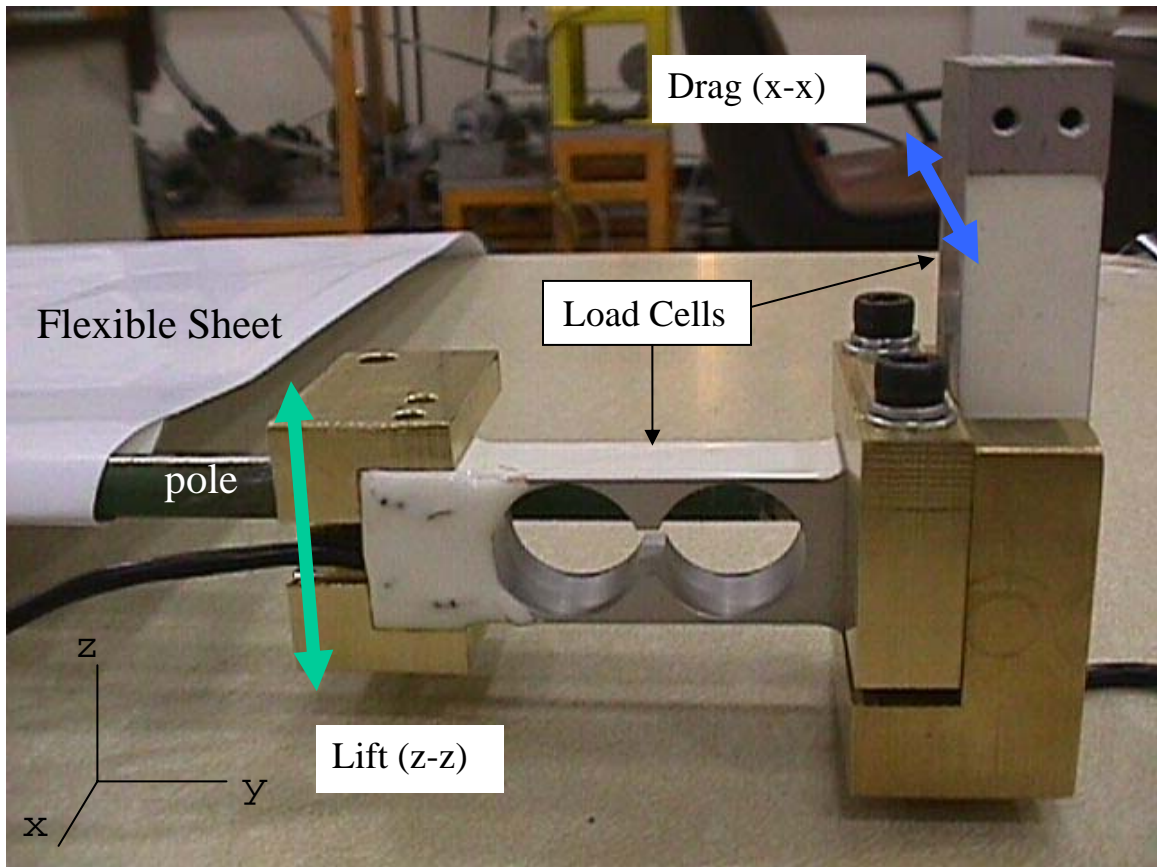
Figure 20 Coupled drag and lift transducers

Four *Transducer Techniques* beam type load cells: *LSP-1*, rated at 1 kgf $(2.2\ lbf)$, were coupled by way of precision machined brackets to support a $\frac{3}{8}$ in.

attachment pole. The load cells were press fit and secured with machine screws into each bracket, and were mounted onto a rigid (frame welded) support as shown in Figure 21. Two load cells on each support end were dedicated to measuring lift and drag respectively. A *Measurements Group ES 2100* Strain indicator/amplifier was used to condition and amplify the voltage signals from each load cell. Load data was acquired using *National Instruments LabVIEW 6* Data Acquisition software and a *PCI-6025E* series multifunction DAQ card.
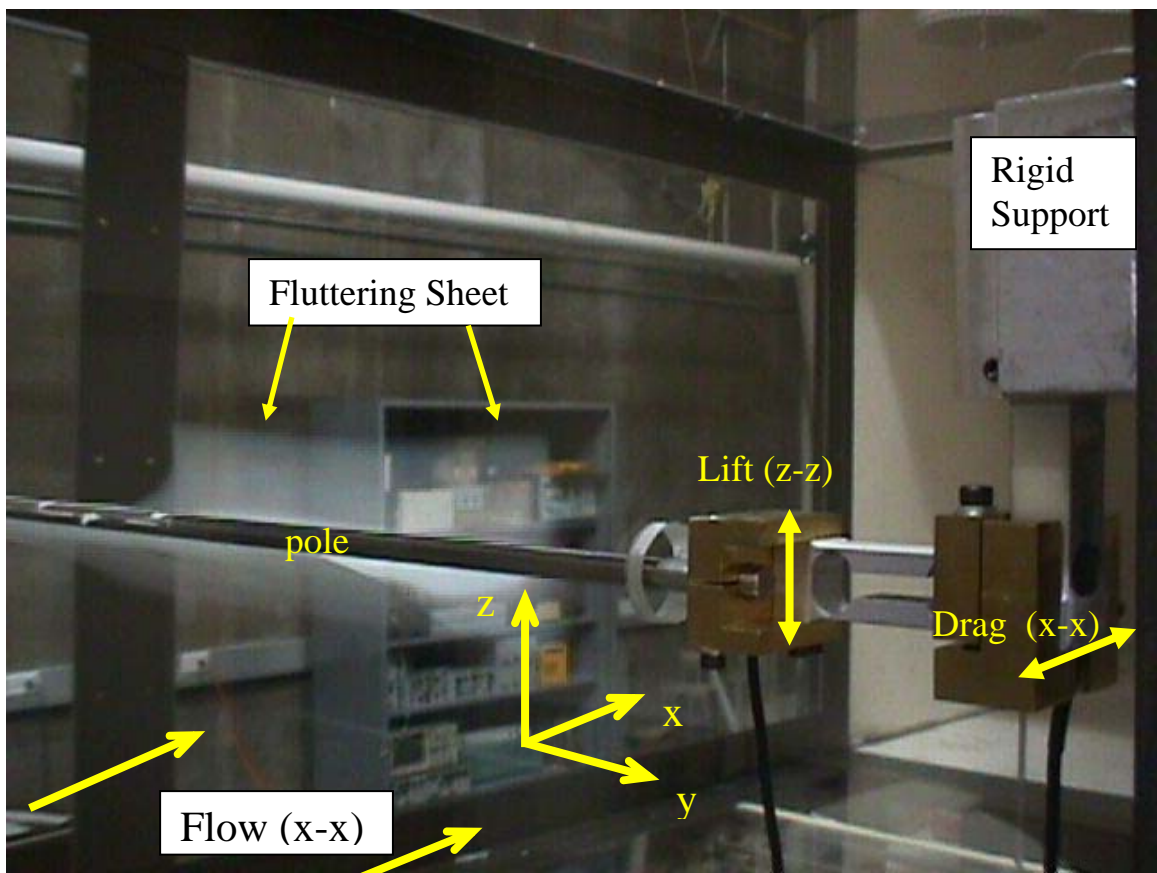
Figure 21. Lift and Drag Measurement on a Fluttering Flag

Pressure Measurements

Pressure measurements were made with a Validyne DP45-18 Very Low Differential Pressure Transducer with a pressure range of: $0 \leq \Delta p \leq 2.22 \ in - H_2O$. Sizing was determined based on maximum tunnel velocity limit, conservatively set for the acrylic panel test section to be 30 m/s, which is roughly equivalent to $2.0 \ in - H_2O$ based on air density at $35°C$. Tunnel velocity profiles are calculated by means of measuring a differential pressure from a pitot state tube. By measuring the pressure differential, the fluid velocity is calculated by way of Bernoulli's equation. A schematic of the pitot static tube used for all experimental pressure measurements is shown in Figure 22 below.
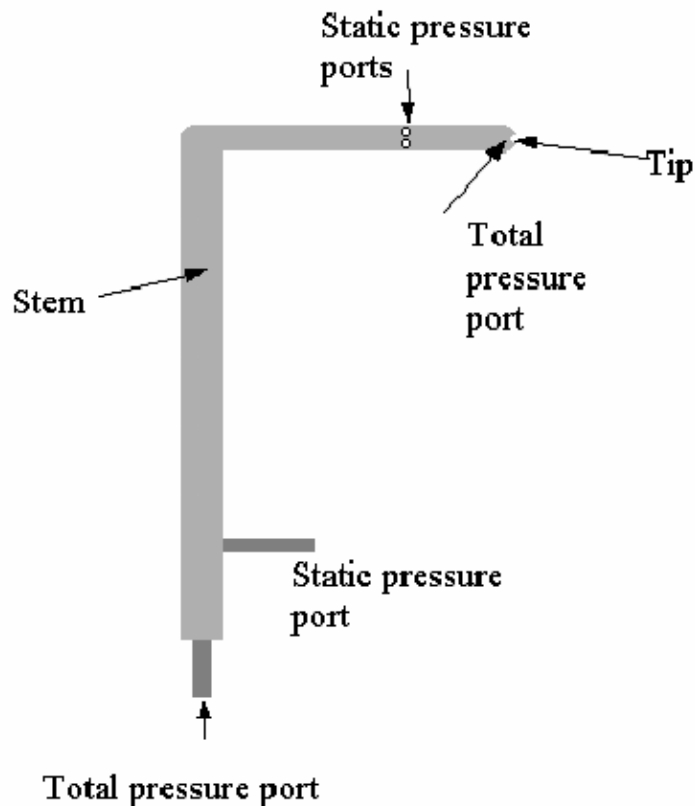
Figure 22 Schematic of a pitot static tube.

The term "pitot static" comes from the fact that the tube requires the measurement of both static pressure and total pressure for accurate velocity prediction. Total pressure is also referred to as the "stagnation pressure", because the fluid velocity is assumed to be zero at the tip entrance, thus creating the largest pressure. At this point, all of the fluid's kinetic energy is converted into potential energy, often called pressure energy. Using the velocity-pressure relationship derived from Bernoulli's equation in Section 3.1, recall the total pressure $p_s = p_1 + \frac{1}{2} \rho v_1^2$ can now be applied to compute the free stream fluid velocity (U_o).

solving for the free stream velocity:

$$v_1 = \sqrt{\frac{2(p_s - p_1)}{\rho}} = U_o$$

A velocity profile of a center section of the wind tunnel cross-section measuring $26 \times 26 \; in.$ was scanned in 1 in. increments using a bi-directional traverse controlled by stepping motors. Figure 23 shows the pitot tube mounted within the traverse setup.
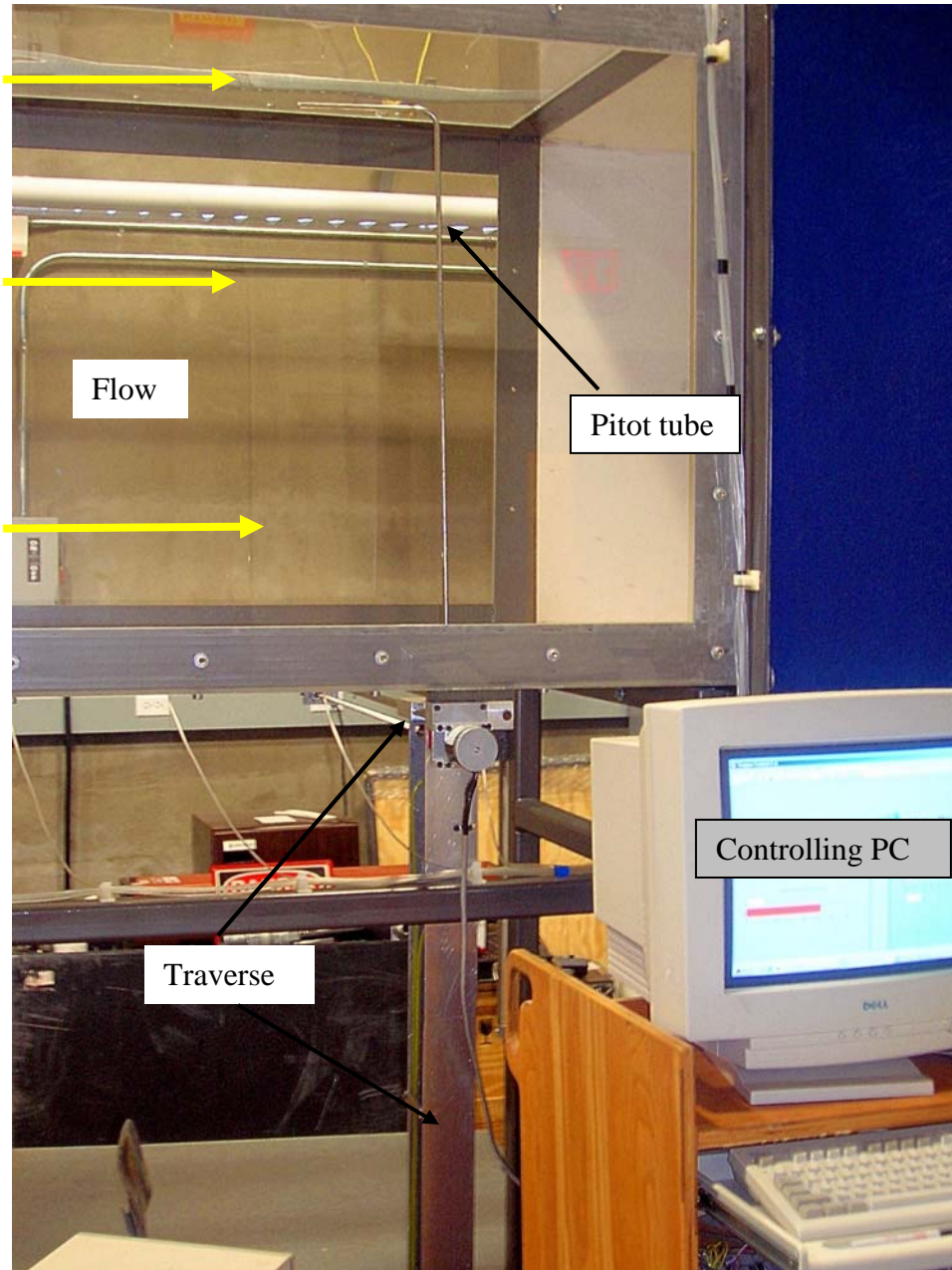
Figure 23. Pitot static tube traverse

The stepping motors were controlled digitally with LabView. A custom code was written to allow for both free control, direct x, y step increment control (for positioning

the pitot tube for general velocity readings) and an automated sweep control, which performs a sweep in 1 in. increments to the data matrix the user specifies (Appendix E).

In the automated control, data is written to a file at each step location along with the pitots' current x, y position. The data matrix is parsed in LabView and written to file such that it can be read directly by a MatLab script, which takes the $[n \times 3]$ matrix and creates a contour plot of the velocity data. An example velocity contour plot is given in Figure 24 below, and the m-file contour script is given in Appendix B.
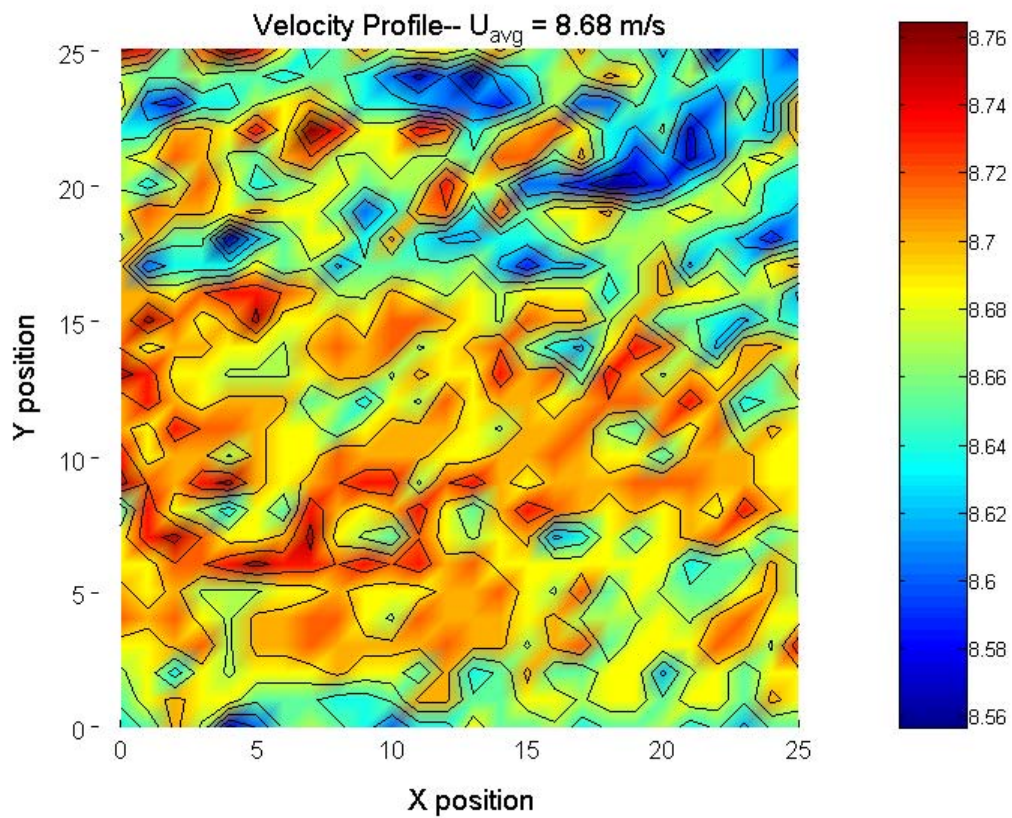
Figure 24. Free stream velocity profile using bi-directional traverse.

To control the stepping motors, the low current digital pulses from the computer are fed into a high speed transistor switching circuit. With a 6 Volt power supply connected to the motors, the transistor served as a switch to ground the coils when the digital signal from the computer is given to transistor base (power sink). Detailed schematics of stepping motor operation and circuitry are given in Appendices C-E.

Frequency Measurements

Frequency measurements were made with a pair of laser vibrometers, by focusing a fixed beam on reflective tape stuck to the fluttering specimen. The sensors: two *Polytec* OFV 350 laser–doppler vibrometers incorporating a 1 milliwatt Class II HeNe-laser and a Nikon projecting/collecting lens. Each sensor head is connected to a *Polytec* OFV 2600 velocimeter controller which converts velocity measurements to voltage signals, with three selectable gain ranges: 5, 25, or 125 $\frac{mm/sec}{Volt}$. Voltage data was captured at 500 Hz $(\Delta t = 0.002)$ until $2^{15} = 32,174$ data points were saved.
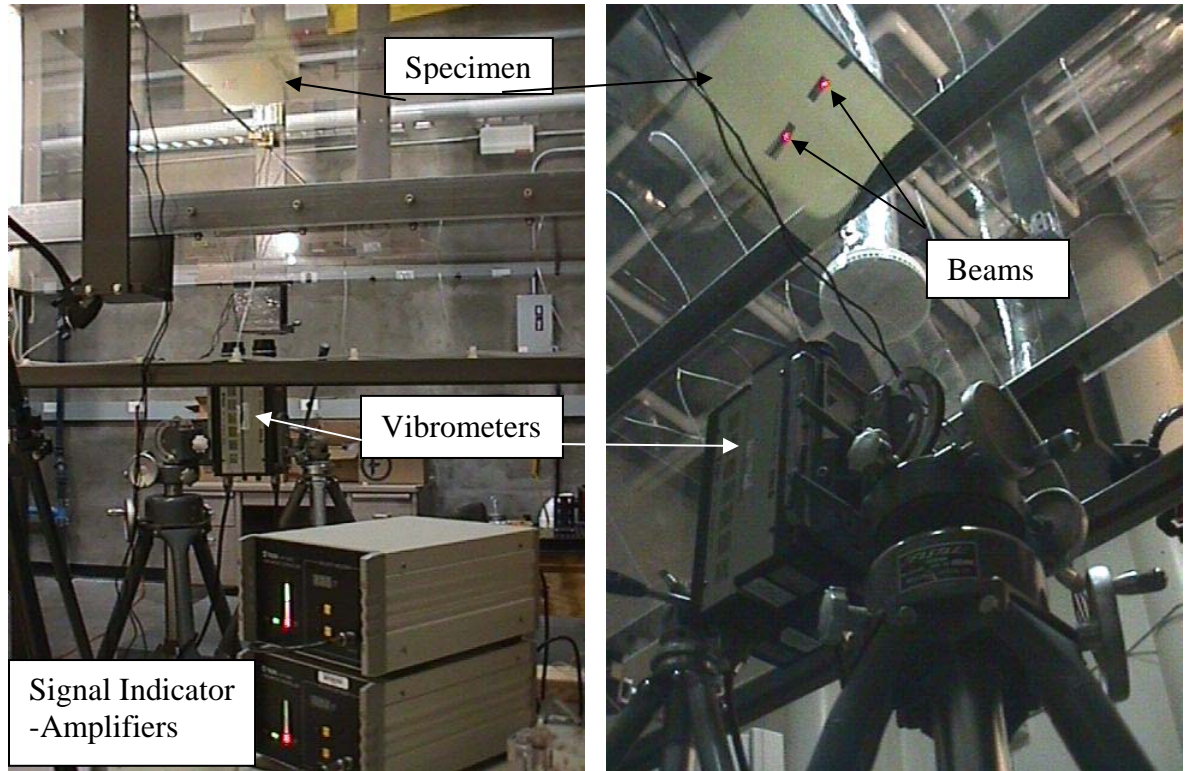
Figure 25. Vibrometer Set-up

The accuracy of the frequency measurements with the laser doppler vibrometers was first tested by using a loudspeaker, audio amplifier and a signal (function) generator. A small piece of reflective tape was placed on the drumhead and the laser vibrometer was aligned and focused on the tape such that the LED signal indicator confirmed high signal strength (reflectivity). By feeding a known signal (sinusoid) to the loudspeaker (through the audio amplifier), and using a Fast Fourier Transform (FFT) of the data, frequency measurements made with vibrometer were extremely accurate for various frequency ranges tested. In each case, the FFT results matched the signal generator frequency, with two additional significant digits (decimal).

Frequency measurements were made by placing the reflective tape toward the center of the sheet, such that the vibrometer laser beam was in constant contact with reflective tape. Due to the large "whip" action observed at the trailing edge of a fluttering sheets, the laser beam shot by the vibrometer was unable to stay in constant contact with the reflective tape. It was hoped that amplitude at the trailing edge (leech) could be computed with the vibrometers, however the extreme "whip" action at the leech caused momentary loss of signal. The next subsection discusses the use of a high speed camera to capture such data.

Traveling Waves

The cross spectrum is a FFT based signal measurement defined as:

$$\text{Cross Power Spectrum } S_{XY}(f) = \frac{FFT(Y) \bullet \left(FFT(X)\right)^*}{N^2}$$

where :
$\left(FFT(X)\right)^* = $ complex conjugate of the FFT of signal x
$N = $ Number sampled points describing one waveform (x or y)

The cross spectrum is used to compute the phase difference between two signals of like frequencies. When used with only one measurement signal the cross spectrum is referred to as a power spectrum, where $S_{XX}(f)$ is the rms amplitude at an indexed frequency. As an example to which we know the solution, the cross power spectrum of a sine and cosine function: $y(t) = \sin(2\pi \bullet 15)$ and $x(t) = \cos(2\pi \bullet 15)$ is shown in Figure 26.
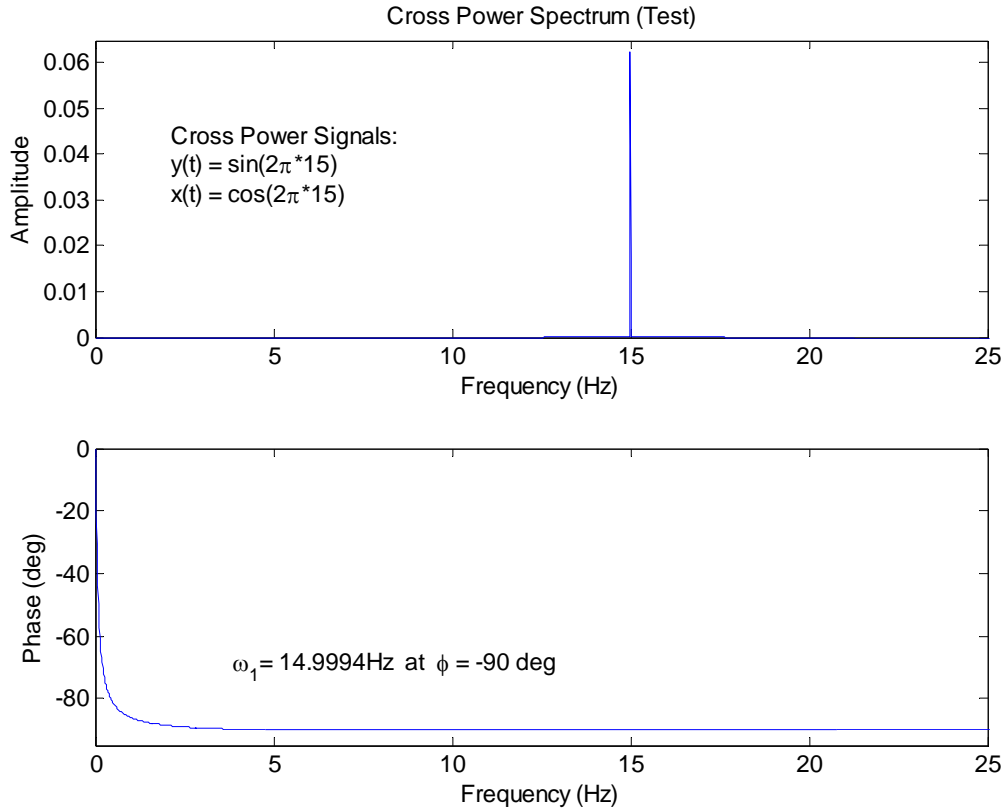
Figure 26. Cross spectrum test confirming 90° phase shift of sine and cosine function.

As expected the phase difference between a sine and cosine function is $90°$, furthermore this test confirms the accuracy and implementation of the Matlab m-file script that was used to compute all frequency and phase data for flutter experiments. This script is given in Appendix G. This MatLab script pulls two columns of voltage data $\begin{bmatrix} 2^{15} & 2 \end{bmatrix}$ from the vibrometers saved in *Excel*, puts the data through a Hanning window, computes the FFT for each vector, applies the cross spectrum function, finds the first four harmonic frequencies, plots the frequency and phase spectrum, and displays the

fundamental frequency and phase on the plot. An example plot for a flexible sheet with mass ratio $\mu = 1.88$, is shown in Figure 27.
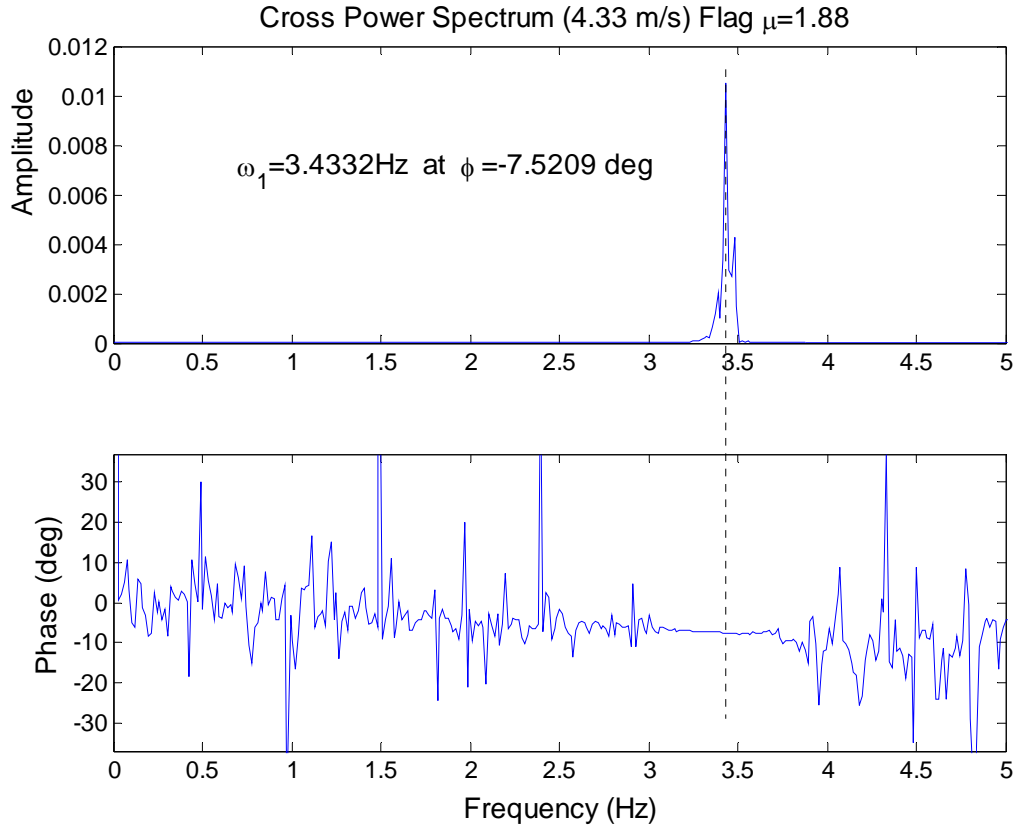
Figure 27. Cross FFT frequency and phase information for a flexible sheet at 3.43 m/s.

Executing the Matlab cross spectrum script, and zooming in, there is a dominant "spike" near 3.5 Hz. This spike is a quantitative measure of the power, and hence the relative contribution to the entire frequency spectrum. We find the exact location of the fundamental frequency to occur at $3.43\ Hz$. Utilizing the same index to find frequency, the corresponding phase angle is $-7.52°$. This approach is continued for increasing

velocities to form plots of frequency and phase vs. velocity. These results will be displayed and discussed in Section 4.4.

Mode Shape Measurements

A model XS42GB-MONO high speed digital camera from Integrated Design Tools, Inc. (IDT) was used to capture frame by frame deflection profiles at $500\ Hz$ $\left(\Delta t = 0.002\ \text{seconds}\right)$. The camera was set approximately four feet from the specimen and was pointed perpendicular with the edge of the fluttering specimen as shown in Figure 28. Because of the large amplitude deflections and curling at the leech, measuring high speed images (pixel correlation) is thought to be the only accurate method to compute the amplitude at the leech.
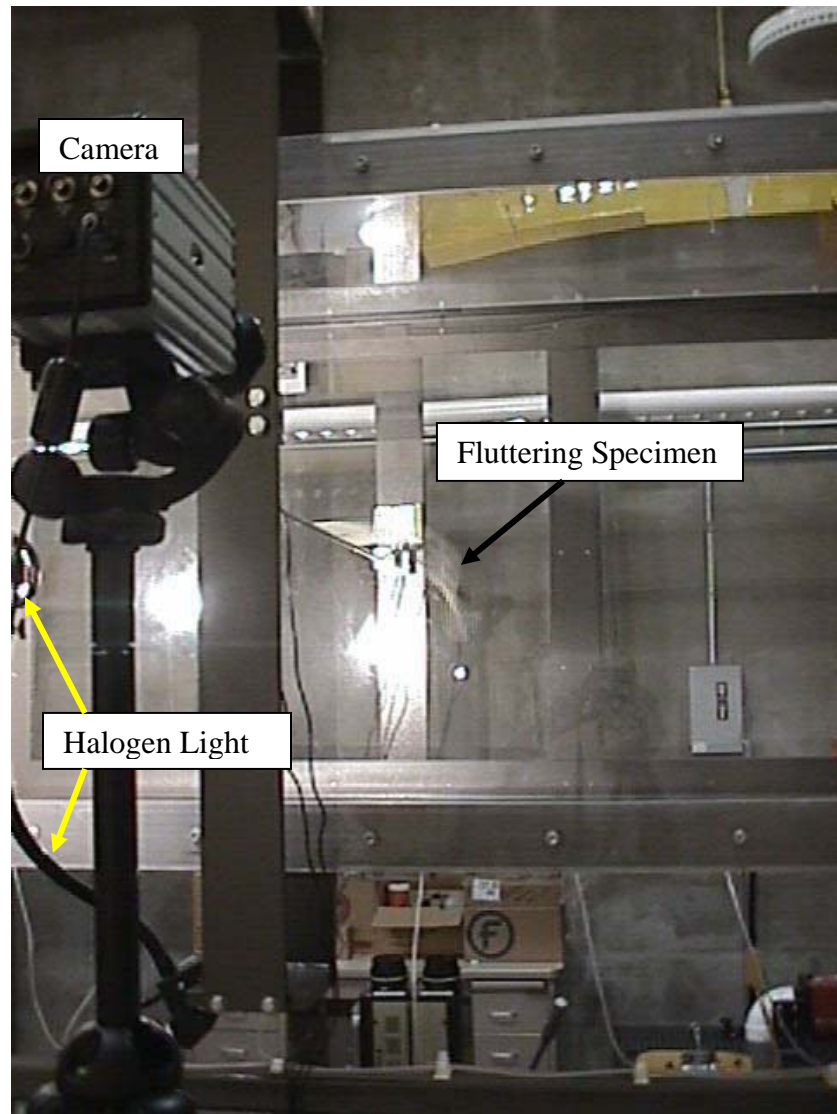
Figure 28. High speed camera set-up

To understand mode shapes, and to extract amplitude data for theoretical drag correlations [Thoma/*Moretti*], a commercial photo editing software (ULEAD), was implored to measure pixels. Amplitude and wavelength information was extracted from high-speed images by correlating pixels to known dimensions in the photo. Image data was parsed, such that the maximum image with the maximum deflection (amplitude) was

measured. For low velocity cases, where deflections were not symmetric about the pole (due to gravity), the mean, of both the upper amplitude (seen in Figure 29) and the largest downward deflection were taken as the experimental amplitude. Figure 29 illustrates the procedure used to measure the amplitude of the main test specimen, $\mu = 1.88$.
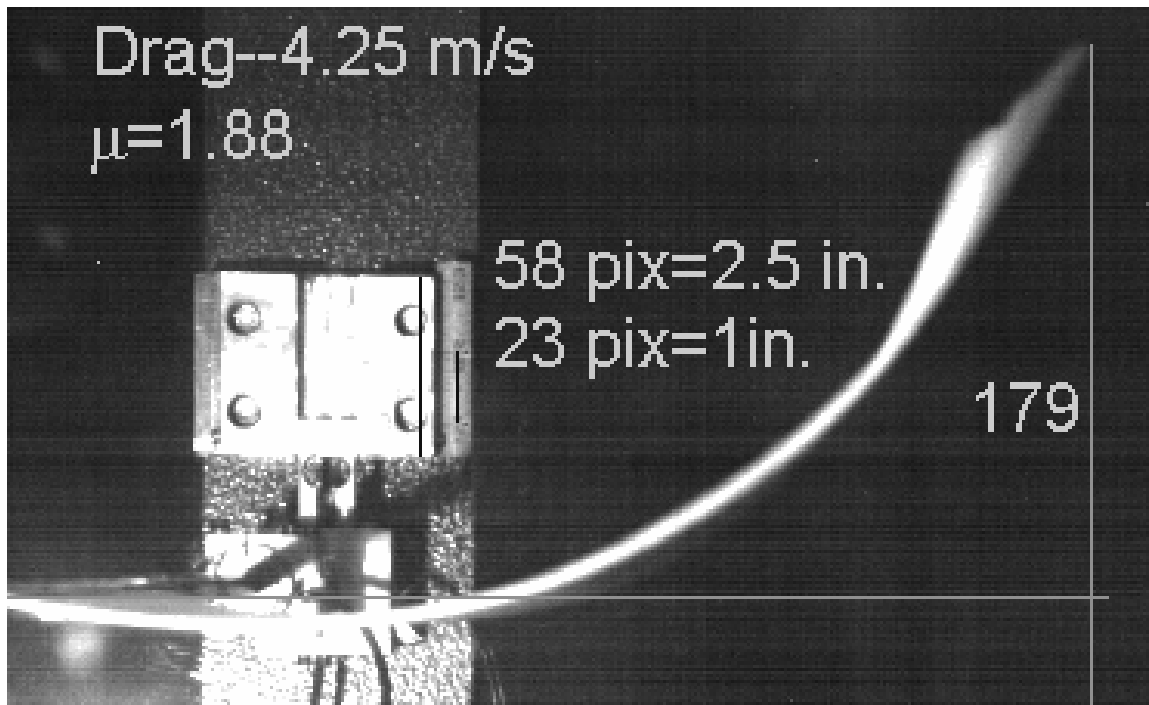
Figure 29. Amplitude measurement from high speed photo data

Generalized mode shapes can be visualized and measured by superimposing several images on top of each other as shown in Figure 30. As an additional check on the vibrometer setup and FFT analysis, the computed frequency from the image data $(\Delta t = 0.01 \text{ sec})$ was 7.14 Hz. Compared with 7.18 Hz computed by implementing a FFT of vibrometer data; FFT analysis proves to be accurate and considerable less tedious to compute. For the frequency measurement made in Figure 30, a complete cycle of

images must be parsed (here the 14th frame coincides precisely with the 0th frame) and

knowing the frame rate Δt, we have : $f = \dfrac{1}{T} = \dfrac{1}{14(0.01)} = 7.14 \text{ Hz}$. On the other hand,

the FFT script in *MatLab* can be executed in matter of seconds. The use of high speed

images however, is the only means by which to accurately measure modal properties,

such as amplitude, wavelength, and node location. Pixels are approximated into units of

length by: $\left[in. = \dfrac{2.5}{58} (\#Pix) \right]$
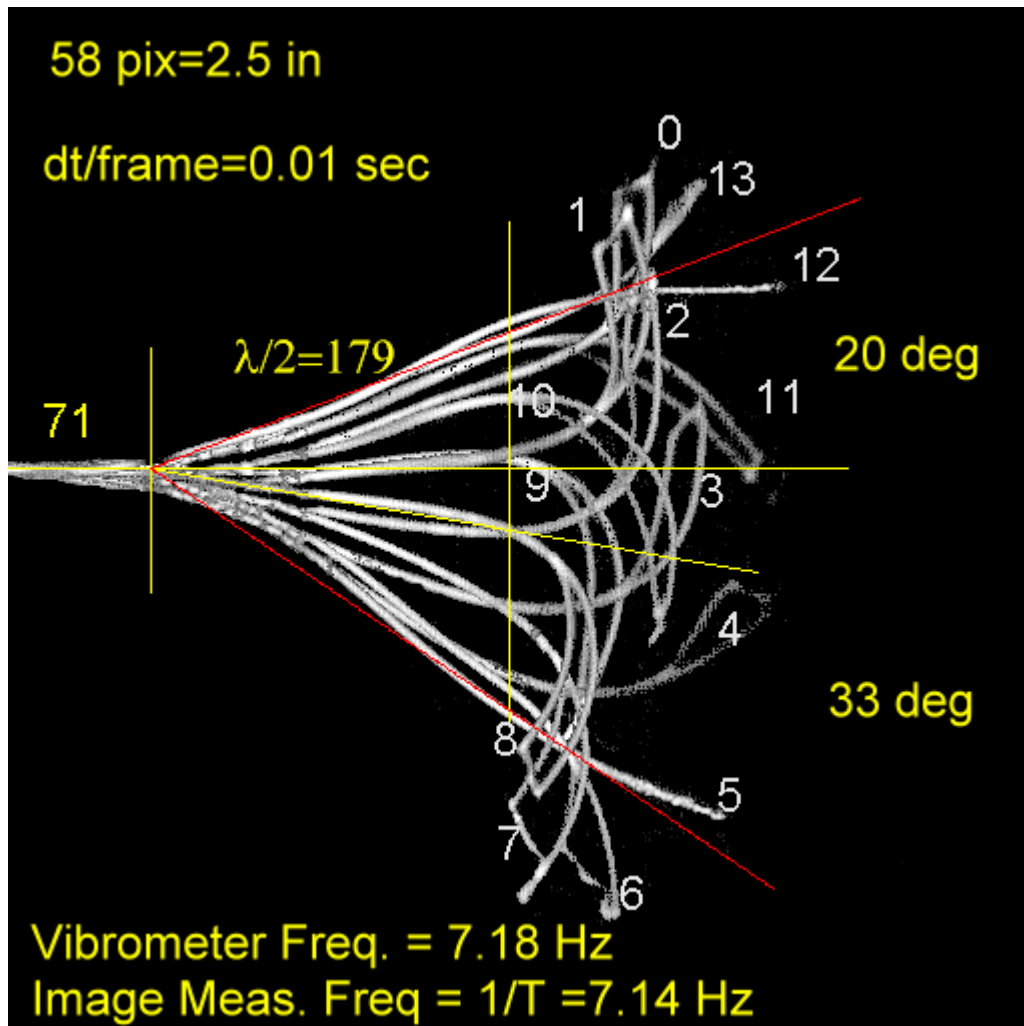
Figure 30. Heavy sheet deflection modes 8.41 m/s (μ=1.88)

4.2   Experimental Procedure

The quantities measured and/or computed in this experiment were F_D, F_L, Δp (v), f_{Hz}, T_{room}, and high speed image deflections. Three independent personal computers were used to gather the experimental data as shown in Figure 31. PC #1 was used to capture high speed deflection images, PC #2 was used to capture drag data from the four load cells and pressure data (Δp) from the pitot-static tube, and PC #3 was used to control the pitot traverse, record pressure data during cross-section sweeps (velocity profiles), and record frequency signals from the two vibrometers. The pressure transducer signal was split, and sent to PC #2 and PC #3 for simultaneous velocity correlations between experimental variables. Each pressure signal was independently calibrated to account for lead wire resistance.
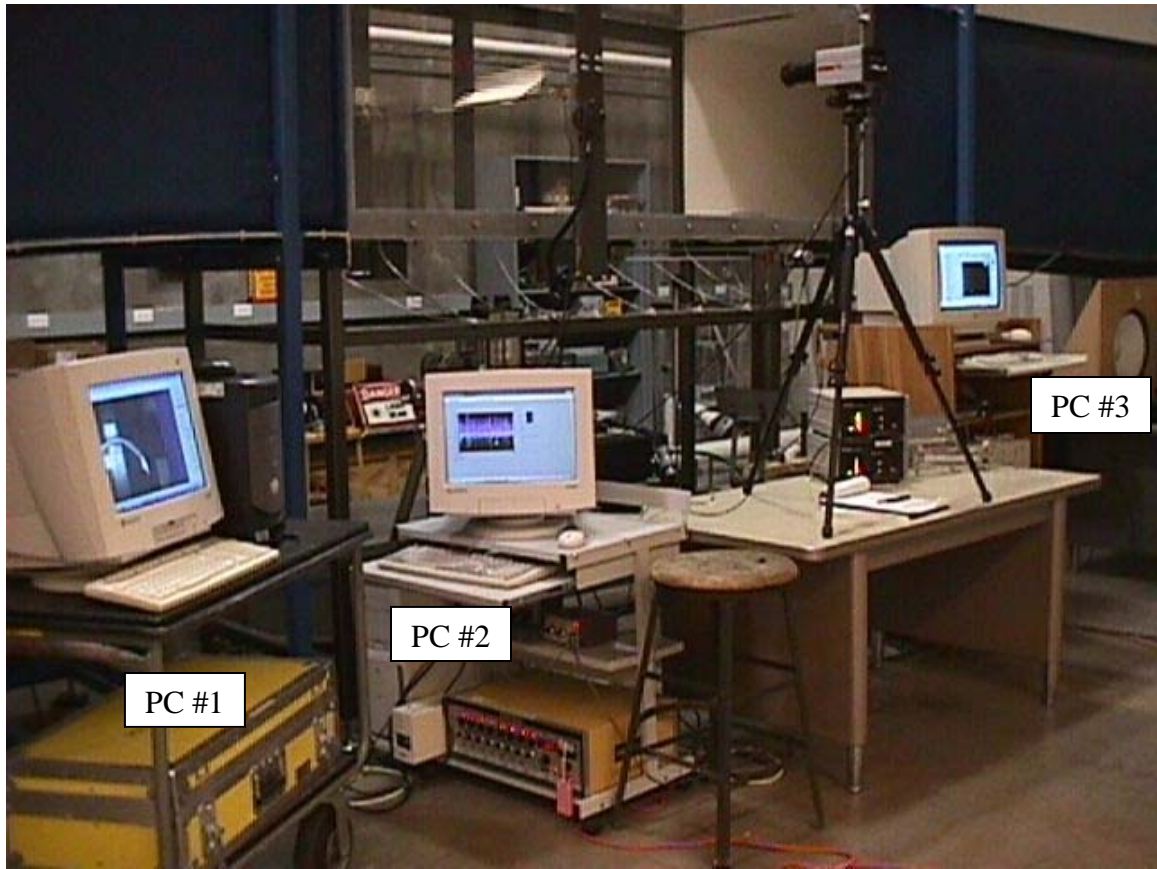
Figure 31. Experimental set-up

The procedure that was followed when capturing experimental data is described in steps 1-10 below:

1.) All test equipment and related electronics were powered for at least one hour prior to the start of a test.

2.) With the test specimen affixed to the attachment pole, high strength fishing line was strung onto the attachment pole with a large loop for hanging calibration weights. The pole and specimen were then inserted into the wind tunnel.

3.) With specimen in place, the wind tunnel was slowly ramped to a maximum test velocity, where the specimen either exhibited three dimensional (and/or irregular) deflections, or experienced especially violent oscillations close to exceeding load cell capacities. At this critical velocity, drag data was recorded to check signal strength and/or saturation. The signal conditioner gain (amplification) was then adjusted such that the output was very close to, but less than the saturation voltage of the AD card. The tunnel was then turned off, and the drag channels were adjusted to zero output. The tunnel was then ramped up again to the critical velocity to check saturation. This procedure was repeated until a satisfactory nulling was seen at no wind velocity, and a maximum output (under AD saturation) was seen at the critical velocity. Gain and nulling knobs were then locked in position.

4.) With the specimen still in place, a calibration jig was inserted into the tunnel. The calibration jig features and a small pulley wheel which was adjusted to the same height as the attachment pole. A horizontal force (drag force) was applied by hanging weights on an extension string that passed through the pulley as shown in Figure 32. Lift calibration was achieved by hanging weights directly on the fishing loop, such that they hung directly from the pole. Drag and lift calibration was performed for each test specimen as just described.
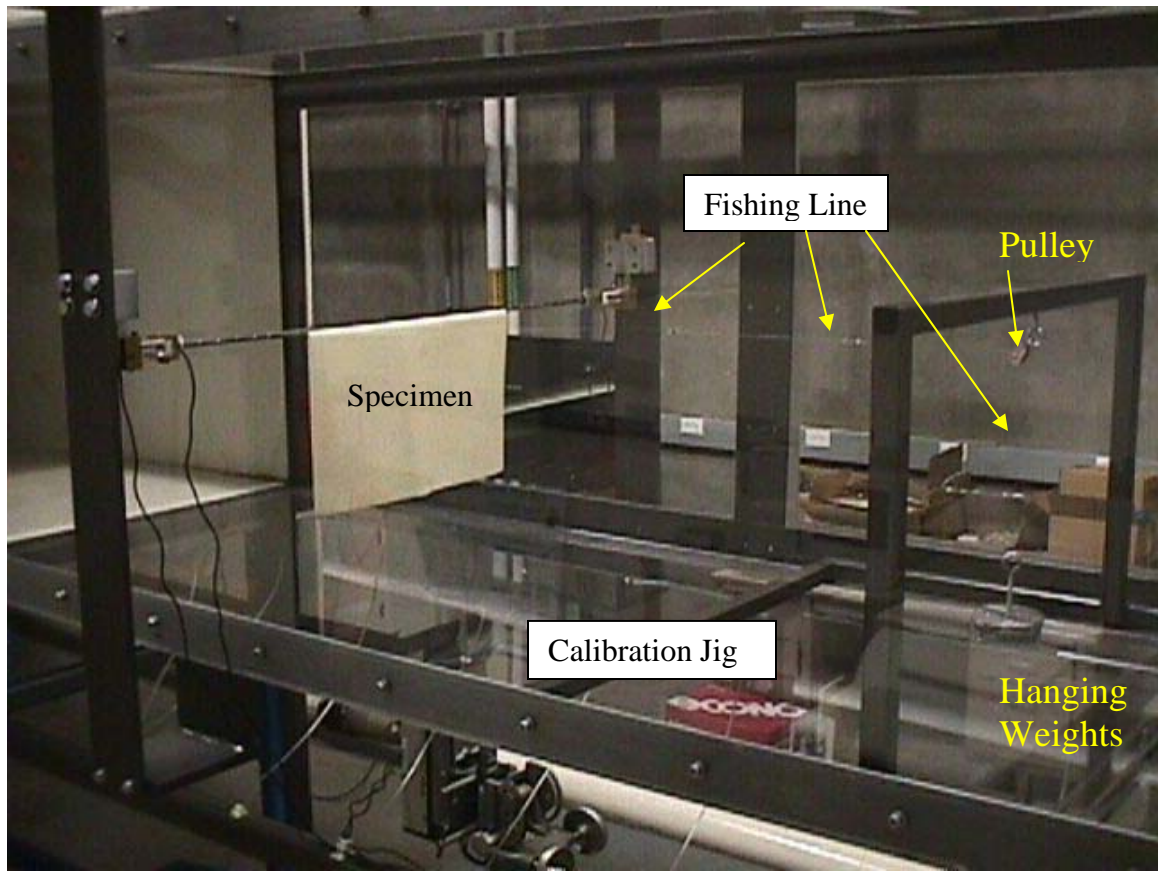
Figure 32. Drag Calibration Set-up

5.)   Calibration data was captured using the data acquisition system and deduced by averaging 6000 data points over a one minute static time period for each hanging weight increment. Calibration tests revealed excellent decoupled lift and drag signals.

6.)   The calibration jig was removed and the access door was bolted shut. A barometer reading was taken. Local pressure and temperature were recorded and inserted into an air property excel worksheet [*Chambers*,

Appendix I], and then saved as a copy into a newly created test case folder.

7.)   The wind tunnel was ramped to the critical wind velocity in increments of $0.02\ in-H_2O$, by monitoring a manometer hooked in parallel with the pitot pressure transducer. Drag data was sampled every $10\ ms$ for one minute. Once the drag PC was initiated, frequency data collection (PC #3) was started. Data was collected at 500 Hz $\left(\Delta t_{sampling}=2\ ms\right)$ until $2^{15}=32,768$ data points were captured. After initiating the frequency measurement, the high speed camera was used to capture images at 500 Hz $\left(\Delta t_{sampling}=2\ ms\right)$. Images were recorded for 5 seconds and stored onto the cameras internal memory. Playing back the images, two complete cycles of oscillation were saved to disk to reduce the file size.

8.)   The tunnel speed was increasing by $\Delta p=0.02\ in-H_2O$, and step 7 was repeated.

9.)   After the critical velocity data was recorded, the tunnel was ramped down and turned off. At no wind velocity, load cell data was captured again to ensure negligible drift.

10.)   The barometer was read again. Local pressure and temperature were inserted into the air calculator and saved into the test folder. The density computed by the sheet before and after the test was averaged and used in velocity calculations.

4.3   Estimation of the Uncertainty of Drag Force

The experimental drag and lift forces were measured with four identical load cells with the performance specification given by the manufacture. Important specifications are summarized in Table 1 below.

Performance Property	Specification
Capacity	$1.0\ Kgf\ =\ 2.21\ lbf$
Rated Output	$0.933\ \text{mv}/\text{V}$
Nonlinearity	0.02% FS
Excitation Voltage	10 V DC

Table 1. Transducer Techniques LSP-1 Load Cell Specifications

To find the uncertainty of the drag force, the propagation of uncertainty approach is implored, as described by *Holman* (1995). The most insightful drag case (and heavily studied) was for a flexible sheet with a mass ratio $\mu = 1.88$. The material was a heavy "leather" fabric, which exhibited consistent (steady) 2-D deflections for a wide range of wind velocities. To compute the uncertainty of drag force, the calibration equation describing the output force as a function of the transducer output voltage is given in equation (4-3.1) below.

$$F_D = 0.9003(\text{V}) - 0.021 \tag{4-3.1}$$
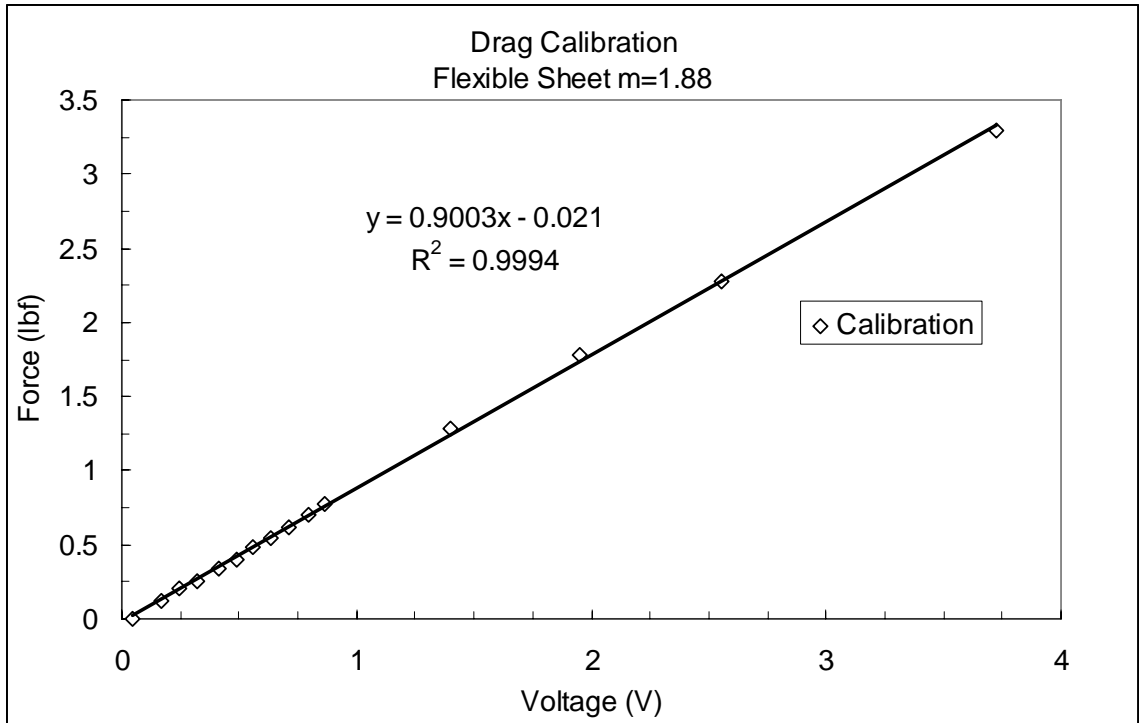
Figure 33. Drag calibration linear curve fit μ=1.88

Equation (4-3.1) is the result of least squares linear curve fit of the calibration data. That is, the output voltage at incremental weight steps using the drag calibration jig, and is shown in Figure 33. This calibration result is dependent upon three related variable uncertainties: 1.) AD board resolution (bit flop), 2.) scale uncertainty when measuring the weights, and 3.) the nonlinearity of the output transducer. To compute the uncertainty at a measurement point, consider the drag results given in Figure 34.
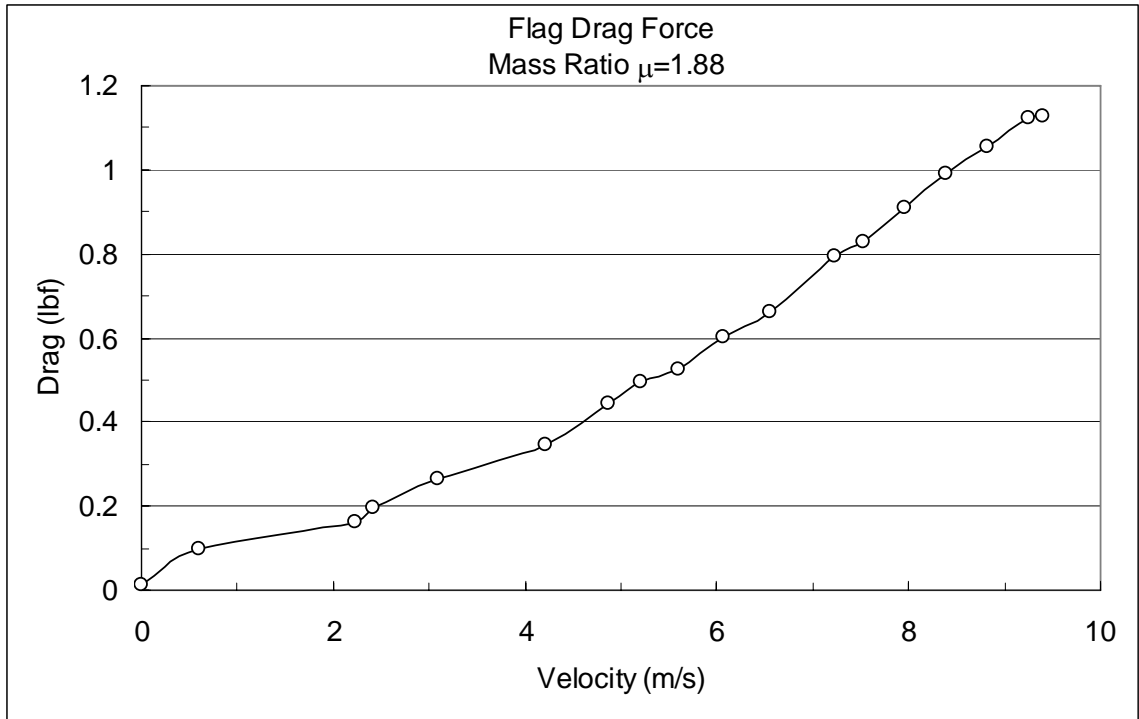
Figure 34. Drag results for heavy sheet μ=1.88

The last data point, $F_D\left(9.4\,{}^m\!/_s\right)=1.13\ lbf$ corresponds to an output transducer voltage of $1.24\ V$. Using this voltage as the nominal output by which to compute the uncertainty, the three variable and their uncertainties are given as:

$$V_{AD} = 1.24 \pm \frac{1}{2^{12}}\mathrm{V} \quad = \quad 1.24 \pm 0.000244\ V$$

$$V_{nonlin} = 1.24 \pm 0.02\% \quad = \quad 1.24 \pm 0.000248\ V$$

$$F_{weights} = 1.13 \pm 0.02\ lbf$$

Fundamentally, the propagation of uncertainty analysis is the square root of the summation of the component variable uncertainty. It quantifies how an individual variable affects the dependent output while holding the other variables constant: The propagation of uncertainty is defined as:

$$\omega = \left[\sum \left(\frac{\partial R}{\partial V} \right)^2 \left(\omega_V{}^* \right)^2 \right]^{\frac{1}{2}}$$

where

$\omega = $ Total uncertainty of result

$R = $ Result function(dependent variable)

$V = $ A varaible of your function

$\omega_V{}^* = $ Uncertainty of variable

In this case, the drag force is measured directly, where the drag uncertainty comes from the voltage uncertainty (from the AD board and the transducer nonlinearity) in addition to the resolution uncertainty given by the scale used to weigh the weights. Applying the propagation of uncertainty, the drag force uncertainty ω_F, is expressed as:

$$\omega_F = \left[\left(\frac{\partial F_D}{\partial V} \right)^2 \left(\omega_{AD} + \omega_{nonlin} \right)^2 \right]^{\frac{1}{2}} + \omega_{weights} \qquad (4\text{-}3.2)$$

$$\omega_F = \left[(0.9003)^2 \left(244 \times 10^{-6} + 248 \times 10^{-6} \right)^2 \right]^{\frac{1}{2}} + 0.02$$

$$\omega_F = (0.000443 + 0.02) \; lbf \quad = \quad 0.020443 \; lbf$$

The percent uncertainty of drag force is $\left(\dfrac{0.020443}{1.13} \right) 100 = 1.81\%$. The maximum experimental drag force for the flag $\mu = 1.88$, can therefore be expressed as $F_D = 1.13 \pm 0.020443 \; lbf$. Clearly, the uncertainty of the scale $\left(\omega_{weights} \right)$ dominates the overall uncertainty of the drag measurement. This calculation is meaningful, in that the

"weak link" in establishing measurement confidence, is not in the transducer, but rather the instrument that was used to calibrate the transducer. Measurement confidence can therefore be increased by using a scale with higher resolution. A similar uncertainty analysis is performed for pitot tube pressure measurement in Appendix F.

4.4   Experimental Results

Light-Weight Flexible Sheet $\mu = 0.704$

A light weight and flexible sheet (lighter than a bed sheet) was first tested. Light weight materials were found to exhibit flutter oscillations at low wind velocities and flutter consistently for only a small range of wind velocities. When the wind speed was increased beyond a critical stability velocity, the flag would oscillate in very unpredictable / sporadic 3-D deformations. In such a situation, the flutter frequency and drag force was seen to drop; as a consequence of periods of momentary fold over. For the first drag experiment, frequency data was recorded and processed immediately by utilizing a LabView auto-spectrum subvi (Appendix H). Figure 35 illustrates the sudden flutter onset and "falloff", over a very small velocity range.
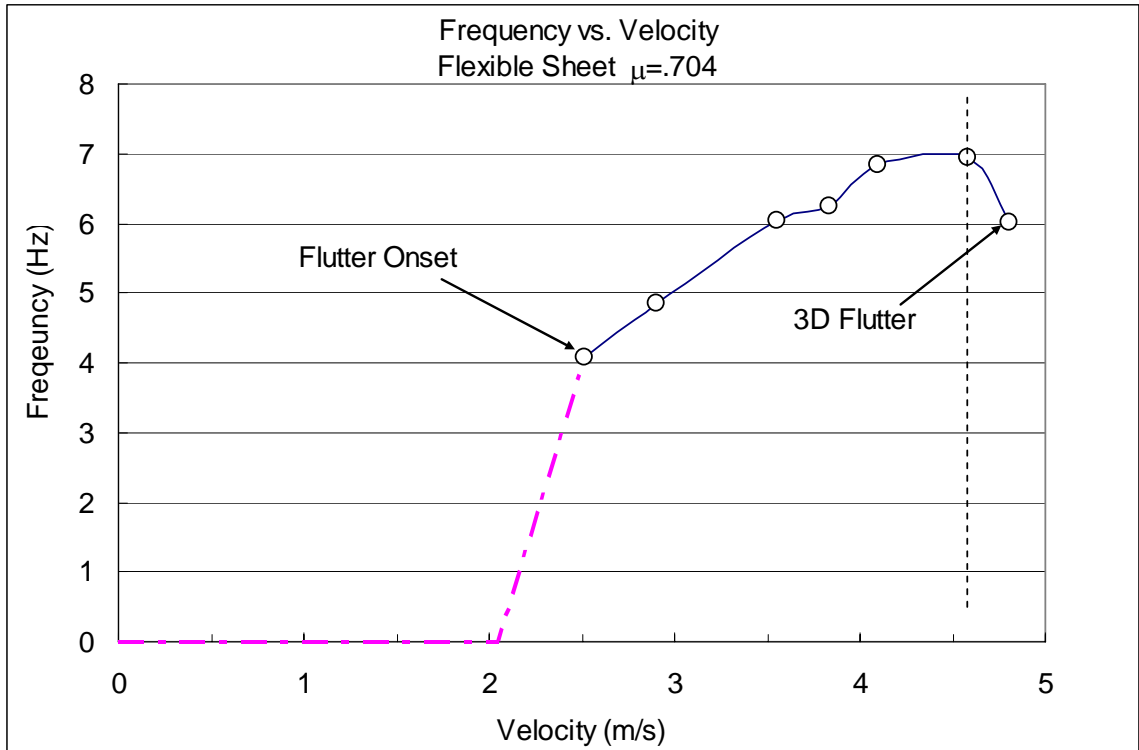
Figure 35. Sudden flutter onset and fall-off for a flexible fabric with very low stiffness.

The drag force behaves similar with the frequency, where drag increases with wind velocity, and drops when the specimen begins to oscillate in three-dimensions. Figure 36 shows the experimental drag force in comparison with an empirical drag prediction given by *Fairthorne* (1930).
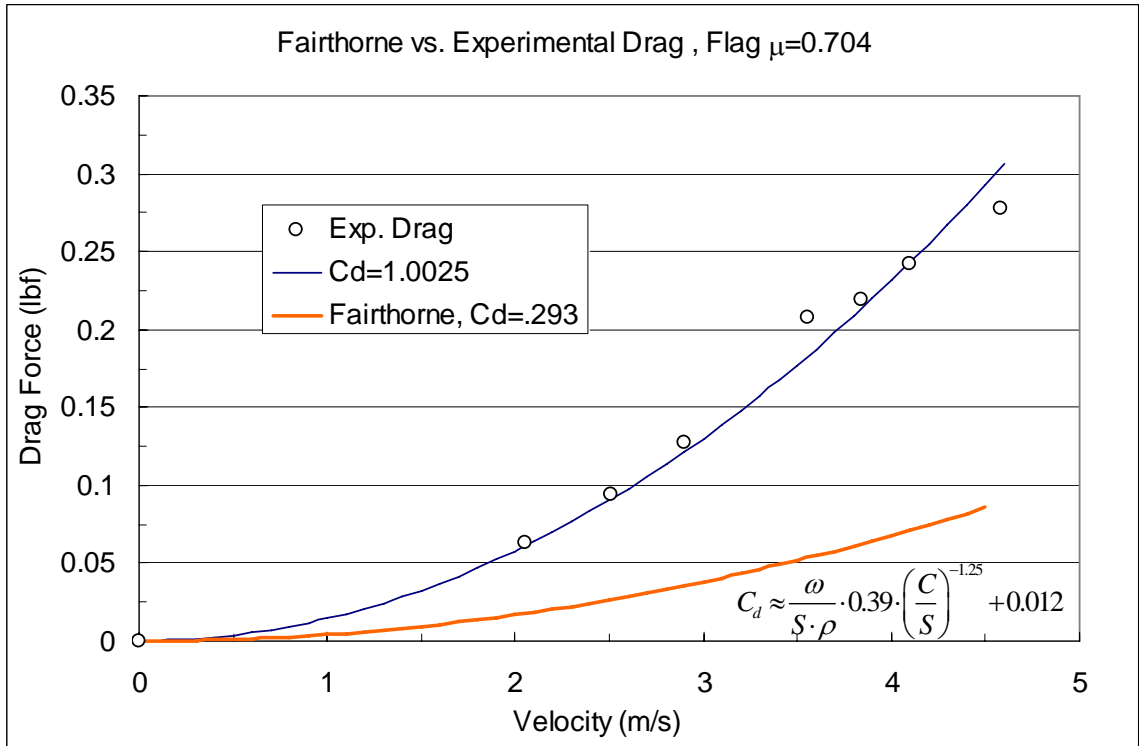
Figure 36. Experimental drag comparison (μ=0.704) with empirical prediction
Fairthorne (1930)

The experimental comparison with the empirical curve given by *Fairthorne*
(1930) shows that the drag coefficient prediction is inaccurate for this light weight flag.
On the contrary, the physics governing drag (dynamic pressure) shows good agreement;
as a fitted line falling near the data can be created by adjusting the drag coefficient. A
reasonable fit was found when C_D was increased to 1.0025. The light weight fabric used
for this test yielded reasonable results, however flutter modes were not always consistent.
This undesirable trait, due to extremely low material stiffness (in both the axial and
transverse direction) was reason enough to experiment with heavier fabrics that would

demonstrate consistent 2-D deflections, allowing ease of study and comparison with simplified 2-D theories.

Semi-Rigid Cooking Board μ =1.74

A flexible cutting board (cooking board) was tested as an opposite extreme to the last material $(\mu = 0.704)$, yet was still capable of flutter. It was flexible enough to bend under its own weight when supported like a flag, but considerable stiffer than the other fabric cases.
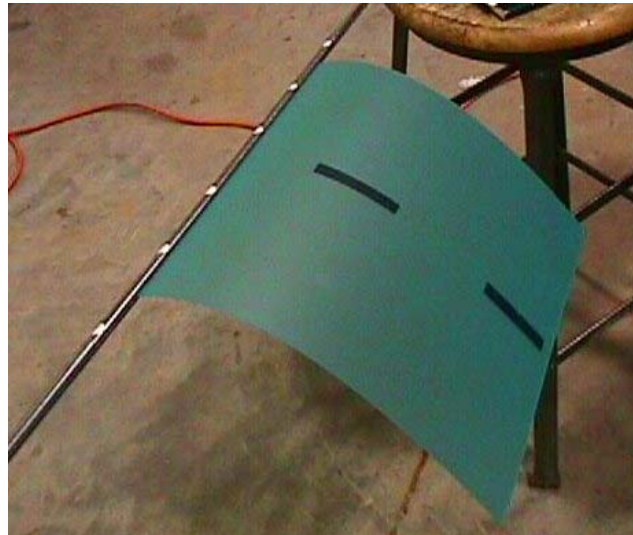
Figure 37. Semi-Rigid Cooking Board

Flutter modes of the cutting board were similar to flexible sheets, however the board did not experience extreme curling at the leech when it reached its maximum potential. Figure 38 shows the fundamental frequency and phase angle for the cooking board. Note that the first flutter data point, was just before symmetric (regular) oscillations, and represents the frequency and phase when the board was just beginning to

oscillate. It fluttered at very small amplitudes ("hovering") just below the horizontal position (level with the pole). At this point flutter onset had occurred regularly, but the effects of gravity were still dominant, and the board would not oscillate upwards (beyond horizontal pole level). The next point however, represents regular (large amplitude) oscillations symmetric about the attachment pole. Thereafter, frequency and phase increase consistently with increased wind speed.
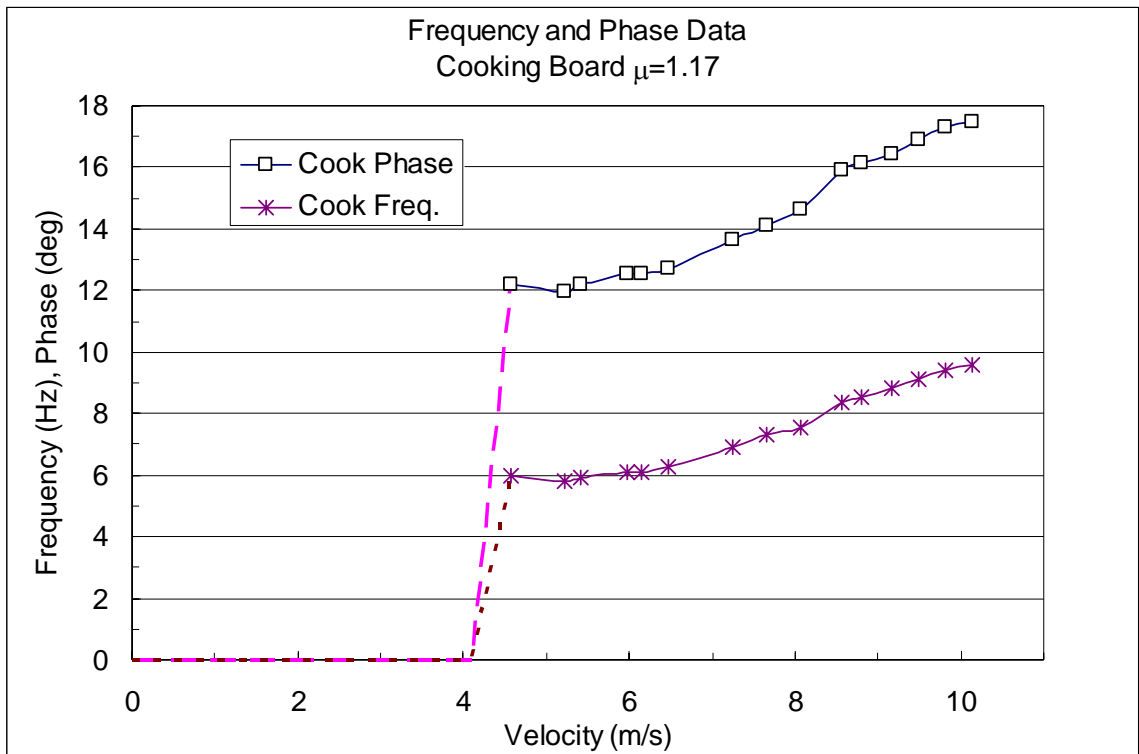
Figure 38. Fundamental frequency and traveling phase angle (cutting board μ=1.17)

The flutter onset is seen more clearly from the drag results shown in Figure 39. As expected, the drag force is very low at low wind velocities (as the board is being raised), and jumps to almost 5 times its value upon the first flutter onset.
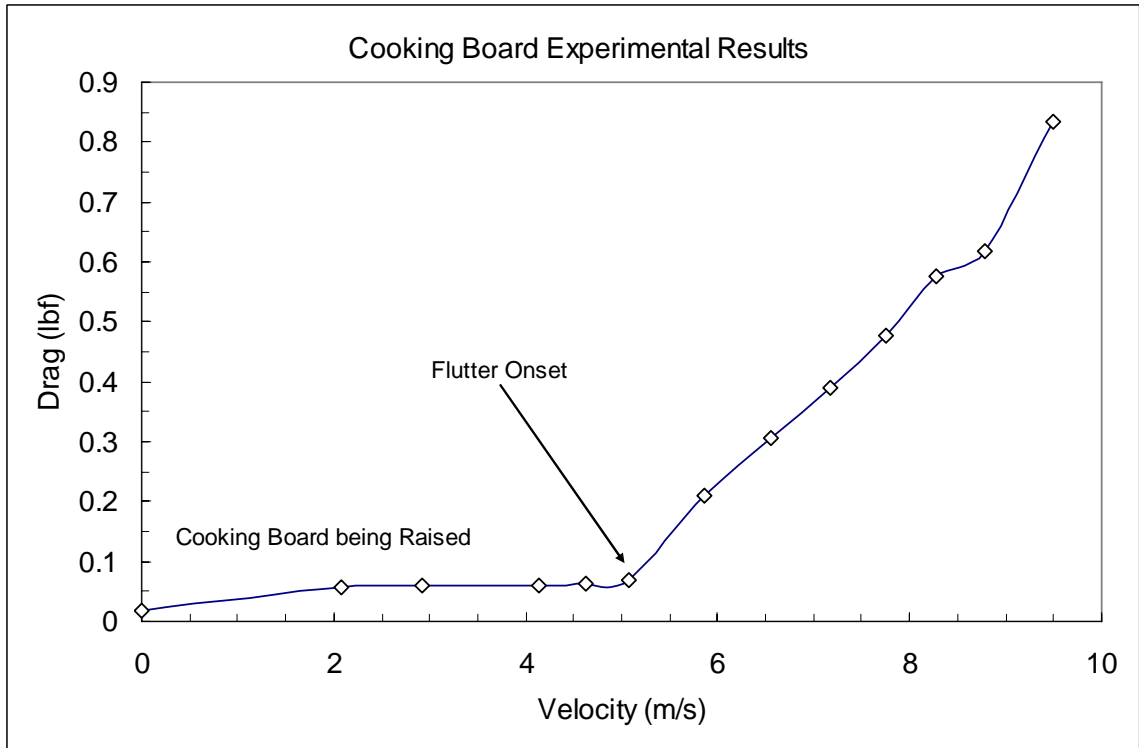
Figure 39. Cooking board drag results

Heavy-Weight Flexible Sheet μ =1.88

The "heavy weight" specimen is an upholstery type leather, that is dense, but also very flexible. This specimen underwent the most testing and analysis due to its consistent 2-D deflections over a wide velocity range and its ease to photograph clearly with the high speed camera. Recalling the importance of the fluid flow field from the stiff-vane results in Section 3.2, the velocity wake of the fluid can give both qualitative and quantitative information about the drag force. The larger the wake field (disturbed flow) and the magnitude of the velocity drop translates to larger drag forces at the

attachment pole. Figure 40 and Figure 41 illustrate the specimen orientation in the tunnel and the velocity wake that results from the fluttering specimen.
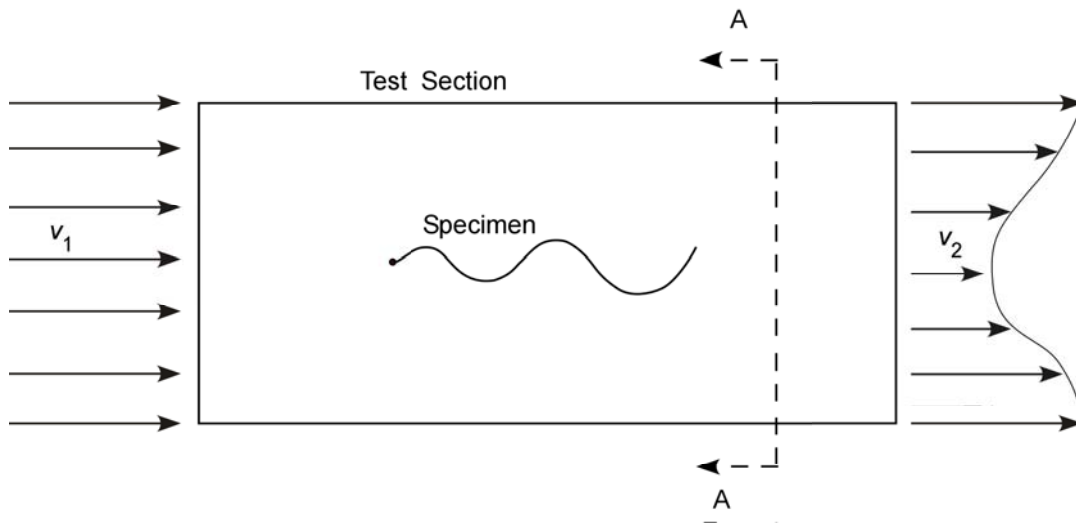
Figure 40. Schematic of the wind tunnel and test specimen
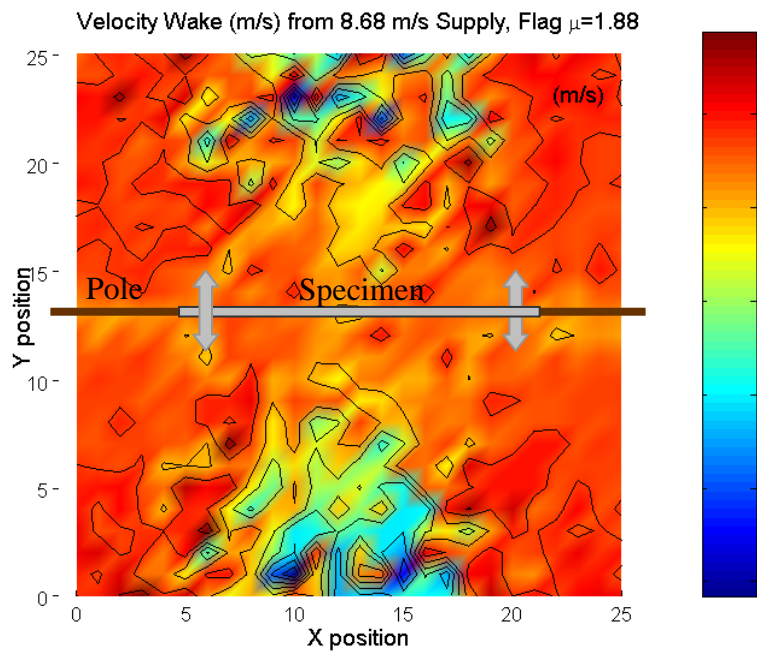
Figure 41. Velocity wake of fluttering specimen μ=1.88

Figure 41 represents section A-A from Figure 40, and shows a relatively calm area along the horizontal pole axis, and areas of large velocity differentials just above and below the fluttering specimen. In these areas, turbulent vortices are created from the specimen whipping violently and shedding the fluid. At increased wind velocities, a combinational increase in wake size and pressure drop give way for increased drag force at the attachment pole. The conservation of momentum principle to predict the net drag is applied later in this chapter and compared with experimental load cell results.

With all test specimens, it was found that the onset of flutter occurs suddenly, and increases in a relatively linear fashion with increasing velocity. Figure 42 illustrates increasing phase and frequency with velocity.
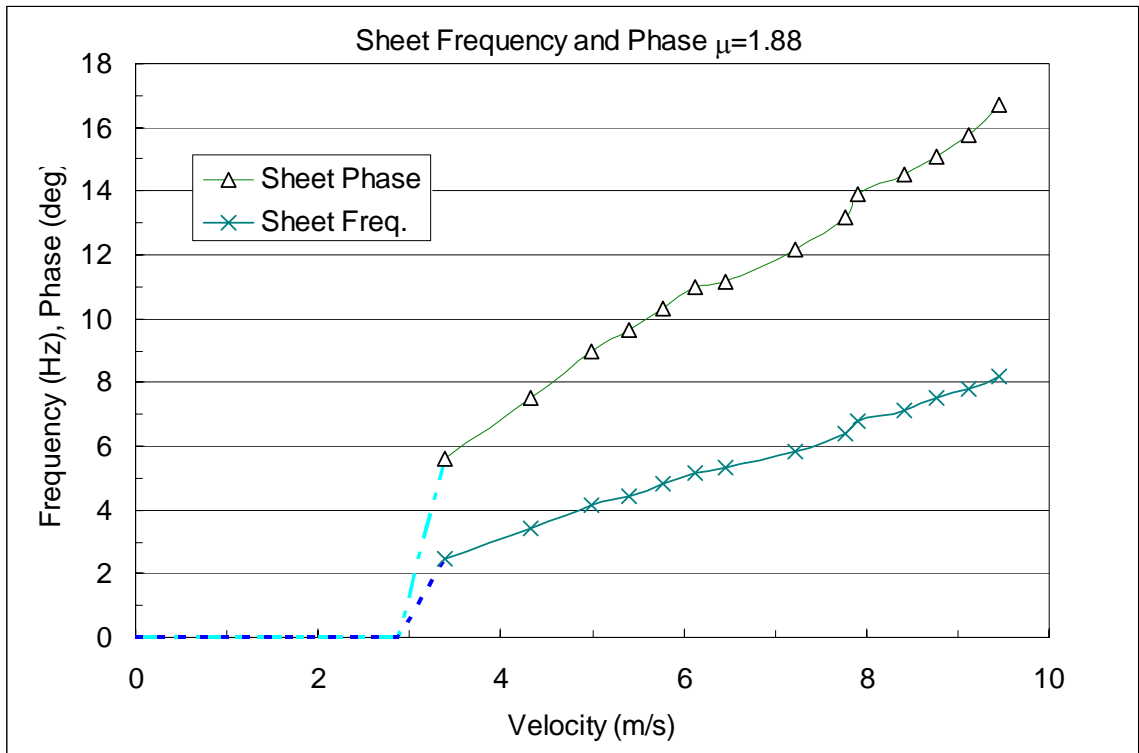
Figure 42. Increasing flutter frequency and phase with velocity (μ=1.88)

Recalling the frequency measurement section, 4.1, the presence of a phase difference between the two vibrometer signals proves that the waving deflection modes are traveling. This test was stopped before 10 m/s due to the violent oscillations (still 2-D) and increased drag force, which was close to exceeding load cell capacities.

Looking closer at the deflection profiles at a wind speed of 8.84 m/s, Figure 43. shows two superimposed images that are separated by 2 cycles.
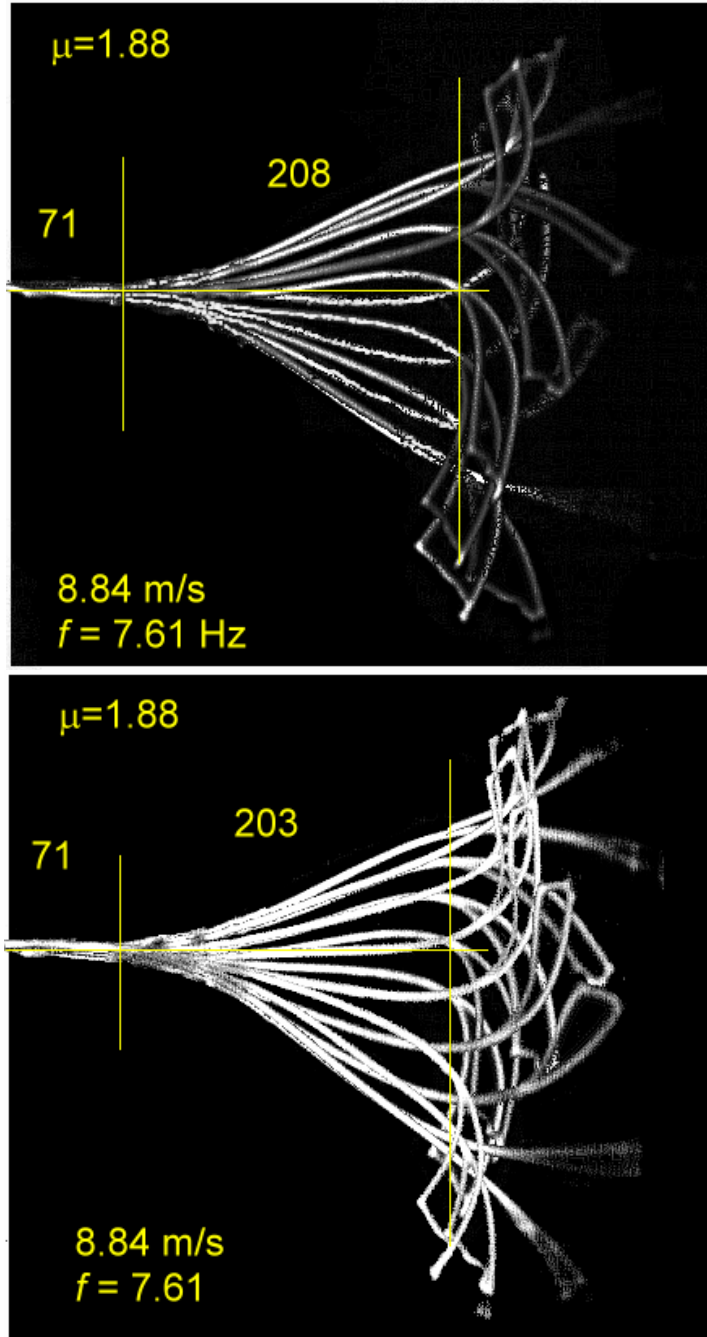
Figure 43. Traveling waves from high speed images separated by two complete cycles

The images illustrate a stationary node 71 pixels from the pole, and a traveling partial node dimension (208 pix vs. 203). This change in node location relates to 0.22 *in.*

and occurs under a half of a second (0.395 sec.). Interestingly, the wavelength is moved backwards slightly (toward the stationary node) suggesting that there is some degree of wave reflection. That is, as the traveling wave reaches the leech and "whips", a small portion of energy is transferred backwards instead of being shed into the fluid stream. The added mass of the flag and the sudden change in deflection direction is likely the cause of this "backlash" effect. These two images only categorize a small sample of this highly dynamic process, however there appears to be a large portion of traveling waves emanating through the small stationary node with some reflective waves.

Considering an image taken at a lower wind speed (8.41 m/s) for the same test, the wavelength is found shorter yet. Without analyzing all image data (which is intensive), it is assumed from experimental observation that the secondary wavelength (partial node) travels back and forth and may be indicative of a large traveling wave being squeezed through the stationary anti-node, which is assumed to have a small "waist" (partial node). The traveling partial node location changes from roughly 170-221 pixels (2.20 in.). Note that this node location is a pivot where the "whip" occurs.
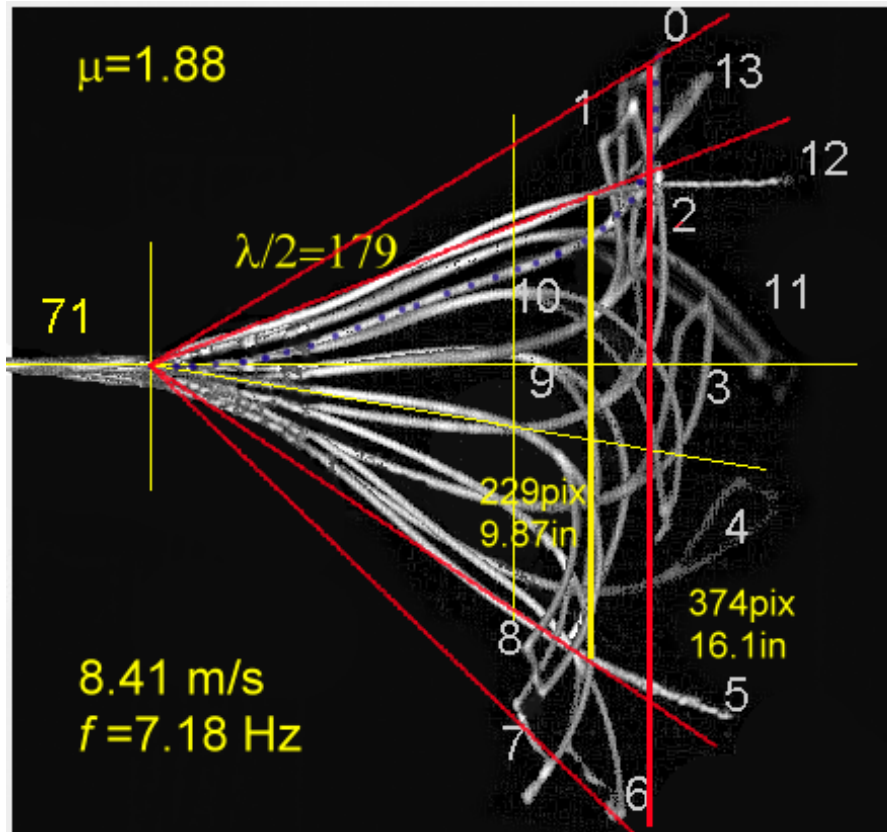
Figure 44. High speed modal data at 8.41 m/s (μ=1.88)

It is hard to quantify the relative magnitudes of traveling and standing waves for this experiment, where we can only see three-quarters of one complete wavelength, $3/4\lambda$. From the image shown in Figure 44 it is not precisely known how best to quantify the relative contribution of standing and traveling waves. Typical studies dealing with the measure of standing waves, will consider the ratio of the maximum amplitude of the incident wave to that of the reduced amplitude as a consequence of reflection. A waveform that is purely standing will not change from period to period and thus has a standing wave ratio of one. The line marker measuring 9.87 in. Figure 44 is a critical dimension/measure of wave mode content. Furthermore, because the specimen is

short (short chord length) and does not exhibit a complete wavelength, the maximum (incident) wave definition is unclear. Additionally, the node at 71 pix is a unique and vague occurrence. It is unclear from the current data, but it is assumed that this stationary node has a small "waist", making the degree of traveling waves substantial. Further complications are revealed when viewing Figure 45, where the inflection amplitude (measured line) changes over two cycles of oscillation. With the additional complication of a varying wavelength (wave number), it becomes necessary to analyze the images over several periods of oscillation where a periodic wavenumber can be identified. As such, it is quite possible that a clear anti-node (waist) is formed at the 71-pixel marker.
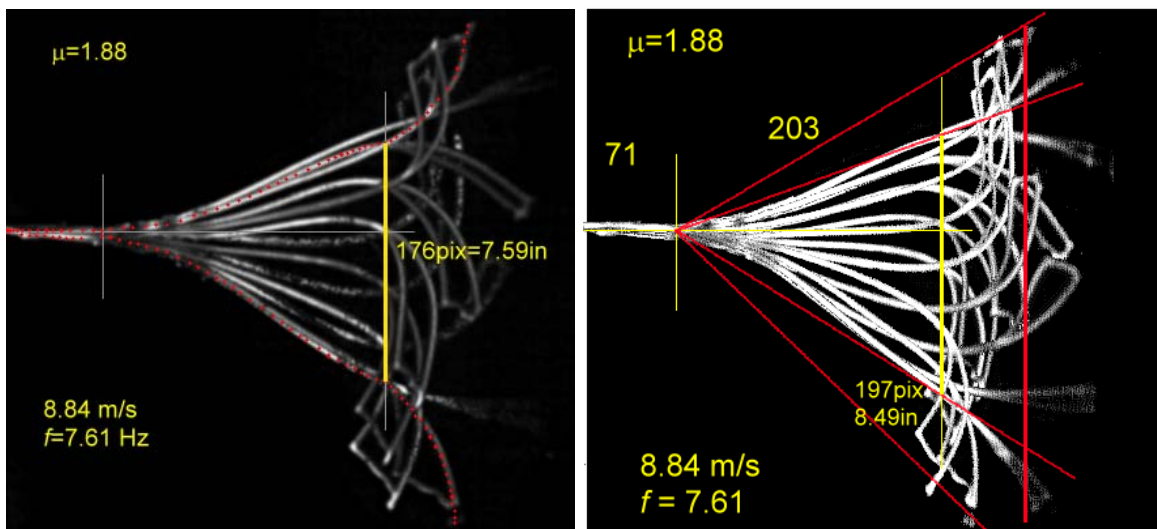
Figure 45. Change in inflection amplitude with wavelength over 2 periods.

Experimental drag data taken for the specimen indicate a clear dominance of drag over lift. Figure 46 shows the averaged drag and lift results, in addition to net (vector) drag.
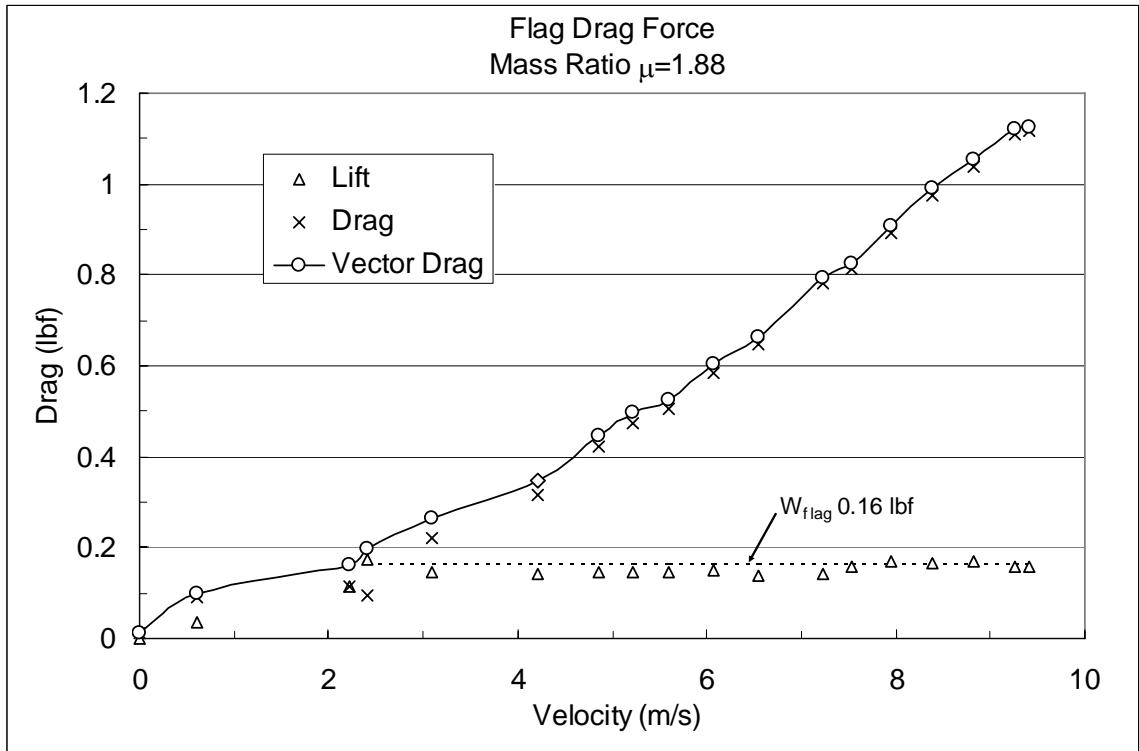
Figure 46. Experimental drag data μ=1.88

Figure 46 shows the flag being raised to a horizontal from the first three data points, and the fourth is the onset of flutter. It is interesting to see that the lift force after flutter onset, is essentially constant throughout the test. Even more insightful, the weight of the specimen: $(0.16\ lbf)$, appears to be the relative magnitude of the lift throughout the test. The fourth lift data point (at flutter onset) is the largest lift magnitude, exceeding the weight of the flag. At this point the destabilizing force has additionally overcome the out-of-plane material stiffness and the in-plane skin friction; both of which are acting (in small magnitude) to stabilize the flag. Notice that after flutter onset the lift force drops,

and remains relatively constant throughout the test. Perhaps the lift forces are small at the attachment pole, because the flag is largely pivoting about the stationary node (71 pix from the left), and most of the lift energy is continually being exchanged into the fluid stream. Furthermore, assuming symmetric flow above and below the flag, it is reasonable to assume symmetric oscillations about the flagpole, and thus the additional force required to keep the oscillations horizontal, is the lift force to support the weight of the flag.

Amplitude measurement at the leech has never been attempted before now, and even in this study is at best, approximate. The defining amplitude of a free edge in flutter is unlike the familiar sinusoid convention and is somewhat ambiguous. For this reason, two amplitude measurements were made with different interpretations of maximum amplitude. For one case, the maximum amplitude was computed as the maximum edge displacement before the "tail-whip" action went into effect. The second interpretation considered the maximum possible vertical displacement of the leech. These two interpretations and the measurement technique can be seen in Figure 47.
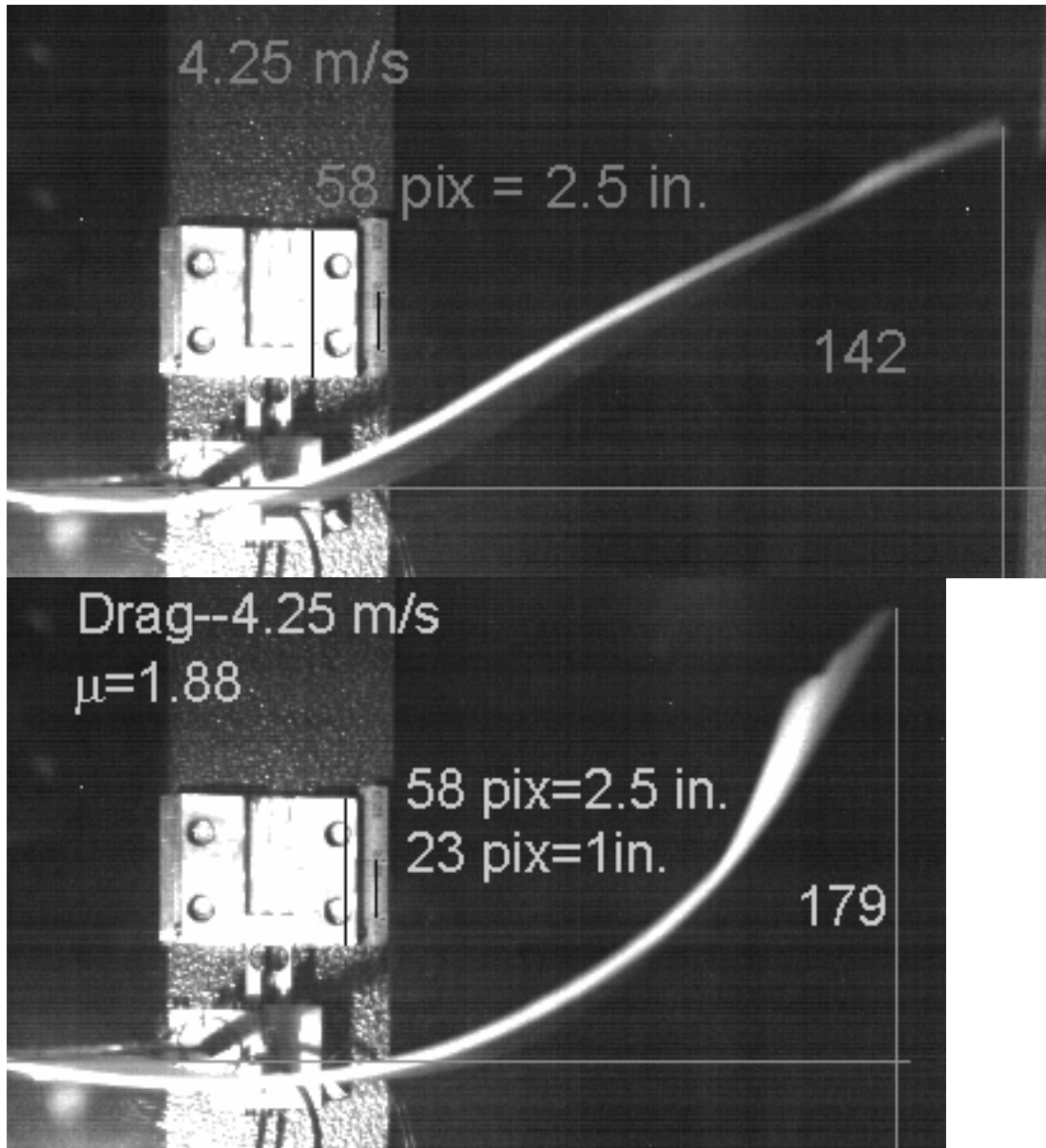
Figure 47. Example amplitude measurement from image data

Clearly, the effect of tail whip allows greater amplitude measurements at the expense of a reduced in-plane chord length. It seems reasonable therefore, to use the average of these interpretations as the effective flag amplitude. Figure 48 illustrates the subsequent amplitude results over a 10 m/s velocity range.
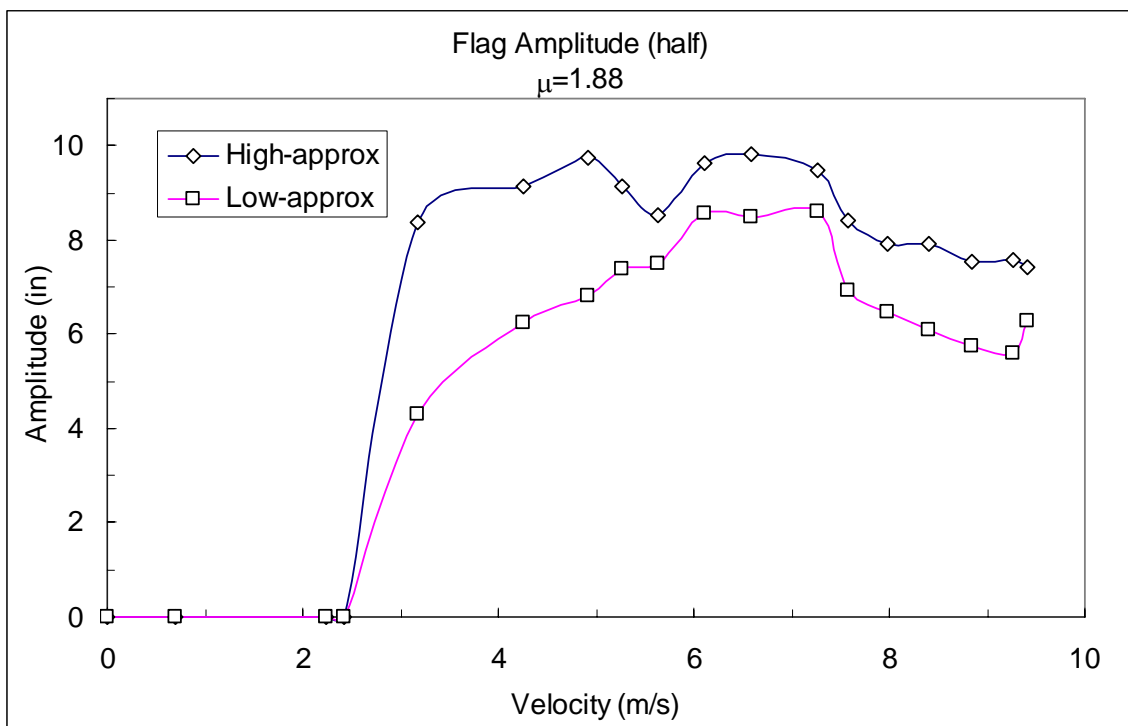
Figure 48. Amplitude results from high speed camera pixel correlation

The results do not indicate a continuous trend, however there appears to be a threshold at which the amplitude decreases. Presumable this is the point at which the induced in-plane tension overcomes the pressure forces invoking the deflection (amplitude). Many researchers have gone around amplitude discussions, while some have assumed that it would increase with velocity up to a horizontal asymptotic limit. It was best explained (predicted) by *Moretti* (2003), by considering the dominance of induced tension. That is, when a flag flutters the amplitude increases from pressure forces acting normal to the flag surface, however at the same time the centrifugal forces from the flag (due to large fabric curvature) opposed the pressure forces. The two

phenomena are fighting each other. The pressure forces impose curvature and promote large deflections, meanwhile the induced tension (in-plane with the fabric) work to "straighten" the flag. At higher wind velocities, the amplitude results show that the induced tension wins, and dominate the total drag at the attachment pole, thereby reducing the amplitude. Analytical drag predictions suggested by *Thoma* (1939 b) and *Moretti* (2003) are compared with experimental load cell data in Figure 49 and illustrate a remarkable correlation, especially considering the first four data points have no flutter frequency $(A = \omega = 0)$. These first four data points represent the initial phase of the experiment where the flag is being raised horizontally (parallel to the flow field).
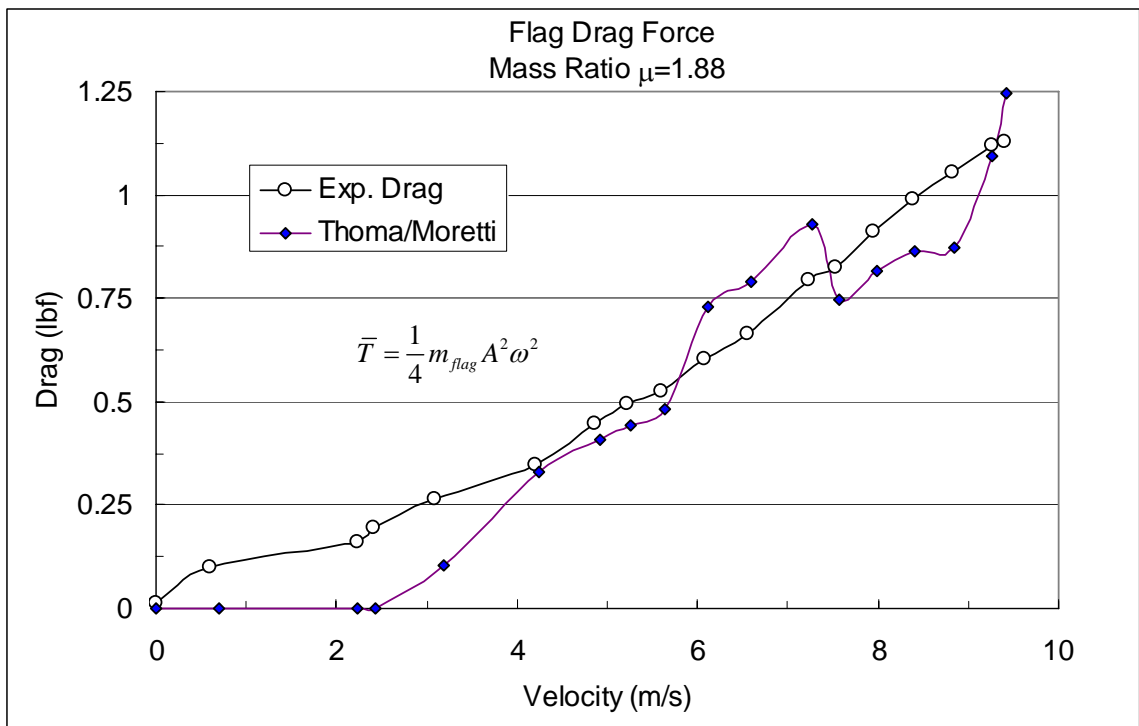
Figure 49. Experimental comparison of drag with theory [*Thoma* / *Moretti*]

To quantify the contribution of the dynamically induced drag (integrated tension) from experimental data, the experimental drag results for the stiff panel (pole+panel) and the current specimen $(\mu = 1.88)$ were approximated mathematically by a least squares curve fit, Figure 50.
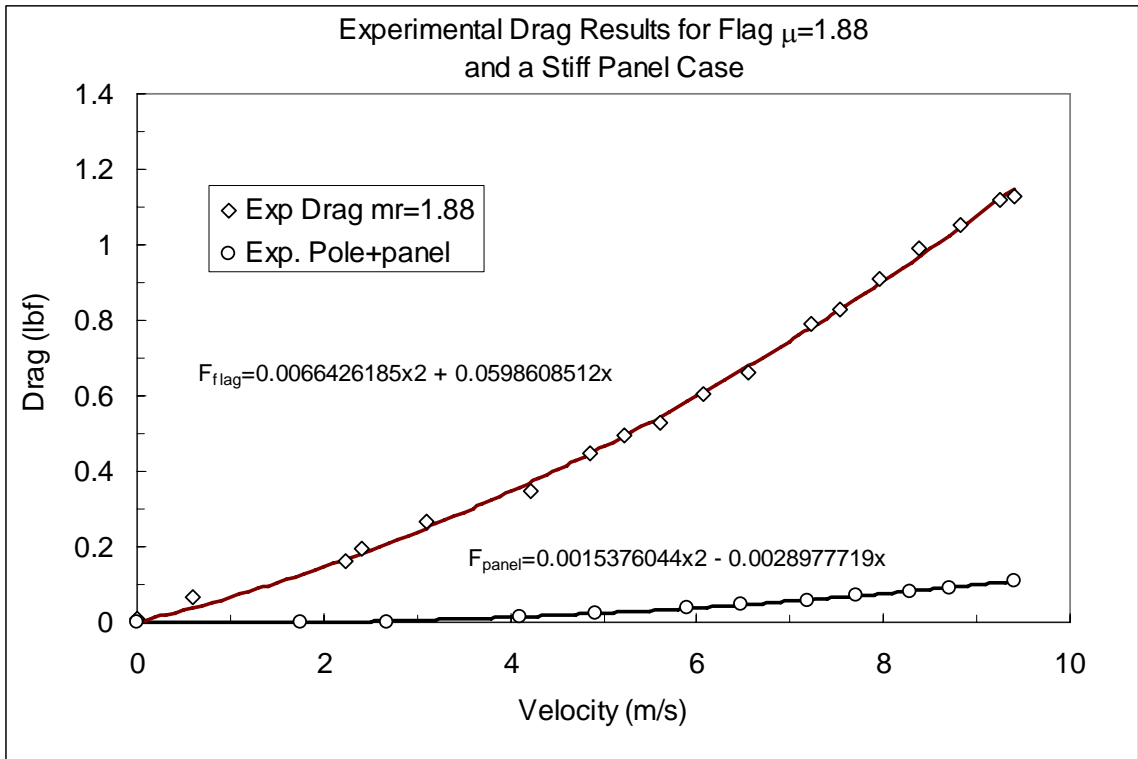
Figure 50. Least squares curve fit of experimental drag data

Performing a curve fit of the experimental data, an approximating 2nd order equation can be used to describe each drag curve more discretely. Subtracting the equations describing the stiff vane case with that of the flag drag $(\mu = 1.88)$, yields the dynamically induced component of drag produced by the flag alone. Figure 51 illustrates the component of dynamically induced drag in comparison with the net drag for the

specimen. Clearly, the flapping motion of the flag generates the dominating component of drag seen at the attachment pole.
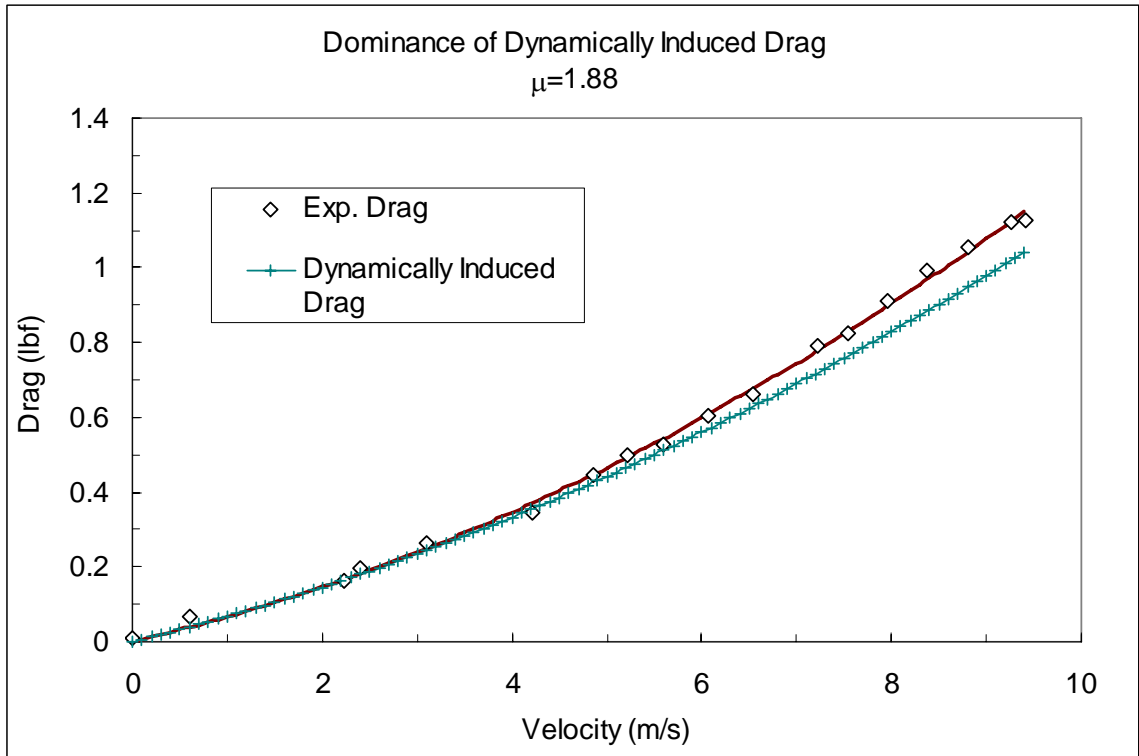
Figure 51. Component of dynamically induced drag μ=1.88

As a last comparison with the empirical formula given by *Fairthorne* (1930) for flag drag coefficients, the drag coefficient for this flag case $(\mu = 1.88)$, was computed and applied to the generalized drag equation (3-1.1). Figure 52 shows experimental drag data plotted against the drag force that results from *Fairthorne's* empirical formula.
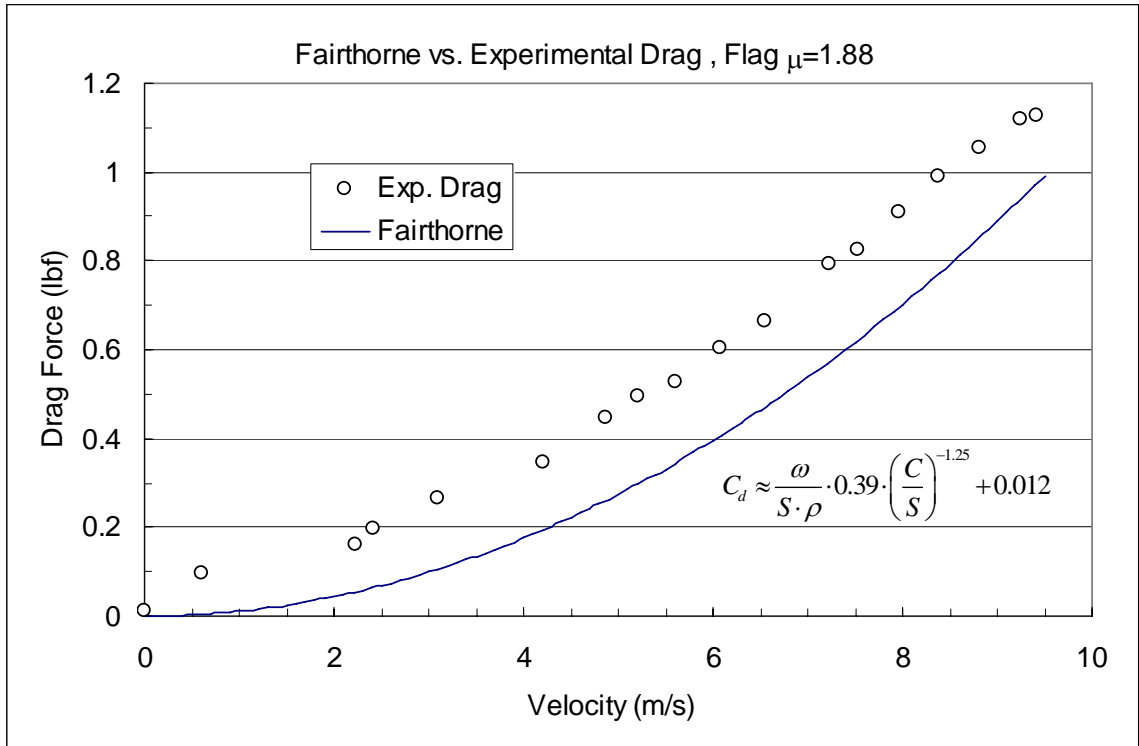
Figure 52. Experimental comparison of drag with empirical prediction [*Fairthorne* (1930)]

Comparing the experimental data with *Fairthorne* (1930), the empirical equation returns a drag coefficient of $C_D = 0.770$, which appears to be shifted from experimental data by a constant value of two tenths of a pound (0.2). This results appears to represent the shape of the drag trend quite accurately, however the trend is consistent because of the generalized drag equation $\left[F_D = C_D \left(\frac{1}{2} \rho v^2 \right) A \right]$. Clearly, the drag coefficient "misses" and the correlation would fall closer to the experimental data if the (constant) drag coefficient were higher. This plot further affirms the accuracy of the dynamic pressure term in the drag equation when computing drag force for various objects.

Fairthorne certainly was on the right track when choosing to formulate a drag coefficient, and let the dynamic pressure term, handle the shape parameter when approximating drag. As mentioned, the dynamic pressure term is also sometimes called the "pressure energy" term, where the energy type is kinetic. This reminder provides additional understanding as to why *Thoma/Moretti's* approximation was accurate. Concisely, the formulation was kinetic energy, and with an intuitive deflection function came the parameters of amplitude and frequency as given in Equation (2-1.4).

Overall Comparison

Bringing all of the experimental data together and making cross-comparisons among the three specimens is important and leads to new insights. Recall that all test specimens had identical dimensions and were tested in the same orientation.
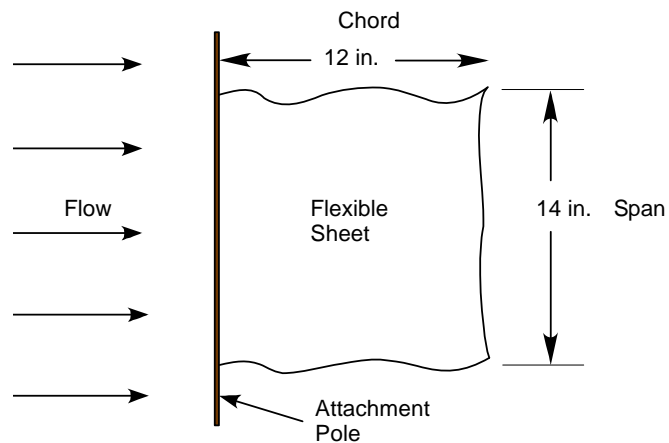
Figure 53 shows the three materials tested, excluding the rigid panel aluminum sheet.
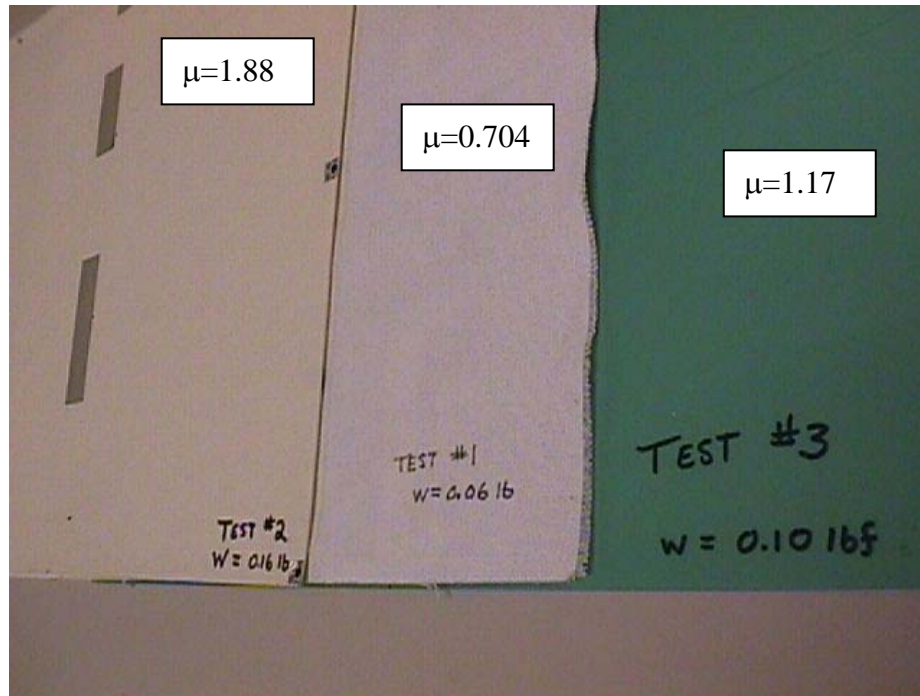
Figure 53. Picture of three materials tested

Beginning with frequency, assuming similar material stiffness, heavier fabrics flutter at lower frequencies than lighter materials and require higher wind speeds to initiate the flutter. Additionally, lighter fabrics experience a faster rate of flutter increase with wind speed. From Figure 54, the slope of the lightweight material indicates roughly a 1.5 Hz change per 1m/s velocity change while the heavier fabric is $0.93\, Hz\!\!\left/\!1\,{}^{m}\!/_{s}\right.$. Figure 54 also illustrates the dominance of material stiffness over weight when classifying flutter onset. The cooking board weighs less than the heavy flag $(\mu = 1.88)$, yet its flutter onset occurs at nearly twice its supply velocity.   The cooking board, once fluttering, experiences the highest initial flutter frequency, but the rate of flutter increase is the

lowest, roughly 0.69 $Hz/1\frac{m}{s}$. This may indicate that stiffer materials have trouble transmitting fast moving waves, resisting curvature (from increased bending stiffness) during oscillations, which would slow flutter frequency propagation with increasing wind speeds.
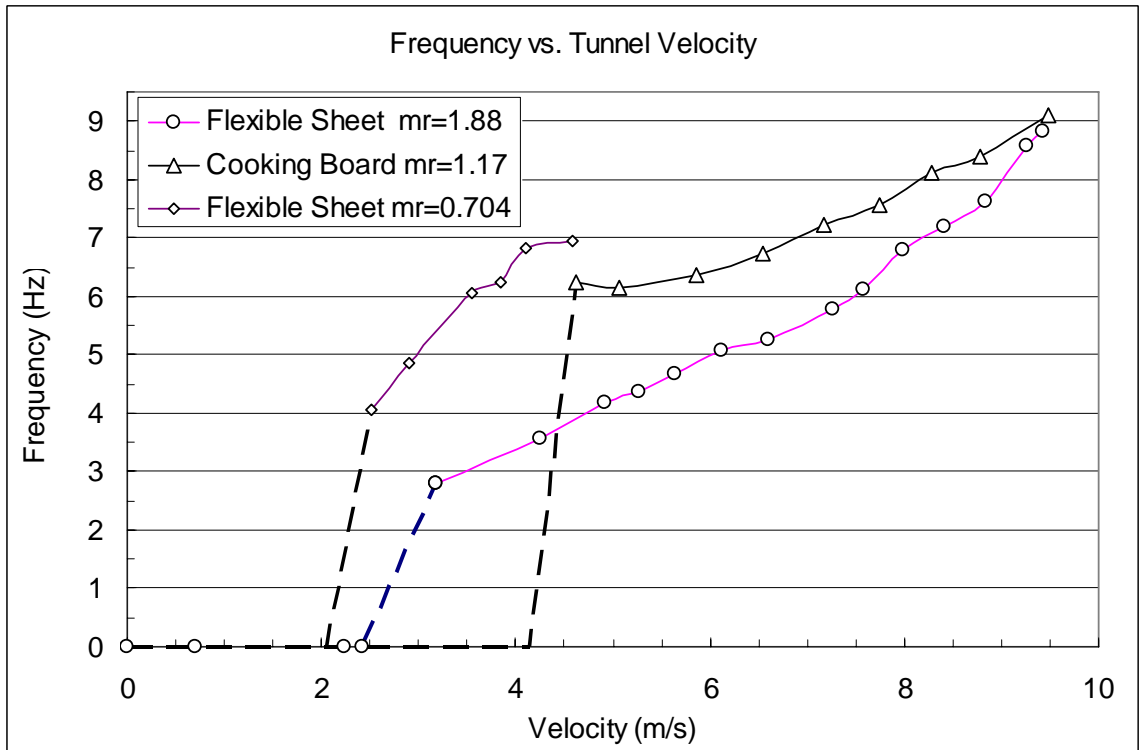
Figure 54. Effect of flutter frequency with material property

Figure 55 illustrates the phase results from the cross FFT analysis. As the wind speed is increased, the phase angle also increases. Similar to frequency, the flexible material exhibits a faster rate of phase change (faster traveling of waves), however the initial phase magnitude is larger for the cooking board. It is seen that the limiting stiffness of the cooking board hinders its growth of amplitude and frequency, thus the flexible sheet is allowed to 'catch up" with the cooking board at approximately 9.5 m/s.

Consequently, this is also the limiting velocity of the leather fabric, before violent oscillations began. It is assumed that all flags with varying stiffness, will have a similar crossover point, where traveling waves are limited (at a critical point) by the material stiffness. As studied by other researchers and observed over the coarse of this study; material stiffness certainly plays a role in limiting drag (by amplitude suppression), however this study did not explore a large comparison of material stiffness properties. We will show however, (through these two stiffness extremes) that stiffer materials have reduced drag as a consequence of flexural rigidity.
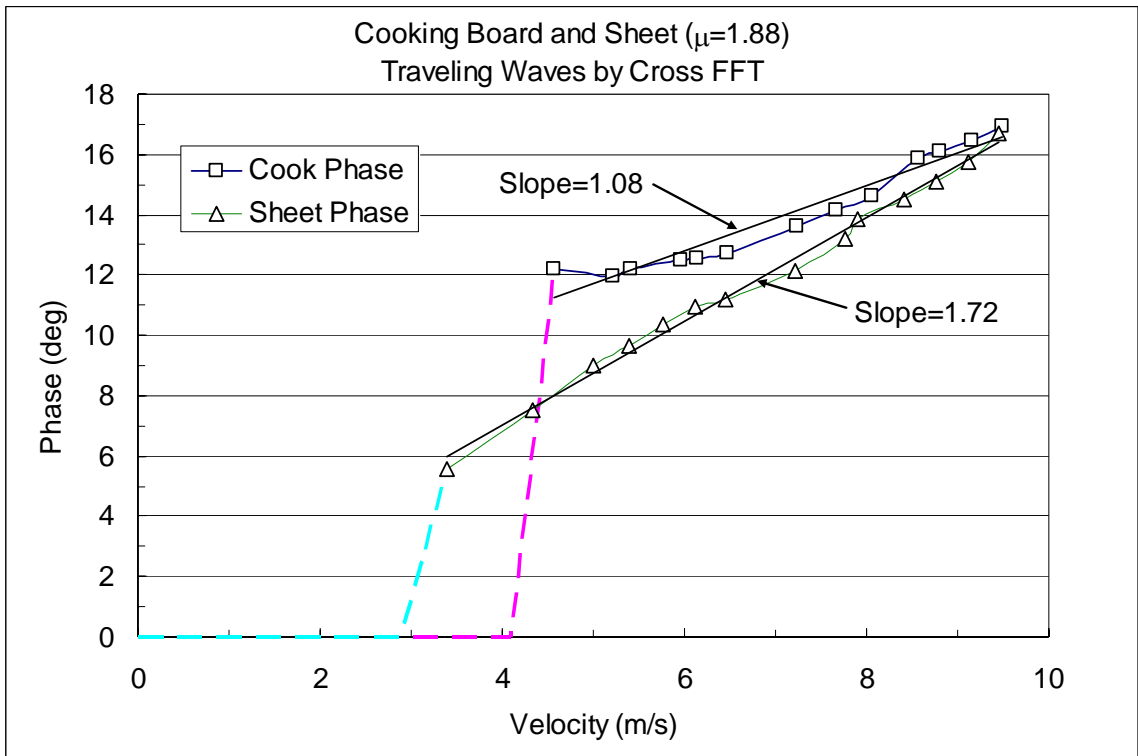
Figure 55. Effect of traveling speed with material stiffness.

Noting the frequency and phase trends from the last two figures, they appear to be related by a proportionality constant. From Figure 56, frequency and phase are approximately related (for both materials) by a factor of 2: $\left[phase \approx 2 \times freq \right]$.
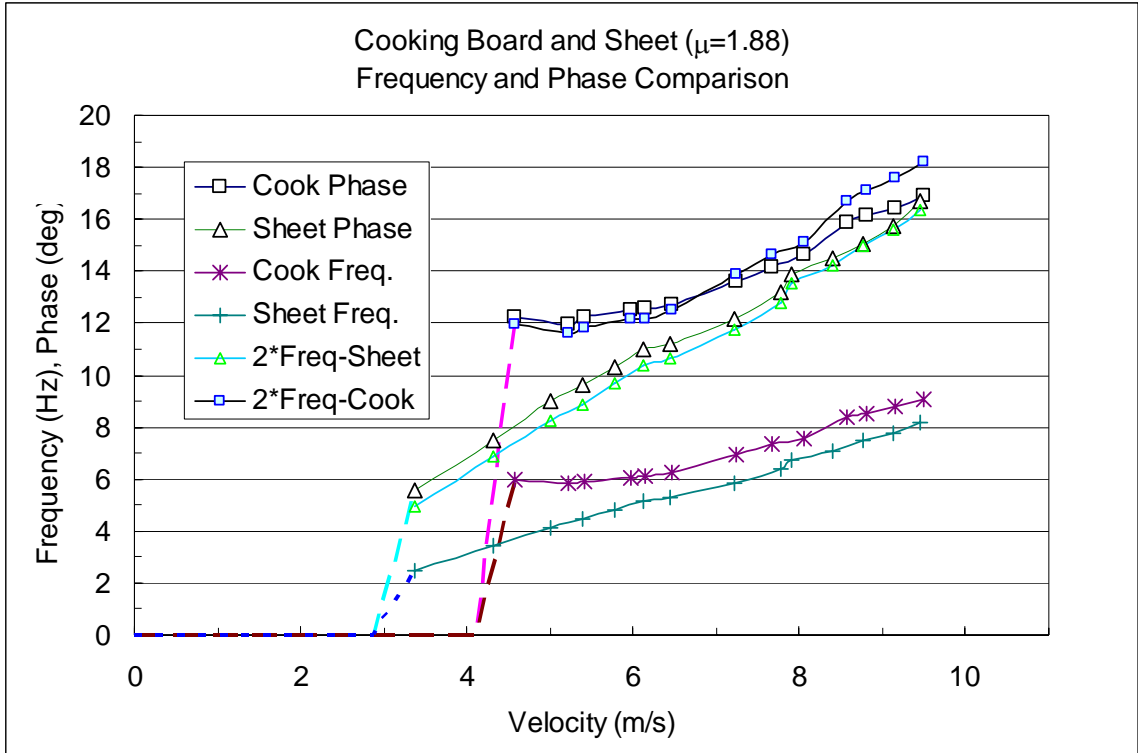
Figure 56. Frequency and phase relationship (cooking board and flexible sheet)

Plotting all drag data together reveals an approximate second-order velocity growth trend, v^2. Consistent with the dominating kinetic energy dissipation $\frac{1}{2}mv^2$, or dynamic pressure term from classical drag formulation $\frac{1}{2}\rho v^2$, the dynamically induced tension is directly related via centripetal acceleration terms. The dominance of dynamically induced drag is clearly seen in Figure 57, where the light weight fabric $\mu = 0.704$, follows a trend of increased drag force in comparison to the heavier cooking

board $\mu = 1.17$. This implies the centrifugal forces from large fabric curvature (deflection) generate the dominating component force, induced drag. That is, the light weight fabric has a much greater centripetal acceleration term (because the mass is lower and yet the force is greater). Due to the flexible motion, the radius of curvature is made small and the flag is accelerated very rapidly; leading to increased (induced) tension.

Recall, centrifugal force is defined as $F_{cen.} = m\dfrac{v^2}{r}$.
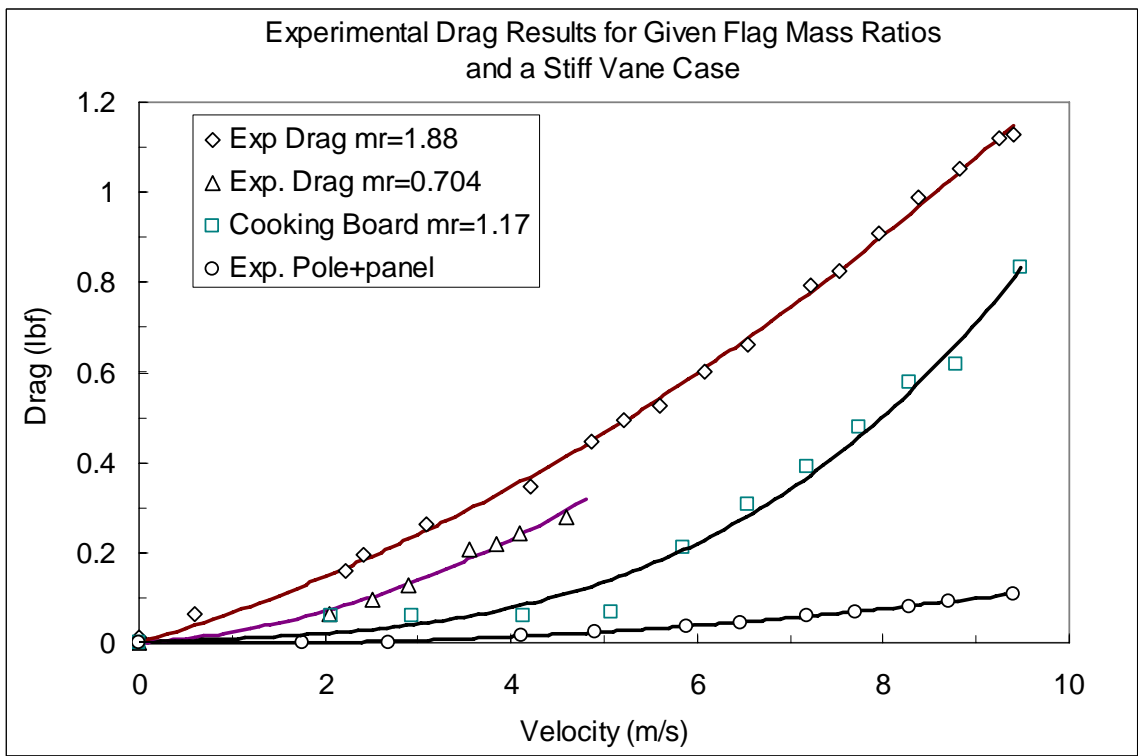
Figure 57. Experimental drag data

The result of subtracting the stiff vane drag curve from the flag drag is the approximated component of dynamically induced drag. Figure 58 illustrates the growth

of drag force with velocity, and shows the component of dynamically induced drag against the net drag for both flexible flag materials tested.
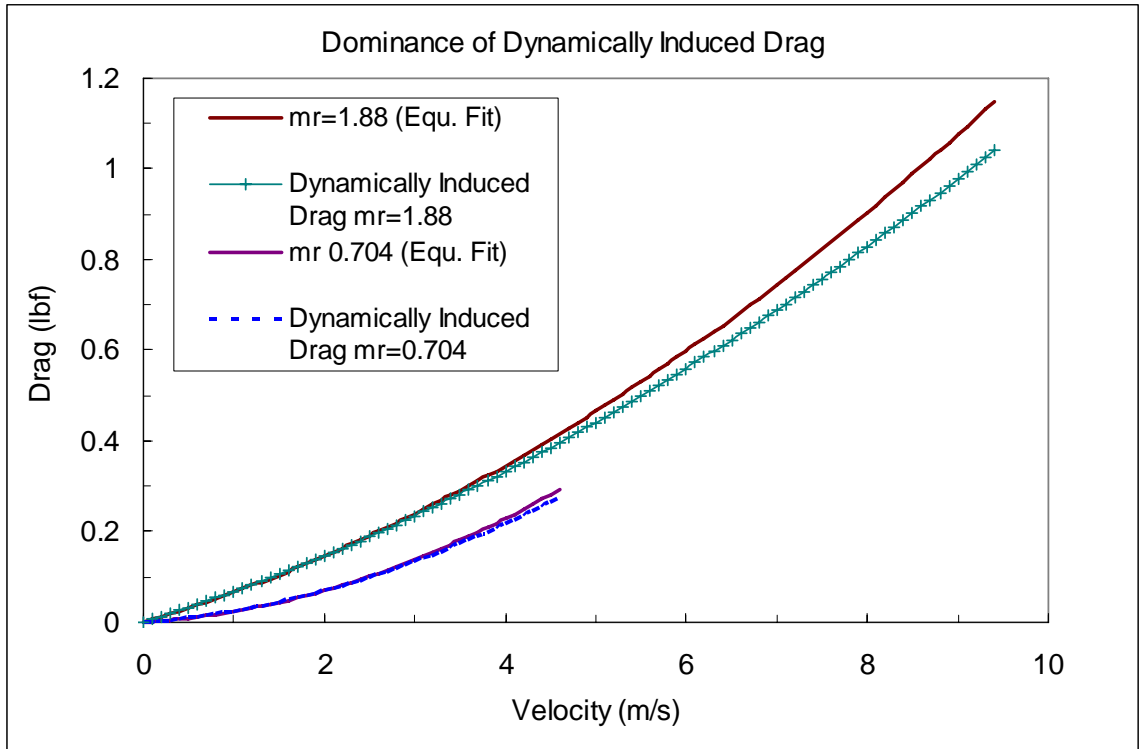
Figure 58. Comparison of net drag with dynamically induced drag

Conservation of Momentum Drag Analysis

With the ease of extracting pressure profiles with an automated pitot traverse setup, the conservation of momentum principle can be utilized as another means to calculate the net drag on a fluttering web. Although this theory is very idealized, assuming two dimensional (potential) flow and neglecting the energy loss from a growing boundary layer along the tunnel walls, we can compare the results to the experimental results obtained from the load cells at the attachment point. Succinctly, the momentum

theory (Newton's second law) says that the sum of external forces on system is equal to

the rate of change of momentum of that system $\left(\sum F = \dfrac{d(mv)}{dt} \right)$. In its precise form,

Roberson (1997) defines the momentum principle as:

$$\sum F = \int\limits_{cs} \bar{v}\rho\bar{v}\bullet d\bar{A} + \frac{d}{dt}\int\limits_{cv} \bar{v}\rho d\forall \qquad (4\text{-}4.1)$$

For the case of the present wind tunnel test, we will assume steady flow through

the control volume $\left(\dfrac{dQ}{dt} = 0 \right)$, so the unsteady term drops out of Equation (4-4.1). For

air moving through the wind tunnel, we define the fluid momentum at one cross-section

as:

$$momentum = \dot{m}v_1 = \left(\rho v_1 A_1 \right) v_1$$

where :
$\dot{m} =$ mass flow rate
$v_1 =$ fluid velocity
$\rho =$ density of the fluid
$A_1 =$ cross-sectional area

With the prescribed assumptions, the momentum principle can be written as:

$$p_1 A_1 - p_2 A_2 - F_D = -\left(\rho v_1 A_1 \right) v_1 + \left(\rho v_2 A_2 \right) v_2 \qquad (4\text{-}4.2)$$

and is graphically depicted in Figure 59
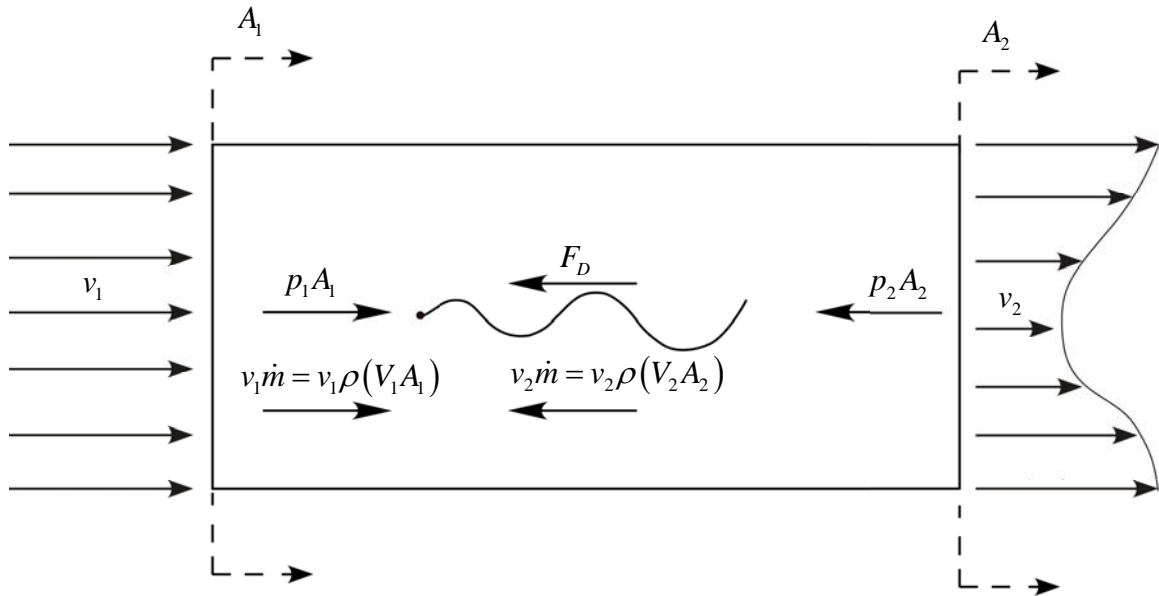
Figure 59. Momentum principle diagram of forces

Simplifying Equation (4-4.2) by converting velocity into pressure (measured experimentally as Δp).

Given:

$$p_1 A_1 - p_2 A_2 - F_D = -\left(\rho A_1\right) v_1^2 + \left(\rho A_2\right) v_2^2$$

And substituting

$$v^2 = \frac{2\left(\Delta p\right)}{\rho}$$

$$\Delta p_1 A_1 - \Delta p_2 A_2 - F_D = -\left(\rho A_1\right)\left(\frac{2\left(\Delta p_1\right)}{\rho}\right) + \left(\rho A_2\right)\left(\frac{2\left(\Delta p_2\right)}{\rho}\right)$$

And simplifying

$$3\Delta p_1 A_1 = F_D + 3\Delta p_2 A_2$$

And since the cross-sections are identical:

$$F_D = 3A\left(\Delta p_1 - \Delta p_2\right) \tag{4-4.3}$$

Equation (4-4.3) describes the theoretical drag force for the object disrupting the flow (attachment pole and sheet) assuming the pressure distribution is constant at the upstream and downstream cross-sections. Experimentally, a $26 \times 26\ in.$ inch area centered on the wind tunnel's $36 \times 36\ in.$ cross-section is traversed in $1\ in.$ increments. Pressure readings from the pitot tube thus discretize the flow field into $1\ in^2$ areas $\left(A^*\right)$. The conservation of momentum is directly applied as:

$$F_D = 3A^* \sum_{j=1}^{26} \sum_{i=1}^{26} \left(\Delta p_{1_{i^*,j^*}} - \Delta p_{2_{i^*,j^*}} \right)$$

or

$$F_D = 3A^* \begin{bmatrix} \left(\Delta p_{1_{1^*,1^*}} - \Delta p_{2_{1^*,1^*}} \right) + \left(\Delta p_{1_{2^*,1^*}} - \Delta p_{2_{2^*,1^*}} \right) + \left(\Delta p_{1_{3^*,1^*}} - \Delta p_{2_{3^*,1^*}} \right) + \ldots \left(\Delta p_{1_{26^*,1^*}} - \Delta p_{2_{26^*,1^*}} \right) \\ + \left(\Delta p_{1_{1^*,2^*}} - \Delta p_{2_{1^*,2^*}} \right) + \left(\Delta p_{1_{2^*,2^*}} - \Delta p_{2_{2^*,2^*}} \right) + \left(\Delta p_{1_{3^*,2^*}} - \Delta p_{2_{3^*,2^*}} \right) + \ldots \left(\Delta p_{1_{26^*,2^*}} - \Delta p_{2_{26^*,2^*}} \right) \\ + \ldots \left(\Delta p_{1_{26^*,26^*}} - \Delta p_{2_{26^*,26^*}} \right) \end{bmatrix}$$

The 5 inch gap between the wind tunnel wall and the outer perimeter of the swept area will not be accounted for, but assumed to have an equal pressure distribution. Experiments reveal that the boundary layer thickness is roughly 2 inches (Chambers 1999). From boundary layer theory and experimental data, the boundary layer will grow as fluid progresses down the length of the tunnel. The increase in boundary layer thickness downstream of the tunnel section will produce larger viscous forces, and hence fluid momentum loss. This loss will create a slight pressure drop from the wind tunnel entrance to the exit. This phenomenon was confirmed by utilizing pressure taps aligned

axially down the center of both the top and bottom walls and recording the local pressure at each tap location with a fast switching scani-valve.
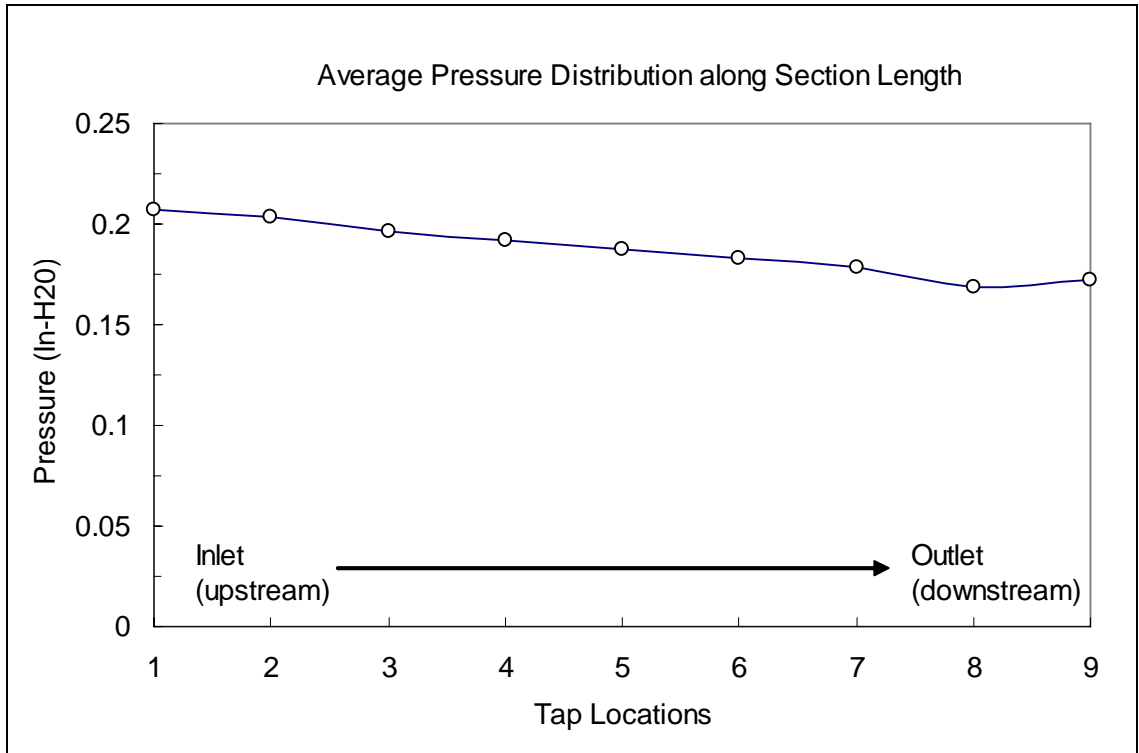
Figure 60. Pressure drop as a result of fluid boundary layer along tunnel walls

Utilizing the pitot tube and traverse setup, the automated sweep program traverses the section and records voltage data from the pressure transducer at each step location. From the voltage data, pressure is computed from a calibration equation, and finally velocity is computed from the pressure readings and plotted. Figure 61 shows a velocity contour plot for a flag specimen $(\mu = 1.88)$ fluttering at 8.68 m/s.

Velocity Wake (m/s) from 8.68 m/s Supply, Flag μ=1.88
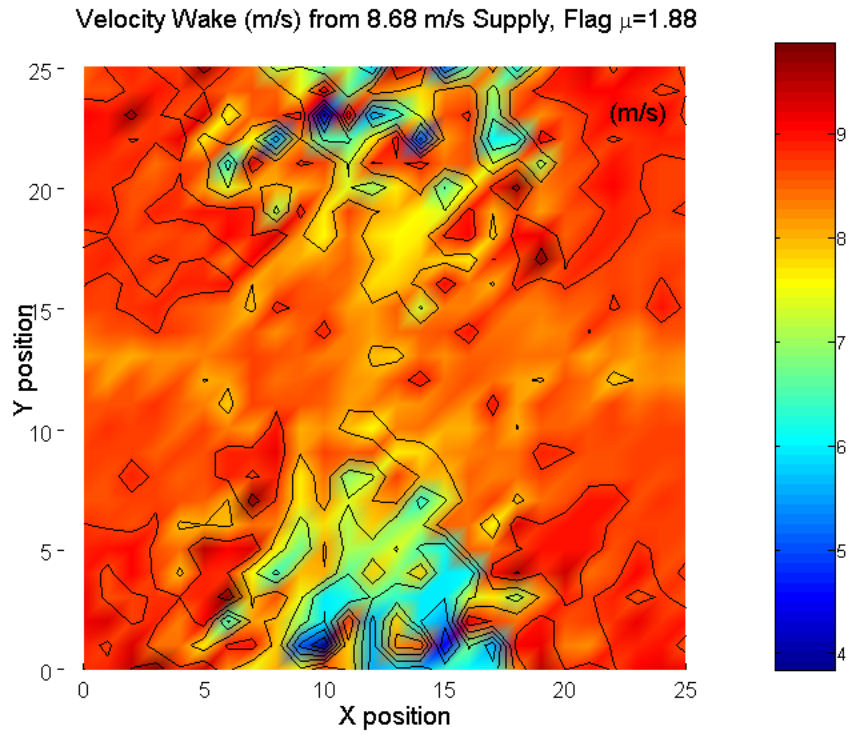
Figure 61. Velocity wake profile at 8.68 m/s.

Velocity Distribution starting at x=0 and moving to x=25
μ=1.88
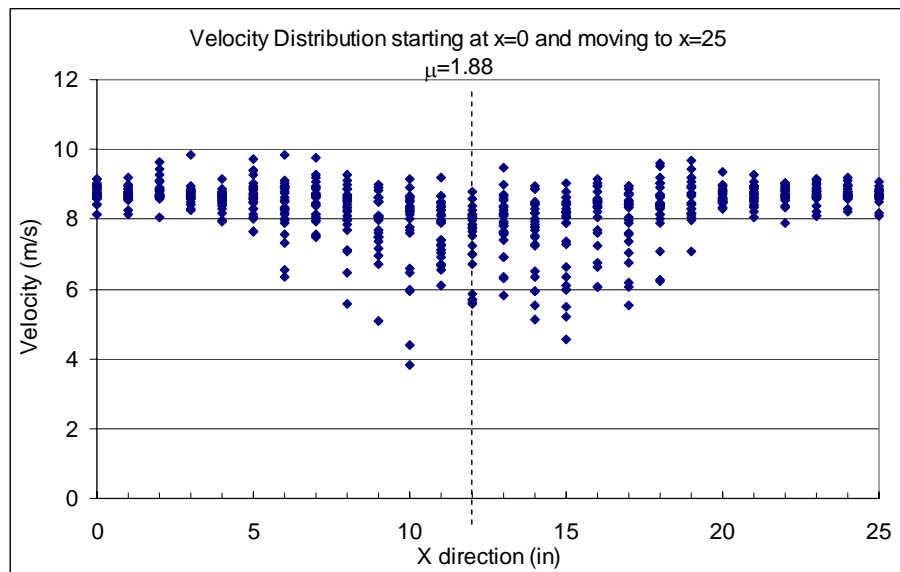
Figure 62. Horizontal velocity profile at 8.68 m/s

The distribution of velocity along the x axis is shown in Figure 62. That is, each column of data points represents all of the possible values of velocity that occurred at that x location. In this way, the shape of the data spread is seen at each x location in the tunnel. A similar distribution in the y direction is shown in Figure 63.
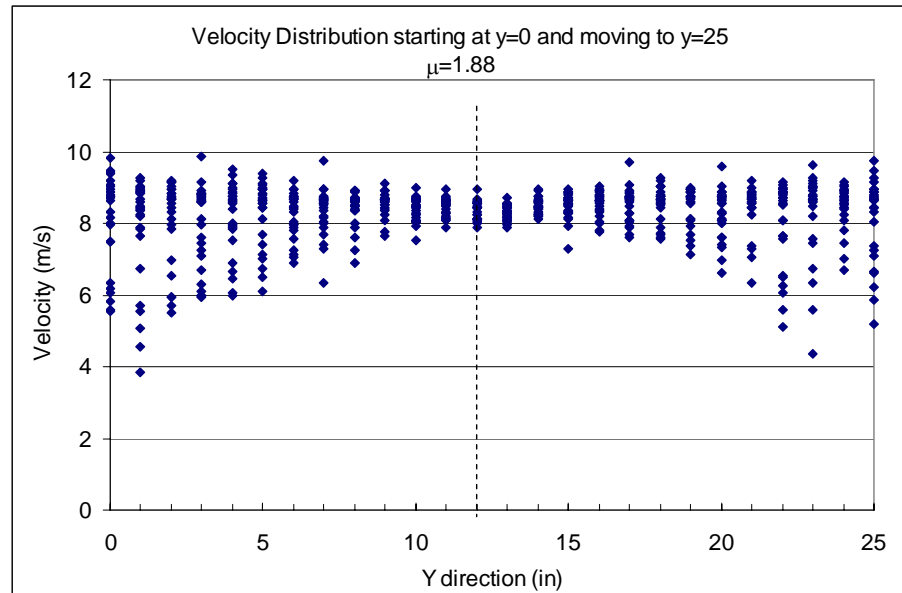
Figure 63. Vertical velocity profile at 8.68 m/s

The results show a relatively stable region along the x-direction aligned with the pole and conversely, a wide data spread in the y-direction, due to the "whipping" of the flag. Applying the experimental pressure profiles captured from the pitot tube, the 26×26 inch data matrix (676 pressure data points) are graphically shown in Figure 64, and will be used for one drag computation $\left(U_o = 8.68 \; m/s\right)$.

.

Pressure Wake (Pa) from 8.68 m/s Supply, Flag μ=1.88

(Pa)

Discretized Pressure Wake-- U_{avg}= 8.68m/s, Flag μ=1.88

Pa
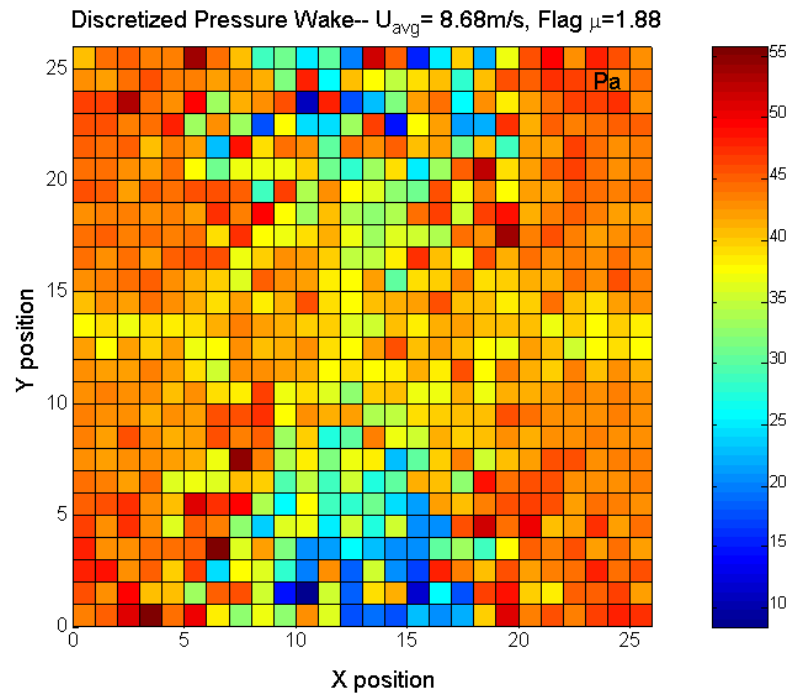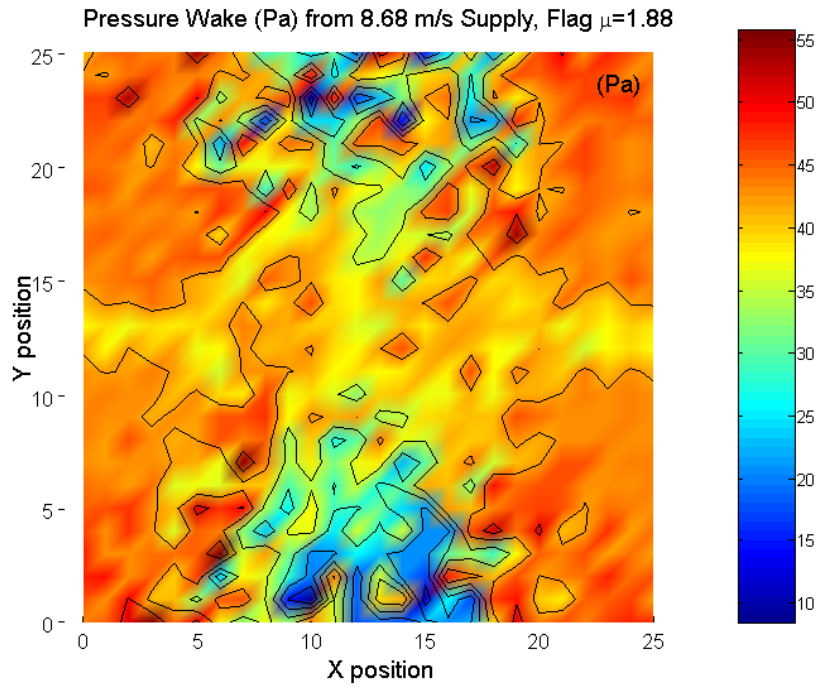
Figure 64. Pressure profile (contoured and discrete) at 8.68 m/s

The momentum equation is then applied by subtracting the free-stream (no flag) pressure profile (Figure 65) from the disturbed pressure wake created by the flag (Figure 64). The summation of all pressure differences (676), is then multiplied by $3A^*$ as given in Equation (4-4.4).
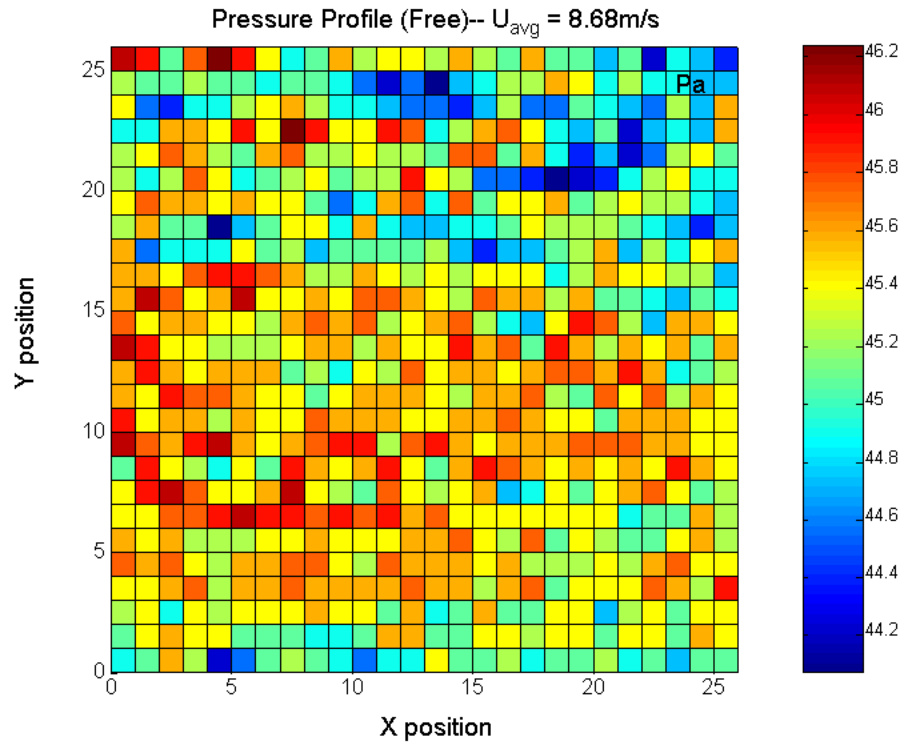
Figure 65. Free stream pressure profile (grid data) 8.68 m/s

$$F_D = 3A^* \sum_{j=1}^{26} \sum_{i=1}^{26} \left(\Delta p_{1_{i^*,j^*}} - \Delta p_{2_{i^*,j^*}} \right) \tag{4-4.4}$$

$$F_D = 3\left(0.000645\,\mathrm{m}^2\right)\left(3225.9\,{}^{\mathrm{N}}\!\!\diagup_{\mathrm{m}^2}\right) = 6.24\,\mathrm{N} = 1.40\,\mathrm{lbf}$$

The result for the pressure profiles given in Figure 64 and Figure 65 for the specimen: $\left(\mu = 1.88\right)$ fluttering at 8.68 m/s is 1.40 lbf. This net drag force corresponds

to one momentum data point shown Figure 66. The results of four other momentum analyses is also shown and plotted against the experimental drag results from the load cells.
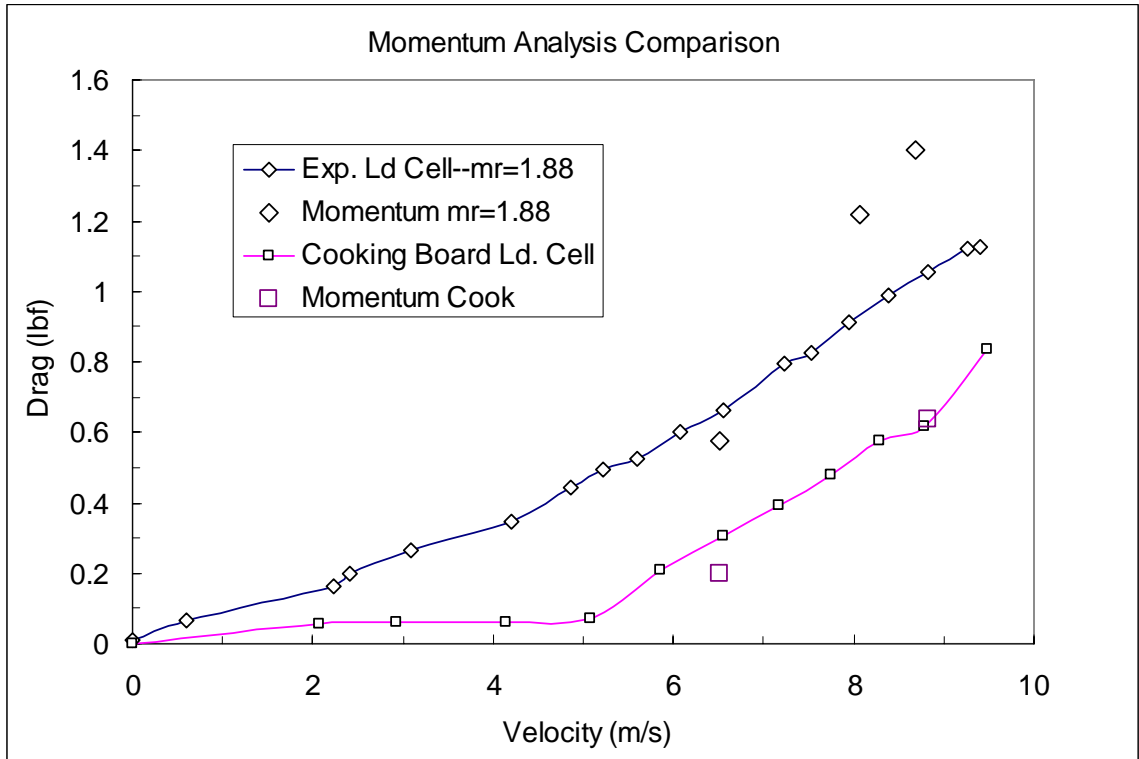
Figure 66. Theoretical momentum drag analysis with experimental results.

Momentum data points were initially taken at velocities where the specimen's oscillations were consistent and fully developed (above 8 m/s). The results for the flexible specimen indicate higher than tested drag results, assumed to be caused by a larger area and pressure drop as a result of the whipping leech. Figure 67 shows the pressure wake from the cutting board from a 8.83 m/s wind velocity. The pressure wake appears to be similar to the flag case (Figure 64), however the flag wake experiences larger areas of sudden pressure drop (especially at the bottom) where the flag whips

backward. Cooking board images could not be resolved from high speed camera data due to the material's dark surface, but from experimental observation, the board was not able to "whip" like the flag due its stiffness. These more 'tamed' (very consistent bi-directional oscillations), are likely the reason for the better correlation to experimental drag results.
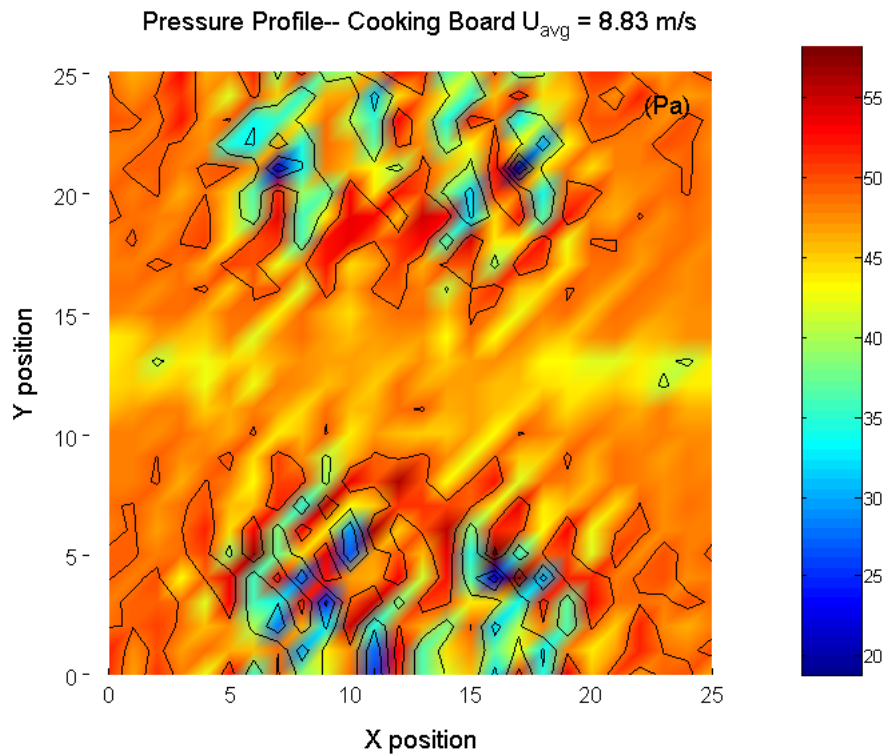
Figure 67. Pressure profile in the wake of a flexible cutting board at 8.89 m/s

Momentum results were not intended to be used to draw experimental drag conclusions, but rather to check (from curiosity) how accurate the theoretical technique could be. Considering the relatively small scale drag magnitudes, the momentum analyses was surprisingly close to experimental drag data for the few cases that were tested, and could potentially be used to 'ballpark" drag if no other force transducers were available.

CHAPTER V

CONCLUSIONS

Drag Overview

When a flag flutters, tension is induced (in-plane) from centrifugal forces due to the flutter motion (out-of-plane). The induced tension acts to "flatten" the flag, however, the pressure forces acting across (normal) to the flag, which generated the lift and induced tension, are fighting to invoke curvature. The flow field generates lift forces on the fabric that induce the in-plane tension, and because the flutter oscillations are symmetrical about the attachment point and normal to the flow field, the time average lift is felt only as the specimen's weight (Figure 46)

We have learned that increased material stiffness leads to decreased drag. Recall the stiff cutting board yielded smaller drag forces when compared with both flexible sheets. Low stiffness in this test setting was even proven to override the inclusion of added mass, as the light weight flexible specimen $\left(\mu = 0.704, \; m = 0.027 \; kg \right)$ weighed less than the cutting board $\left(\mu = 1.74, \; m = 0.045 \; kg \right)$ and yet exhibited increased drag force at the attachment. The large curvature from the fabrics (as a consequence of low material stiffness) yielded large dynamically induced forces. The fact that we see lower drag predictions by using *Fairthorne's* drag coefficient approximation equation suggests that there is a degree of structural stiffening that occurs with a change in flag dimensions.

Furthermore, it was shown that the largest component of drag comes from the kinetic energy dissipation at the leech, which is dependent upon the stiffness of the material (as it limits amplitude). Emphasized again, the centrifugal forces that results from large fabric curvature are reduced in stiffer materials, whereby material flexure is limited.

It has been shown experimentally that the time-averaged tension depends only on the square of the velocity amplitude (at the leech) and the mass of the fluttering specimen. A successful prediction for one case of flag flutter was found using $\bar{T} = \frac{1}{4} m_{flag} A^2 \omega^2$, given by *Thoma/Moretti* (2003). Its origin comes from integrating discretized centrifugal force segments along a curved path (length). Consistent with the derivation, the dominating (induced) drag was found to come from flexible fabrics exhibiting significant curvature (deflection).
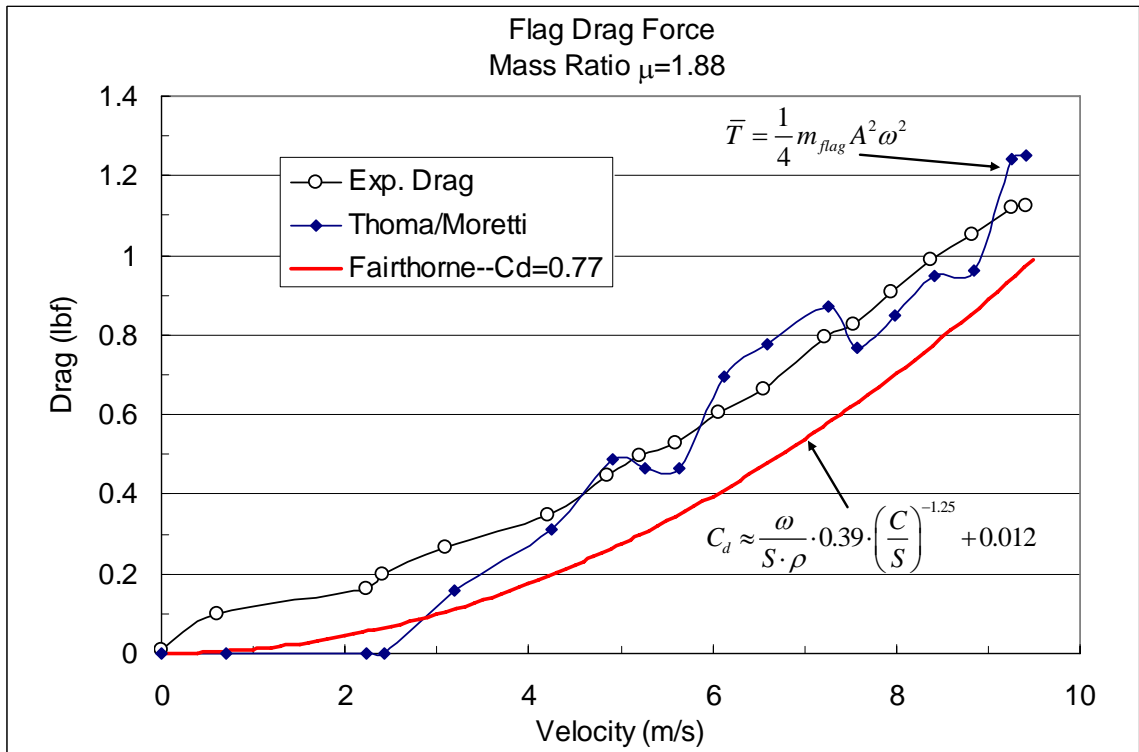
Figure 68. Closed form approximations with experimental data

<u>Wave Characteristics</u>

Vibrometer phase computations and high speed camera images confirm both the presence of a traveling and standing waves. Superimposed images reveal partial traveling nodes and suggest a small stationary anti-node. The combination of such, are indicative of traveling and standing waves, with a wave ratio greater than unity, and an overwhelming dominance of traveling waves. Furthermore, it was shown that stiffer materials flutter at higher frequencies and have larger phase angles, indicating they are able to transmit the fluid energy more efficiently. Stiffer materials have faster traveling waves up to a critical velocity point, thereafter flexible sheets will travel faster. This attribute can again be related back to the stiffness property limiting the natural progression (growth) of the waveform. Interestingly, both the flexible and stiff material tested exhibited a phase angle of approximately twice the fundamental fluttering frequency.

Perhaps a new discovery has come from the ability to measure the amplitude at the leech with a high speed camera. Figure 69 illustrates a sudden increase in amplitude upon flutter onset, followed by a bell shape curve, where the amplitude peaks and tapers off. At this point, it is believed in-plane induced tension from centrifugal forces are competing with the normal pressure forces that create the amplitude deflection. At higher wind velocities, the amplitude results show that the induced tension wins, and dominate the total drag at the attachment pole, thereby reducing the amplitude
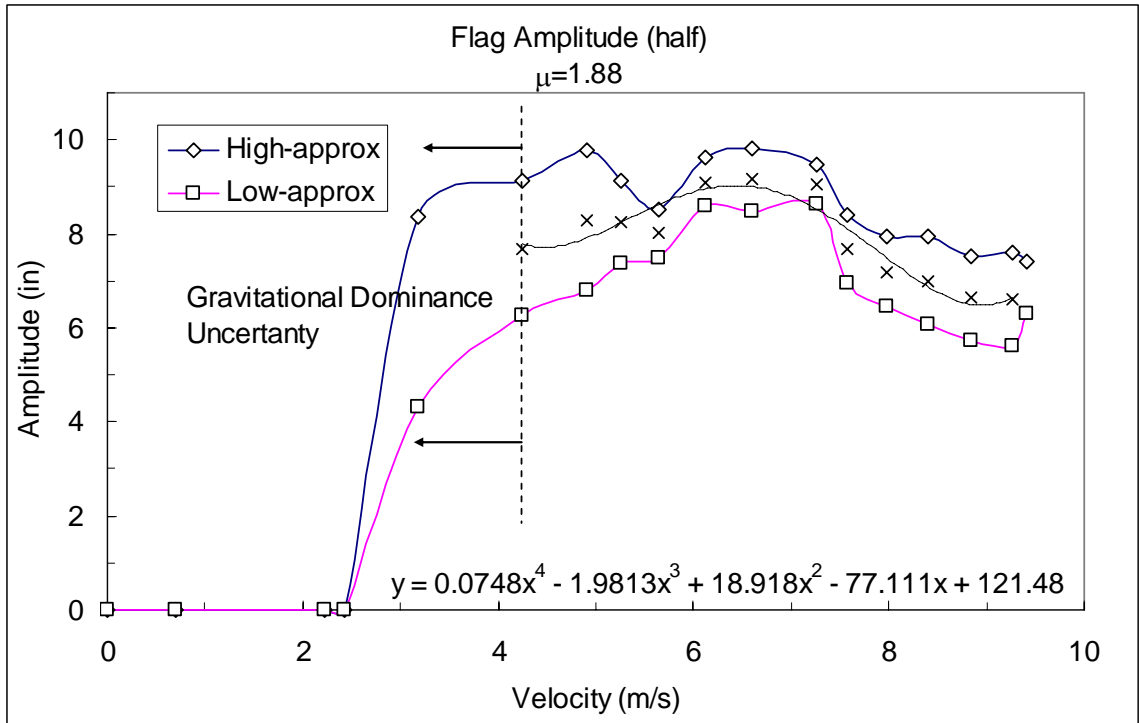
Figure 69. Amplitude shape approximation for measurements at the leech

Figure 69 shows upper and lower approximations for two extremum definitions of amplitude in addition to a median-trend line. It is supposed that in-plane tension, induced from out-of-plane curvature, acts to resist flexure and thus reduce amplitude.

REFERENCES

Bishop, R.H., 1999. *Learning with LabVIEW*. Addison Wesley Longman, Inc. Menlo

    Park, California, pp. 394-404.

Chambers, F.W., 2005. Associate Professor in Mechanical and Aerospace Engineering,

    Oklahoma State University. Private Communication.

Fairthorne, R.A., 1930. "Drag of Flags", Aeronautical Research Committee (ARC)

    Reports and Memoranda No. 1345 (Ae.477), Her Majesty's Printing Office

    (HMSO), London, pp. 887-891.

Hoerner, S.F., 1958. *Fluid Dynamic Drag*, Hoerner Fluid Dynamics, Brick Town, N.J.,

    section 3, p 25.

Holman,.J.P., 1995. *Experimental Methods for Engineers*. New York: McGraw-Hill, pp.

    59-62.

Moretti P. M., 2003. "Tension in Fluttering Flags"*, International Journal of Acoustics

    and Vibration*, Vol. 4, No. 4, pp.227-230.

Mott, R. L, 2000. *Applied Fluid Mechanics*, 5th Edition, Prentice Hall, Upper Saddle, NJ,

    pp. 485-495.

Roberson, J. A & Crowe, C. T., 1997. *Engineering Fluid Mechanics*, 6th Edition, John Wiley and Sons, Inc., Toronto, pp. 429-453.

Taneda, S., 1968. "Waving Motions of Flags", *J. of the Physical Society of Japan*, Vol 24, No.2, pp. 392-401.

Thoma, D., 1939 a. "Warum Flattert die Fahne", *Mitteilungen des Hydraulischen Instituts der Technischen Hochschule Muechen*, No. 9, pages 30-34; translation "Why does the Flag Flutter", Cornell Aeronautical Laboratory, (1949).

Thoma, D., 1939 b. "Das schlenkernde Seil", *Zeitschrift der Angewandten Mathematik und Mechanik*, (ZAAM) No. 19, pages 320-321; translation "The oscillating Rope".

Uno, M., 1973. "Fluttering of Flexible Bodies", *J. of the Textile Machinery Society of Japan*, Vol.19, No.4-5, pp.103-109.

Watanabe, Y., Suzuki, S., Sugihara, M., & Sueoka, Y., 2002. "An Experimental Study of Paper Flutter", *J. of the Fluids and Structures*, Vol.16, No.4, pp.529-542.

Yamaguchi, N., Sekiguchi, T., Yokota, K., Tsujimoto, Y., 2000. "Flutter Limits and Behavior of a Flexible Thin Sheet in High–Speed Flow—II: Experimental Results and Predicted Behaviors for Low Mass Ratios", Trans. ASME, *J. of Fluids Engineering*, Vol 122, pp. 74-83.

APPENDICES

APPENDIX A—WIND TUNNEL TEST SECTION DRAWINGS

VIBRATION DAMPING LEVELING FEET

RIGID SUPPORT MOUNT

STATIC PRESSURE TAPS

DOOR

PITOT TRAVERSE SLOT

GENERAL VIEW

OKLAHOMA STATE UNIVERSITY

TEST SECTION

10/1/05

SCALE 0.047

NO	DESCRIPTION	REQ
1	POLYCARBONATE PANELS 7.9 x 3 ft	4
2	ANGLE IRON 3 x 3 x 0.25 in	56'
3	SQUARE TUBING 2 x 2 x 0.1875 in	60'
4	SWIVEL CASTERS Ø6.0 in	4
5	THREADED LEVELING INSERTS	4
6	LEVELING FEET	4
7	BAR STEEL 4 x 0.5 in.	8'
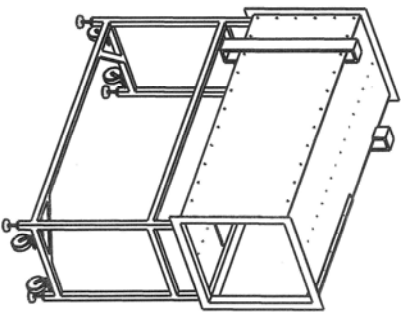
OKLAHOMA STATE UNIVERSITY

SCALE 0.021

EXPLODED TEST SECTION SET-UP

01/16/04

SCALE: 0.03

NOTE:
ALL DIMENSIONS IN INCHES
ALL TUBING: SQUARE 2 X 2 in.

OKLAHOMA STATE UNIVERSITY

Test Section Set-up

10/1/05   SCALE: 0.032

SCALE 0.018

7.75
37.83
95.44
36.38
36.38
60.84
95.19
3.50
30.16
36.00
56.00
36.00

NOTE:
ALL PANELS ARE ACRYLIC

2.8125
1.50
9.19375
8.375
8.375
94.9375
∅.40
1.81
37.125
.50
9.19375
1.8125
.31
1.50
3.3125
37.13

OKLAHOMA STATE UNIVERSITY
SIDE VIEWING PANELS
10/1/05
SCALE: 0.075
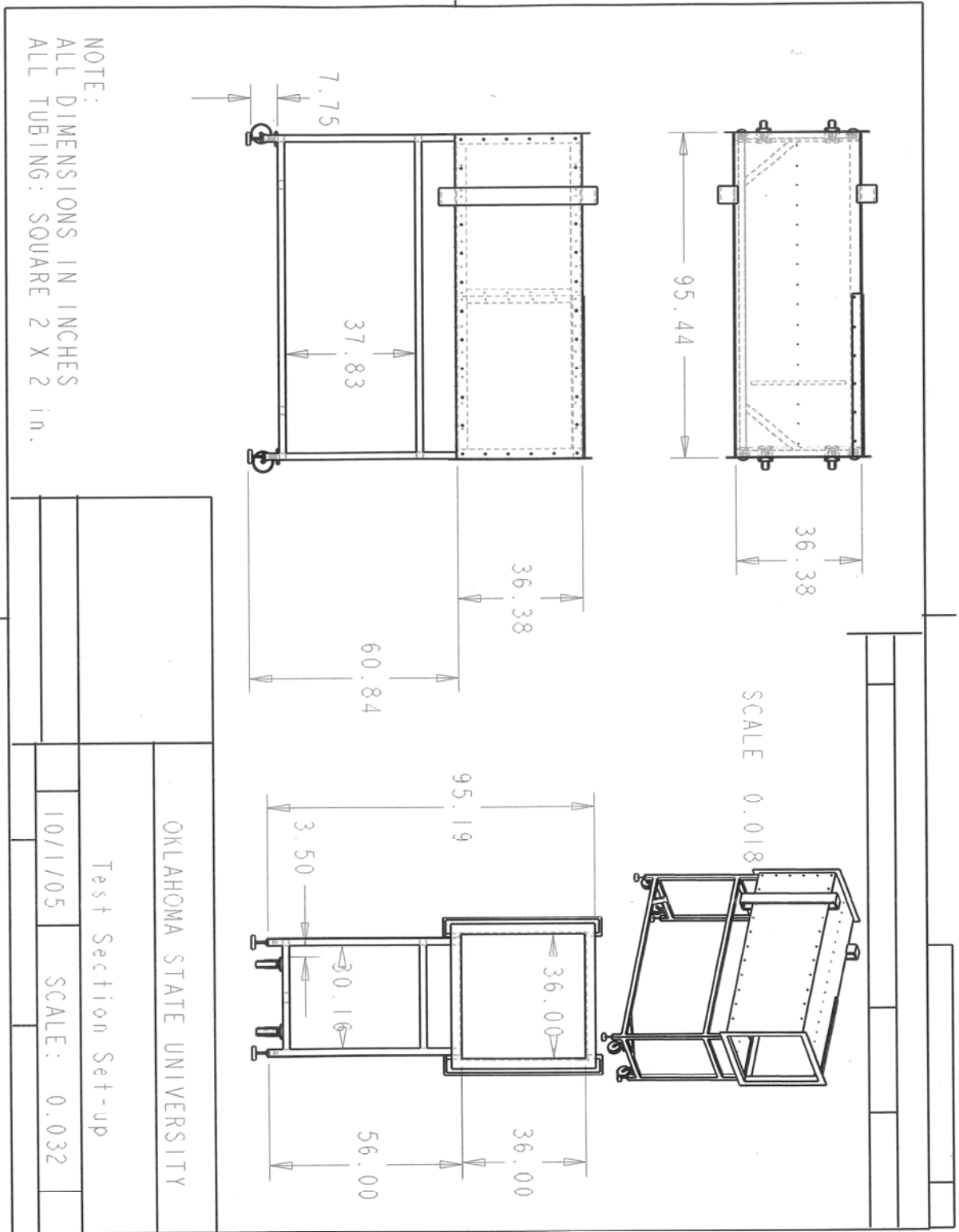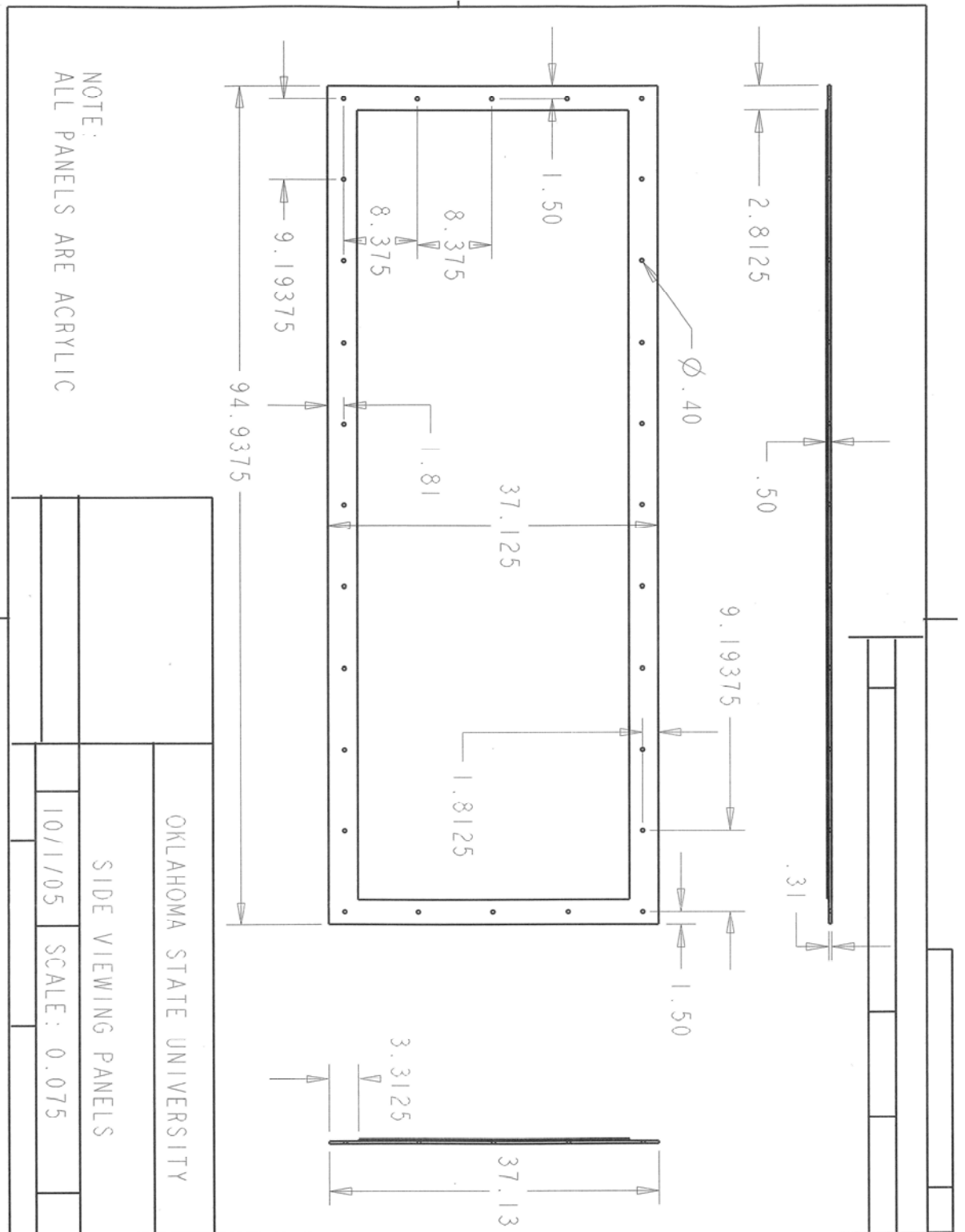
```
%Pressure Contour M-file

clear all;
close all;
clc;
    fprintf ( 1, '\n' );
    fprintf ( 1, 'VELOCITY CONTOUR \n' );
    fprintf ( 1, '\n' );
    file = input('Enter Excel File Name: ','s');
    fprintf ( 1, '\n' );
    squaresweepsize = input('Enter Square Sweep Size: ');
A=xlsread(file);

x=(A(1:squaresweepsize^2,1));
y=(A(1:squaresweepsize^2,2));
z=(A(1:squaresweepsize^2,3));

XI=0:1:(squaresweepsize);
YI=0:1:(squaresweepsize);
ZI=griddata(x,y,z,XI,YI');

hold on

pcolor(XI,YI,ZI);
shading interp;
axis equal;
xlabel('X position');
ylabel('Y position');
title('Velocity Distribution');

colorbar;

min1=min(z);
max1=max(z);
conts=min1:.1:max1;
contour(XI,YI,ZI,conts,'k');
axis equal;
```
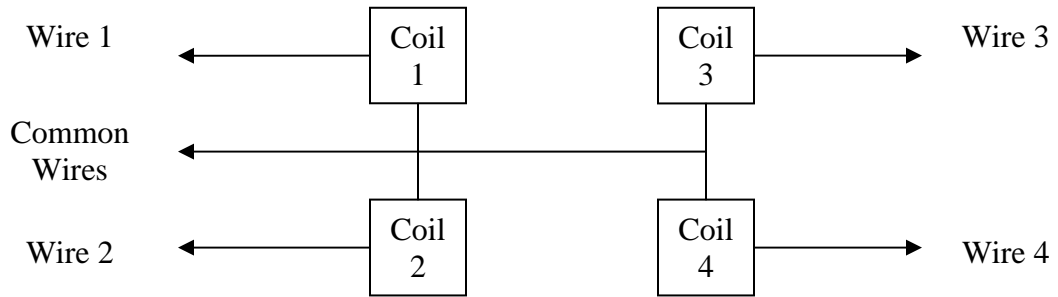
Stepping Sequence:
The armature of the shaft is between the four coils, so Figure 70 shows the setup in easier terms, where you can think of the logic as active low. You feed the power (6 volts) to the two common wires and simply ground the coils in sequence to step the motors.
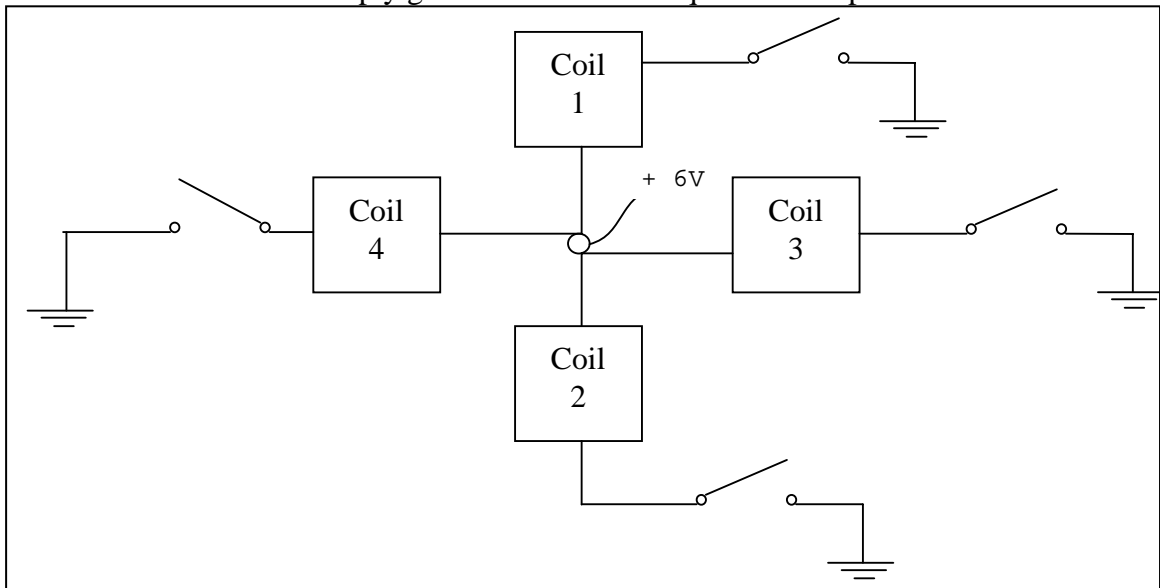
Figure 70. "Ground to Excite" schematic of our 4-phase stepper sequence.

The four wires when energized in the correct sequence causes the rotor to move in the clockwise direction. The exact reverse sequence gives counter clockwise rotation.
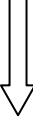
	Step	Coil1	Coil 3	Coil 2	Coil 4
Clockwise Rotation ⇓	1	**1**	0	0	0
	2	0	**1**	0	0
	3	0	0	**1**	0
	4	0	0	0	**1**
	5	**1**	0	0	0
	6	0	**1**	0	0
	7	0	0	**1**	0
	8	0	0	0	**1**

Table 2.   Single step coil excitation pattern.

NOTE: All grounds tied together ⏚

R1 = 47 Ω
R2 = 330 Ω
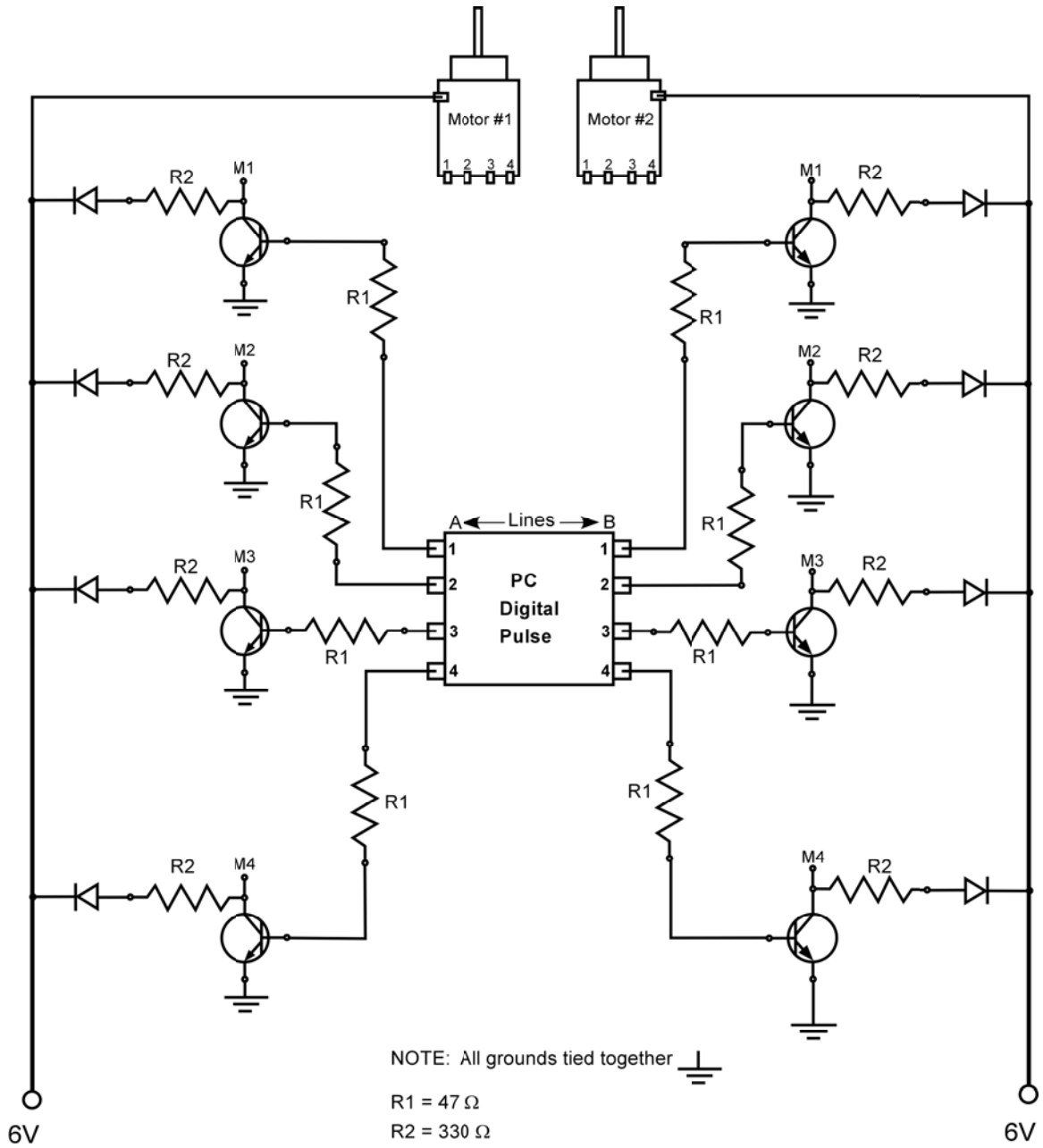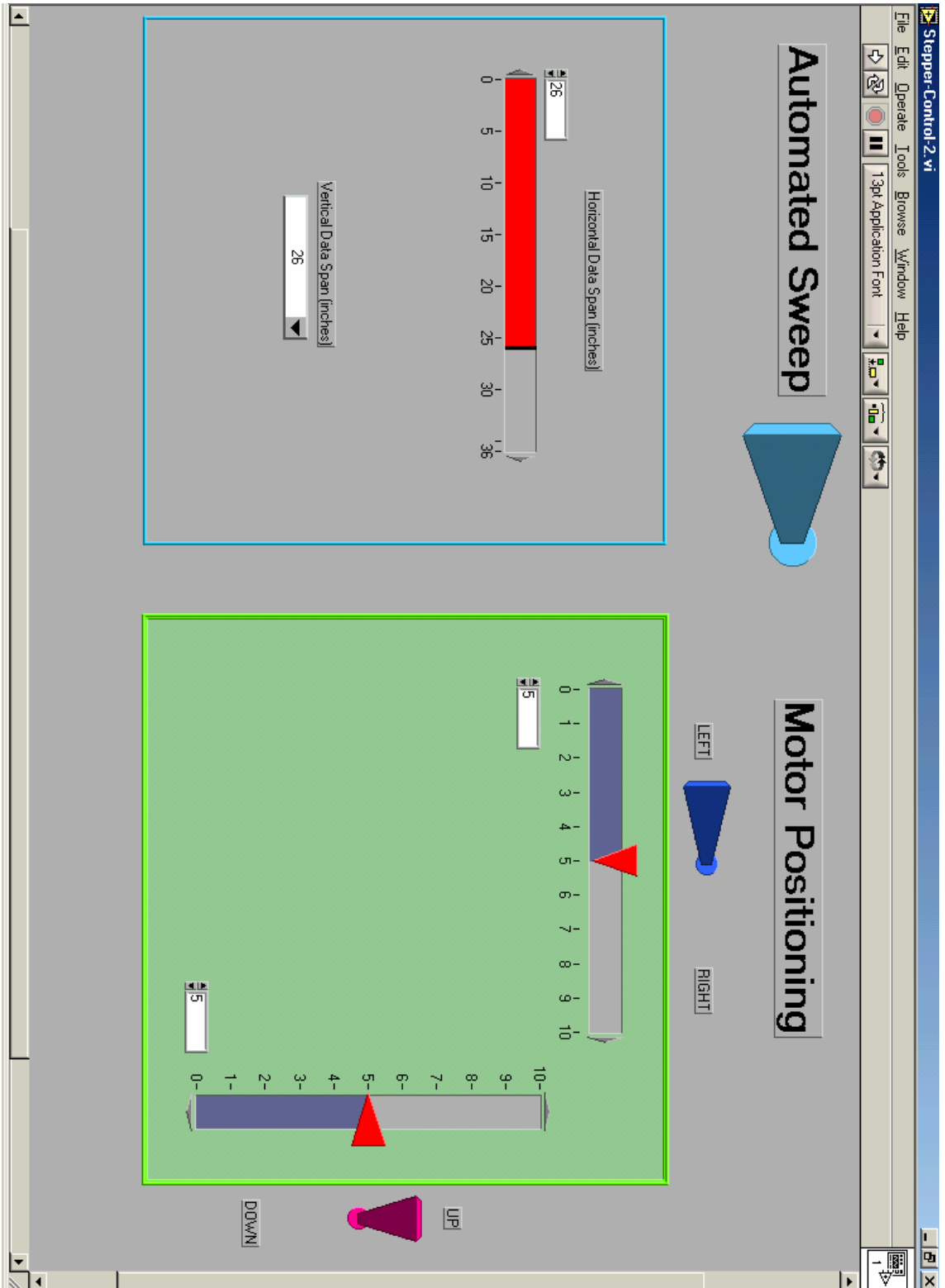
APPENDIX F—PITOT TUBE PRESSURE UNCERTAINTY

Validyne DP45-18 Very Low Differential Pressure Transducer with a pressure range of: $0 \leq \Delta p \leq 2.22 \ in - H_2O$.

$$v_1 = \sqrt{\frac{2(p_s - p_1)}{\rho}} = U_o$$

Performance Property	Specification
Capacity	$0 \leq \Delta p \leq 2.22 \ in - H_2O$
Rated Output	$25 \ mv/V$
Accuracy: Including linearity, hysteresis, and repeatability	0.5% FS

Pressure Calibration:
$P_{Pa} = 34.1(V) - 2.75$

Near the maximum tested pressure range $U = 9.84 \ m/s \ \rightarrow \ V = 1.74 volts$

$$P_{Pa} = 34.1(1.74) - 2.75 \ = \ 56.7 Pa$$

$$V_{AD} = 1.74 \pm \frac{1}{2^{12}} V \ = \ 1.74 \pm 0.000244 \ V$$

$$V_{nonlin} = 1.74 \pm 0.5\% \ = \ 1.74 \pm 0.0087 \ V$$

$$P_{10^\circ \ yaw} = (P_{Pa})0.5\% \ = \ 0.284 \ Pa$$

$$\omega_P = \left[\left(\frac{\partial P_{Pa}}{\partial V} \right)^2 (\omega_{AD} + \omega_{nonlin})^2 \right]^{\frac{1}{2}} + P_{10^\circ \ yaw}$$

$$\omega_P = \left[(34.1)^2 \left(244 \times 10^{-6} + 8.7 \times 10^{-3} \right)^2 \right]^{\frac{1}{2}} + 0.284$$

$$\omega_P = (0.305 + 0.284) \ Pa \quad = \quad 0.588 \ Pa$$

The percent uncertainty of dynamic pressure from the pitot static tube at a yaw angle of $10°$ is $\left(\dfrac{0.588}{56.7} \right) 100 = 1.04\%$. The maximum experimental pressure readings taken at the upper limit can be expressed as $P_{Pa} = 56.7 \pm 0.588 \ Pa$

Velocity Uncertainty

$$U = \sqrt{\frac{2 \left(p_{tot.} - p_{static} \right)}{\rho}}$$

$$where: p_{dyn.} = p_{tot.} - p_{static}$$

$$P_{Pa} = p_{dyn.}$$

$$U_{nom} = \sqrt{\frac{2 \left(56.7 \frac{kg-m}{m^2-s^2} \right)}{1.17 \ ^{kg}\!/_{m^3}}} = 9.84 \ \tfrac{m}{s}$$

$$U_{max} = \sqrt{\frac{2 \left(57.3 \frac{kg-m}{m^2-s^2} \right)}{1.17 \ ^{kg}\!/_{m^3}}} = 9.90 \ \tfrac{m}{s}$$

$$\omega_{U_\infty} = \Delta U = 0.051 \tfrac{m}{s}$$

The maximum experimental velocity readings taken for this experiment can be expressed as $U_\infty = 9.84 \pm 0.051 \tfrac{m}{s}$

```
%Cross-Power-Spectrum Analysis

clear all, close all, clc;
SampleRate=500;

%A=xlsread('freq__sine_test');
%A=xlsread('freq__1_D0_025');
%A=xlsread('freq__1_D0_0275');
%A=xlsread('freq__1_D0_045');
%A=xlsread('freq__1_D0_06');
%A=xlsread('freq__1_D0_07');
%A=xlsread('freq__1_D0_08');
%A=xlsread('freq__1_D0_09');
%A=xlsread('freq__1_D0_1');
%A=xlsread('freq__1_D0_125');
%A=xlsread('freq__1_D0_14');
%A=xlsread('freq__1_D0_15');
%A=xlsread('freq__1_D0_17');
%A=xlsread('freq__1_D0_185');
%A=xlsread('freq__1_D0_2');
%A=xlsread('freq__1_D0_215');
%A=xlsread('freq__1_D0_23');
%A=xlsread('freq__1_D0_245');
%A=xlsread('freq__1_D0_245-2');

%A=xlsread('cook_d_05-onset');
%A=xlsread('cook_d_06');
%A=xlsread('cook_d_08');
%A=xlsread('cook_d_1');
%A=xlsread('cook_d_12');
%A=xlsread('cook_d_14');
%A=xlsread('cook_d_16');
%A=xlsread('cook_d_18');
%A=xlsread('cook_d_21');
%A=xlsread('cook_d_24');
%A=xlsread('cook_d_27');
%A=xlsread('cook_d_30');
%A=xlsread('cook_d_33');
%A=xlsread('cook_d_36');
%A=xlsread('cook_d_39');
%A=xlsread('cook_d_42');
%A=xlsread('cook_d_45');
A=xlsread('cook_d_48');

x1=A(1:32768,1)';
x2=A(1:32768,2)';
```

```
n=length(x1);
%Put data through hanning window

%Initialize the vector
freqvect = linspace(0,n-1,n);

%Calculate the hanning funtion
vHanningFunc = .5*(1-cos(2*pi*freqvect/(n-1)));

%Output the result
x1 = x1.*vHanningFunc;
x2 = x2.*vHanningFunc;


y1=fft(x1);
dc=y1(1);
y1=2*y1(2:(n/2)+1);
y1=cat(2,dc,y1);

m1=abs(y1)*sqrt(8/3)/n;
p1=unwrap(angle(y1));

y2=fft(x2);
dc=y2(1);
y2=2*y2(2:(n/2)+1);
y2=cat(2,dc,y2);

m2=abs(y2)*sqrt(8/3)/n;
p2=unwrap(angle(y2));

DataLimit = (n/2)+1;
dfreq = ((0:n)*(SampleRate/n));   %freq. resolution

dfreq = dfreq(1:DataLimit);
m1 = m1(1:DataLimit);
p1=p1(1:DataLimit);

m2 = m2(1:DataLimit);
p2=p2(1:DataLimit);

subplot(2,2,1)
plot(dfreq,m1)

title('Vibometer near Leech');
    xlabel('Frequency (Hz)');
    ylabel('Amplitude');

    subplot(2,2,3);
    plot(dfreq,p1*180/pi)

    ylabel('Phase (deg)');
    xlabel('Frequency (Hz)');
```

```
subplot(2,2,2)
plot(dfreq,m2)

title('Vibometer near Pole (Luff)');
    xlabel('Frequency (Hz)');
    ylabel('Amplitude');

    subplot(2,2,4);
    plot(dfreq,p2*180/pi)

    ylabel('Phase (deg)');
    xlabel('Frequency (Hz)');

%-------------------------------------------------------------

Cross=(y2.*conj(y1))/n^2;  % Cross power Spectrum
m3=abs(Cross);
p3=unwrap(angle(Cross));

figure (2)
subplot(2,1,1)
plot(dfreq,m3)

title('Cross Power Spectrum Full Spectrum (Luff X Leech)');
    xlabel('Frequency (Hz)');
    ylabel('Amplitude');

    subplot(2,1,2);
    plot(dfreq,p3*180/pi)

    ylabel('Phase (deg)');
    xlabel('Frequency (Hz)');

    [Mag,i]=max(m3(1:(length(Cross))));

    index=i;
        Dominant_Frequency=dfreq(index)
        Phase_angle=p3(index)*180/pi
 index2=index+10;
      [Amp,location]=max(m3(index2:length(Cross)));

location=location+index2;
        Second_Mode=dfreq(location)
        Second_Mode_Phase_angle=p3(location)*180/pi

        index3=location+10;
      [Amp,location2]=max(m3(index3:length(Cross)));

location3=location2+index3;
        Third_Mode=dfreq(location3)
        Third_Mode_Phase_angle=p3(location3)*180/pi
```

```
              index4=location3+10;
         [Amp,location4]=max(m3(index4:length(Cross)));
            location5=location4+index4;
           Fourth_Mode=dfreq(location5)
           Fourth_Mode_Phase_angle=p3(location5)*180/pi


output=[dfreq(index),p3(index)*180/pi,dfreq(location),p3(location
)*180/pi,Third_Mode,
Third_Mode_Phase_angle,Fourth_Mode,Fourth_Mode_Phase_angle]

x1=A(1:32768,1);
x2=A(1:32768,2);
n=length(x1);

avg_x1=mean(x1);
avg_x2=mean(x2);
max_x1=max(x1);
max_x2=max(x2);
min_x1=min(x1);
min_x2=min(x2);

x1=x1.^2;
x2=x2.^2;
x1=(1/SampleRate).*x1;
x2=(1/SampleRate).*x2;
x1=sum(x1);
x1=(1/(n-1))*x1;
x2=sum(x2);
x2=(1/(n-1))*x2;
rms_x1=sqrt(x1);
rms_x2=sqrt(x2)  ;

output2=[avg_x1,avg_x2,max_x1,max_x2,min_x1,min_x2,rms_x1,rms_x2]

    figure (3)
    subplot(2,1,1)
plot(dfreq,m3)
axis([0 25 0 max(m3)+.0025])
title('Cross Power Spectrum (5.27 m/s)');
    xlabel('Frequency (Hz)');
    ylabel('Amplitude');
    gtext(strcat(' \omega_1=',num2str(dfreq(index)), 'Hz  at
\phi = ' ,num2str(p3(index)*180/pi), ' deg' ));

    subplot(2,1,2);
    plot(dfreq,p3*180/pi)
    ylabel('Phase (deg)');
    xlabel('Frequency (Hz)');
    axis([0 25 min(p3)*180/pi-50 max(p3)*180/pi+50])
       %-------------------------------------------
```
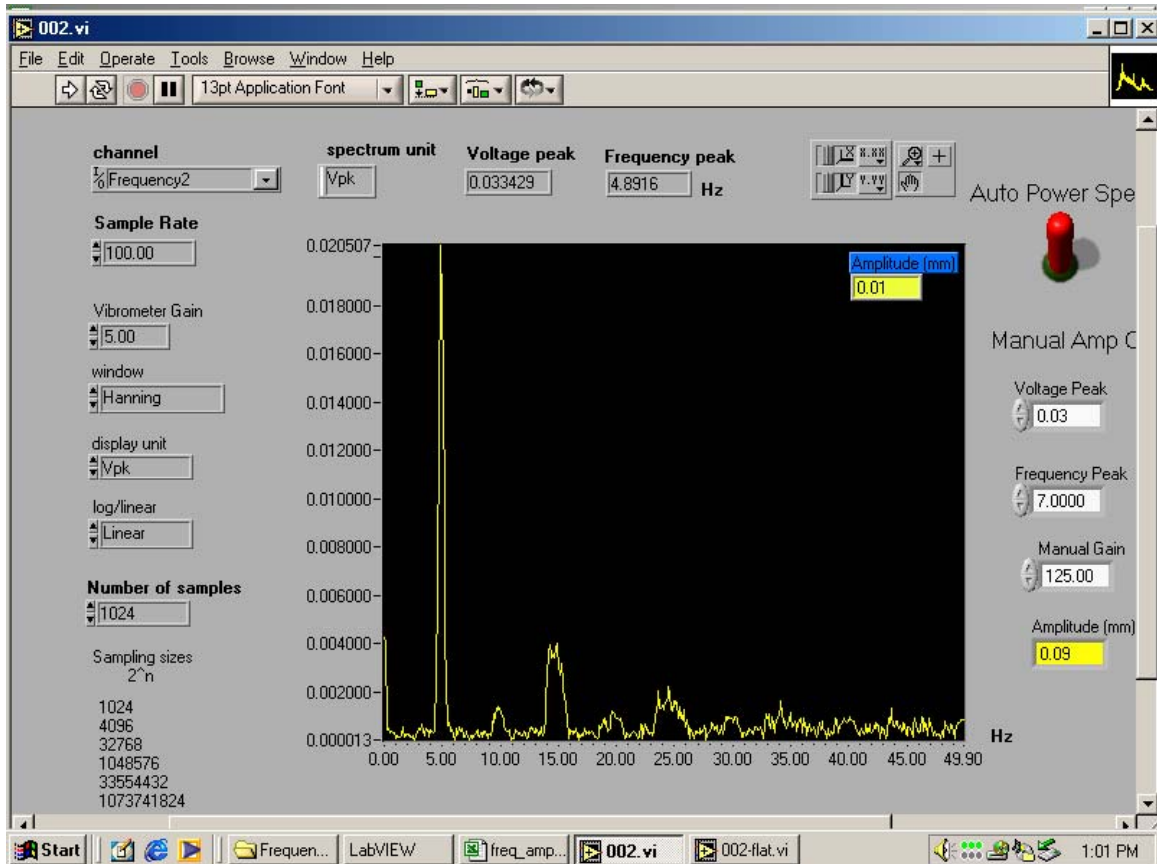
APPENDIX I—EXCEL SHEET AIR PROPERTY CALCULATOR

LAB AIR PROPERTY CALCULATION PROGRAM							
For Princo Barometer							
Enter PMM and TC only							
PARAMETER		VALUE	UNITS				
Uncorrected Barometer Reading	PMM	730.40	mm Hg			Inputs	
Temperature	TC	23.70	C				
Temperature Correction	CT	-2.82	mm Hg				
Barometer, Temp. Corrected	HT	727.58	mm Hg				
Latitude Correction	CG	-0.62	mm Hg				
Corrected Barometer Reading	HL	726.96	mm Hg				
Local Pressure	PATM	9.6920E+04	Pa			Outputs	
Absolute Temperature	TK	296.85	K				
Density	RHO	1.13761	kg/m3				
Dynamic Viscosity	μ	1.8311E-05	Pa-s				
Kinematic Viscosity	ν	1.6096E-05	m2/s				
Speed of Sound	C	345.36	m/s				
Molecular Mean Free Path	λ	6.9481E-08	m				
CONSTANTS							
Sutherland B	B	1.4580E-06					
Sutherland S	S	1.1040E+02					
Gas Constant for Air	R	287.0000					
Specific Heat Ratio	γ	1.400					
Acceleration of Gravity	g	9.80665E+00					
Density of Water	ρH2O	9.9800E+02					
Density of Mercury	ρHg	1.3595E+04					
Kelvin Conversion	CK	273.15					
Standard h	HZ	760.0					
Correction Constant, L	CL	1.8400E-05					
Correction Constant, M	CM	1.8180E-04					
Reference Temperature, Tm	TM	0.0					
Reference Temperature, Ts	TS	0.0					
Stillwater Latitude	ϕ	36.15					
	2ϕ (rad)	1.2619					

CALCULATION OF LABORATORY AIR PROPERTIES AS PERFORMED IN *AIRXLCOR.XLS*

CALCULATION OF ATMOSPHERIC PRESSURE

$$p_{atm} = \rho_{Hg} g h_{barometer} \qquad [\text{Pa} = \text{N/m}^2]$$

CALCULATION OF AIR DENSITY (dry ideal gas)

$$\rho_{air} = \frac{p_{atm}}{R T_{absolute}} \qquad [\text{kg/m}^3]$$

CALCULATION OF DYNAMIC AND KINEMATIC VISCOSITY OF AIR (Sutherland Equation)

$$\mu_{air} = \frac{b\sqrt{T_{absolute}}}{\left[1+\left(\dfrac{S}{T_{absolute}}\right)\right]}$$

$$b = 1.458E-06\frac{kg}{m-s-K^{1/2}} \qquad [\mu_{air} \text{ in Pa-s, } \nu_{air} \text{ in m}^2\text{/s}]$$

$$S = 110.4K$$

$$\nu_{air} = \frac{\mu_{air}}{\rho_{air}}$$

CALCULATION OF SPEED OF SOUND IN AIR

$$a = \sqrt{\gamma R T_{absolute}} \qquad [\text{m/s}]$$

CALCULATION OF "MOLECULAR" MEAN FREE PATH OF AIR

$$\lambda_{air} = \frac{1.26\nu_{air}\sqrt{\gamma}}{a} \qquad [\text{m}]$$

Knudsen Number $\quad Kn = \dfrac{\lambda_{air}}{L_{characteristic}}$

Kn << 1 for continuum flow

TEMPERATURE CORRECTION OF BAROMETER READING

$$C_t = h_t - h_r = h_r \left[\frac{1 + L(t - t_s)}{1 + M(t - t_m)} - 1 \right]$$

LOCAL GRAVITY CORRECTION OF BAROMETER READING

$$C_g = h_l - h_t = h_t \left\{ \frac{980.616}{980.665} [1 - 0.0026373 \cos(2\phi) + 0.0000059 \cos^2(2\phi)] - 1 \right\}$$

WHERE:

h_l	=	**Local Station Pressure Reading**
h_0	=	**Standard Pressure Reading at Sea Level**
h_r	=	**Uncorrected Barometer Reading**
h_t	=	**Temperature Corrected Barometer Reading**
t	=	**Temperature**
ϕ	=	**Latitude (Stillwater Latitude = 36.15 degrees)**

Parameter	SI	English
h_0	760 mm	29.921 in.
L	0.0000184 m/m °C	0.0000102 in./in. °F
M	0.0001818 m³/m³ °C	0.0001010 in.³/in.³ °F
t_m	0 °C	32 °F
t_s	0 °C	62 °F
g	9.806650 m/s²	
ρ_{Hg}	13.595 x 10³ kg/m³	

LOCAL ATMOSPHERIC PRESSURE

$$p_{atm} = \rho_{Hg} g h_l$$

REFERENCE
"Instruction Booklet for Use with Princo Fortin Type Mercurial Barometers," Princo Instruments, Inc., Southampton, Pa., 1983.

Acrylic Test Section Pitot Sweep-- Recall that the each pressure profile presented below was performed over a square 26x26 in. area, leaving a 5 in. un-swept space between the reported edge results and the actual tunnel wall. In general, there was found to be a pressure increase from the bottom of the tunnel to the top. Results will show, that taping the pitot traverse slot will reduce this gradient. Additionally, it appears as if the left side of the tunnel has a higher pressure region than the right side. This could possible be the result of the inlet suction configuration, where air is required to turn a left hand corner as it enters the diffuser. Air has to travel faster on the right side (to make the turn) and may explain the lower pressure trend on the right half of the swept profiles. In general, the tunnel profiles are fairly uniform, where pressure differences are quite small.
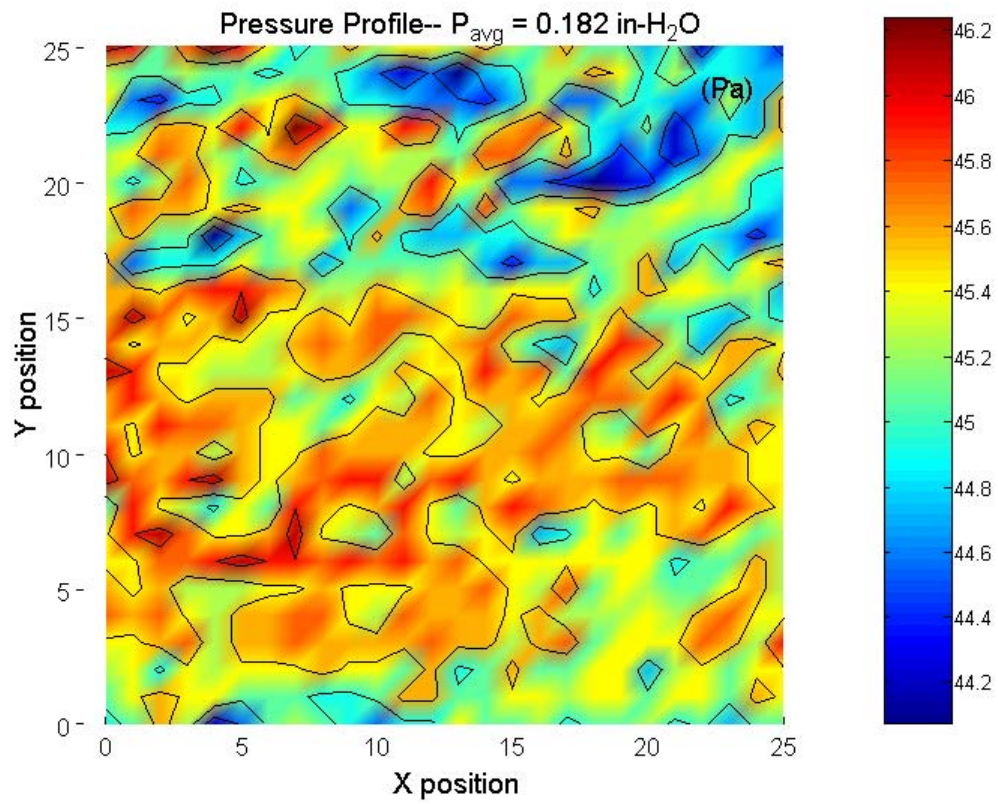
$$Supply: \quad P_{avg} = 0.083 \; in - H_2 0 \; = \; 20.64 \; Pa \; = \; 5.94 \; \frac{m}{s} \; = \; 11.55 \; knots \; = 25.84 mph$$

$$\Delta P_{max} = 3.17 \; Pa \;\; , \;\; \Delta U_{max} = 0.460 \; \frac{m}{s} \; = \; 7.7\%$$

Pressure Profile-- P_{avg} = 0.083 in-H_2O
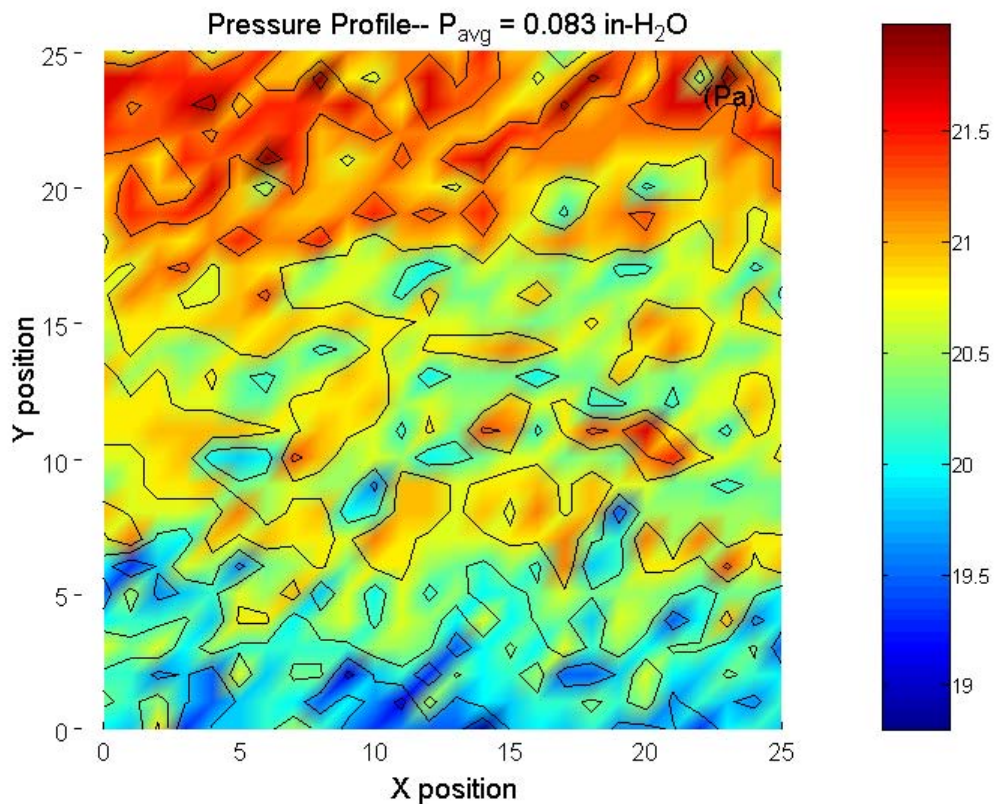
$Supply: \quad P_{avg} = 0.182 \; in - H_20 \;\; = \;\; 45.32 \; Pa \;\; = \;\; 8.68 \; m/s = 16.87 \; knots \;\; = \;\; 19.41 \; mph$

$\Delta P_{\max} = 2.16 \; Pa \;\; , \;\; \Delta U_{\max} = 0.207 \; m/s \;\; = \;\; 2.4\%$

$Supply: \quad P_{avg} = 0.355 \; in-H_2O \;\; = \;\; 88.37 \; Pa \;\; = \;\; 12.07 \; ^m\!/_s \;\; = \;\; 23.46 \; knots \;\; = \;\; 27.00 \; mph$

$\Delta P_{max} = 2.67 \; Pa \;\; , \;\; \Delta U_{max} = 0.183 \; ^m\!/_s \;\; = \;\; 1.5\%$
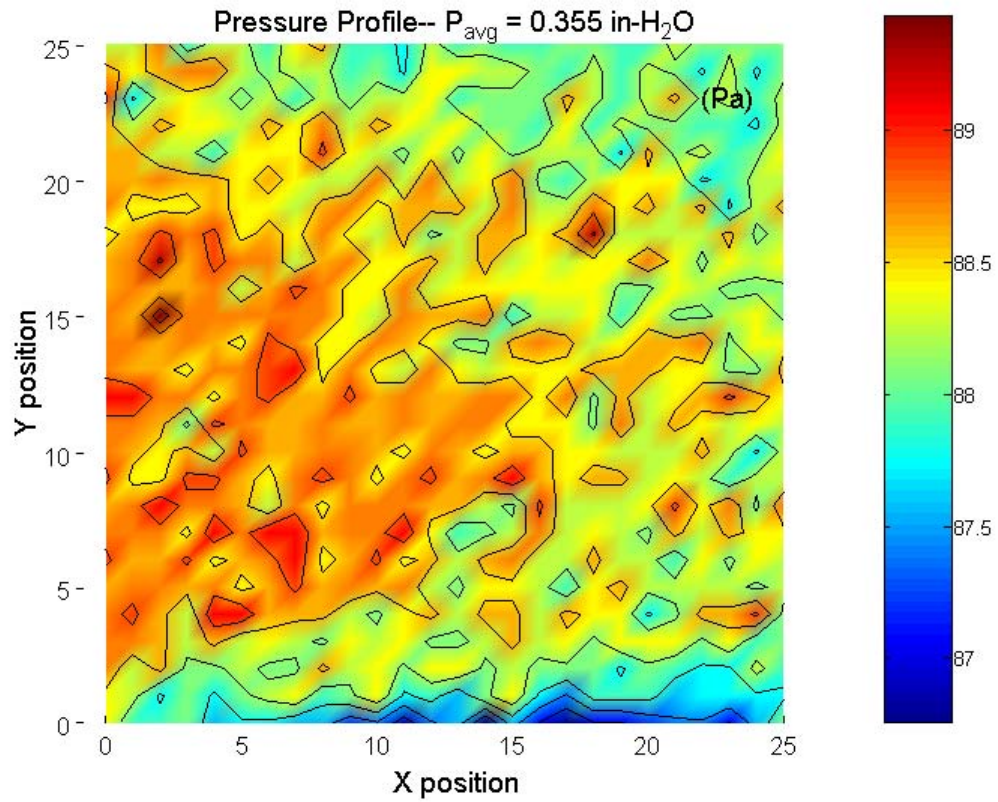
$Supply: \quad P_{avg} = 0.541 \; in - H_2 0 \;\; = \;\; 134.82 \; Pa \;\; = \;\; 15.07 \; {}^{m}\!/_{s} \;\; = \; 29.29 \; knots \;\; = \;\; 33.7 \; mph$

$\Delta P_{max} = 4.17 \; Pa \;\;\;, \;\; \Delta U_{max} = 0.233 \; {}^{m}\!/_{s} \;\; = \;\; 1.5\%$

Pressure Profile-- P_{avg} = 0.541 in-H_2O
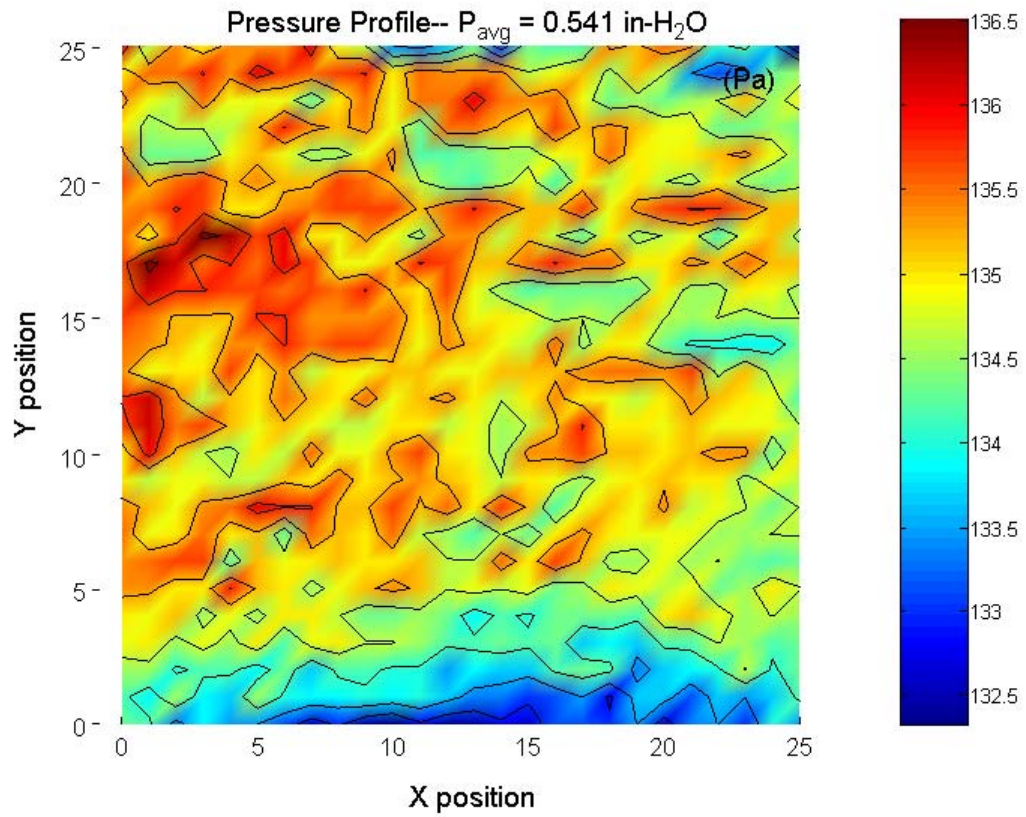
$Supply: \quad P_{avg} = 0.735 \ in-H_2O \ = \ 182.92 \ Pa \ = \ 17.65 \ {}^m\!/_s \ = \ 34.31 \ knots \ = \ 39.5 \ mph$

$\Delta P_{max} = 5.68 \ Pa \ , \ \Delta U_{max} = 0.275 \ {}^m\!/_s \ = \ 1.6\%$
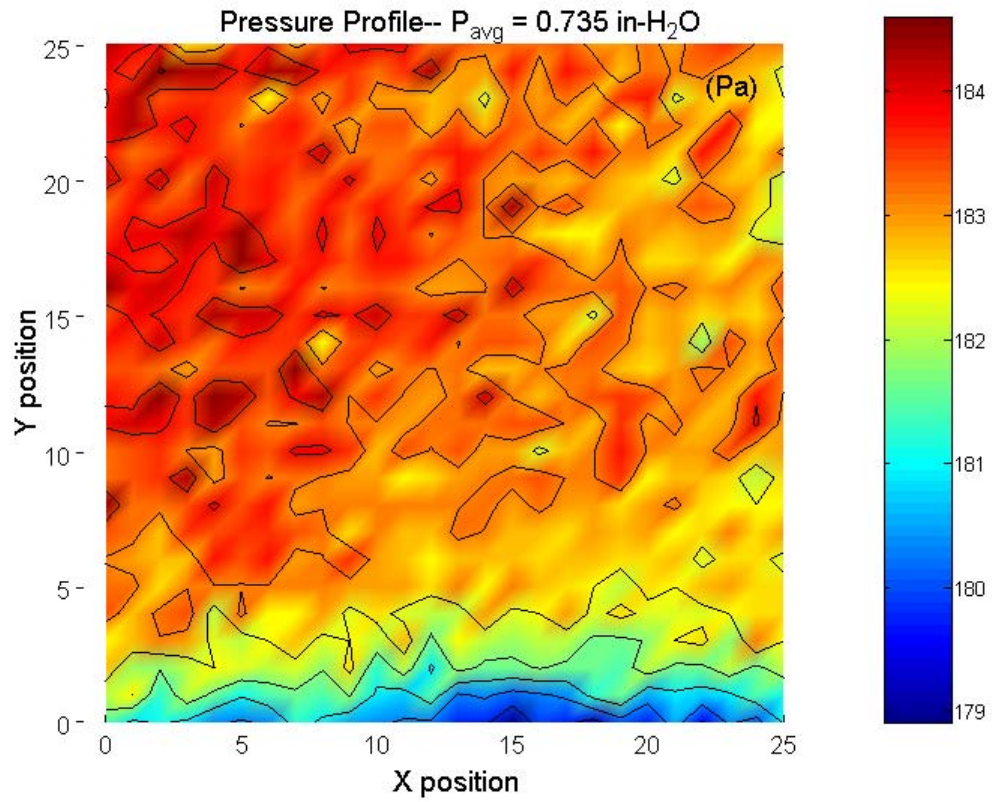
$$Supply: \quad P_{avg} = 0.976 \, in - H_2 0 \; = \; 243.1 \, Pa \; = \; 20.52 \, \dfrac{m}{s} \; = \; 20.52 \, knots \; = \; 39.89 \, mph$$

$$\Delta P_{max} = 9.52 \, Pa \;\; , \;\; \Delta U_{max} = 0.403 \, \dfrac{m}{s} \; = \; 2.0\%$$

Pressure Profile-- P_{avg} = 0.976 in-H_2O
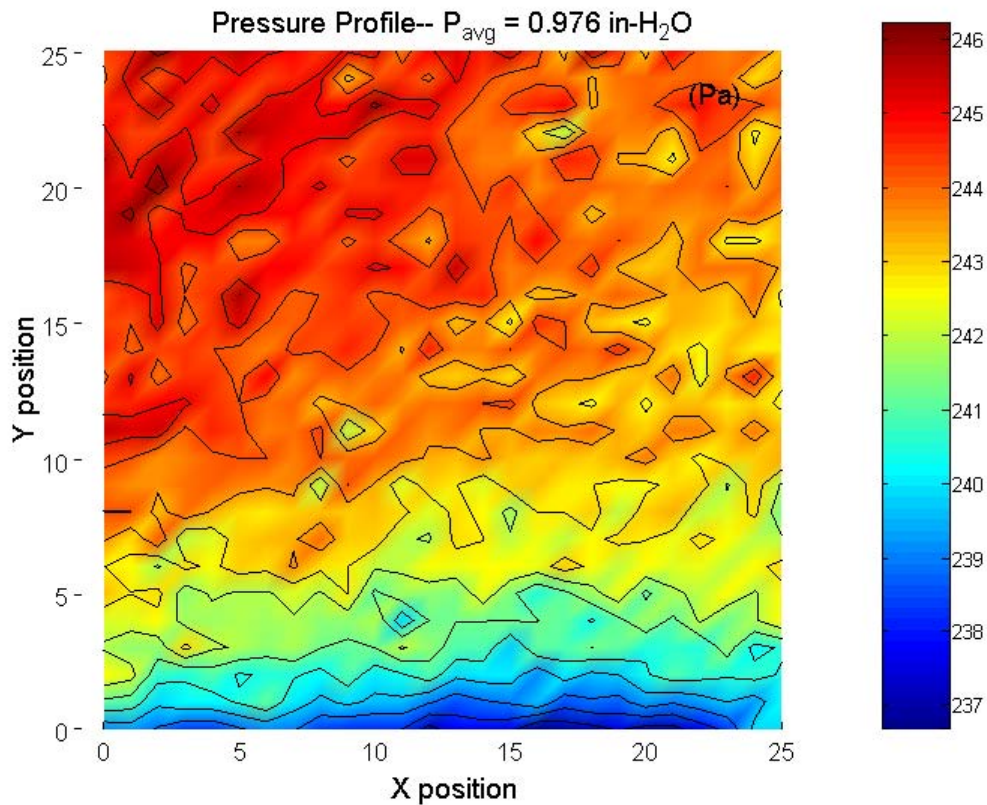
After seeing a consistent pressure gradient trend from multiple free stream pressure profiles. The pitot tube was aligned in the center of the tunnel, and the pitot tube slot (that allowed horizontal translation) was taped, and a vertical traverse (pressure profile) was performed. To ensure that the pressure from outside of the tunnel was not disrupting the flow inside the tunnel, and to eliminate the concern of the pressure drop coming from the sharp edge contact of the slot or foam protrusions the slot was taped on the inside of the tunnel. This test was performed with the same level detail as previous

profile tests, where equipment was given over an hour to stabilize, and the room was brought to temperature (tunnel turned on for 30 min. at desirable velocity before data collection began) before the test was run. The result of this vertical profile was taken at $\left(p_{avg} = 0.738 \ in - H_2O \right)$ supply pressure and is shown in Figure 71. Results indicates a pressure increase from the bottom to top of the tunnel. The pressure gradient is quite small, but it does exist.
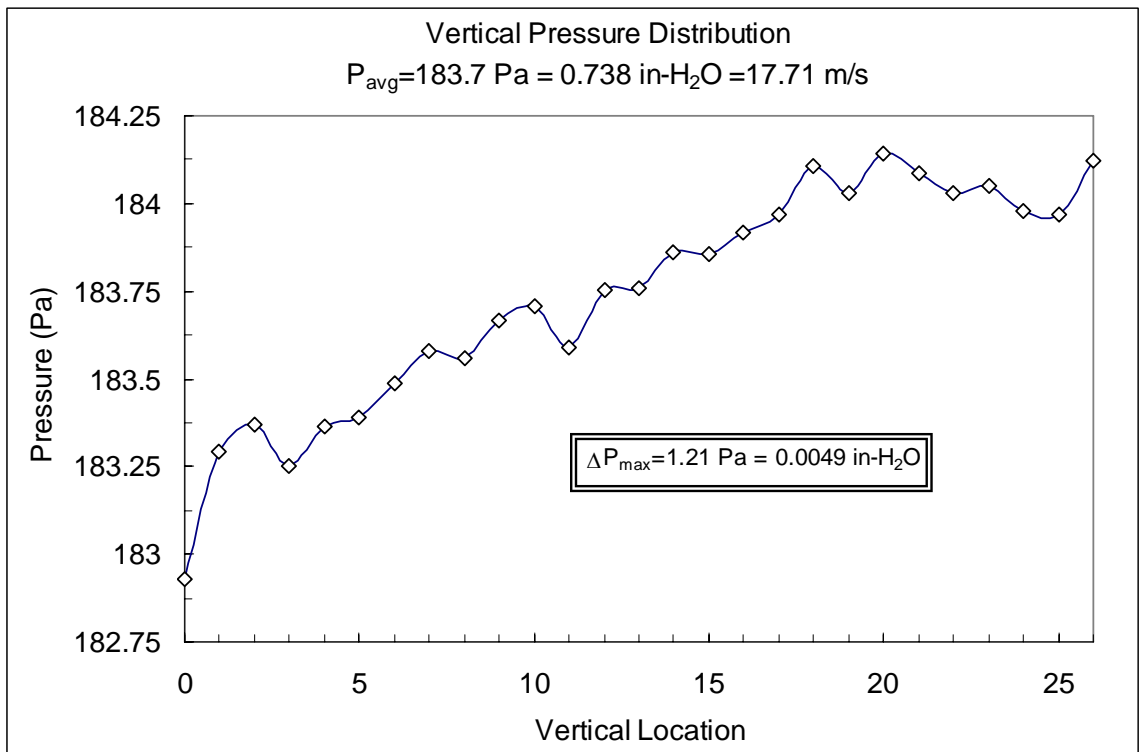

Figure 71. Vertical pressure distribution

Comparing the vertical pressure distribution along the center section for the sweep run at $P_{avg} = 0.735 \ in - H_2O$ indicated that the tape does, in fact reduce the

pressure gradient. Figure 72 shows the both vertical pressure profiles with the maximum

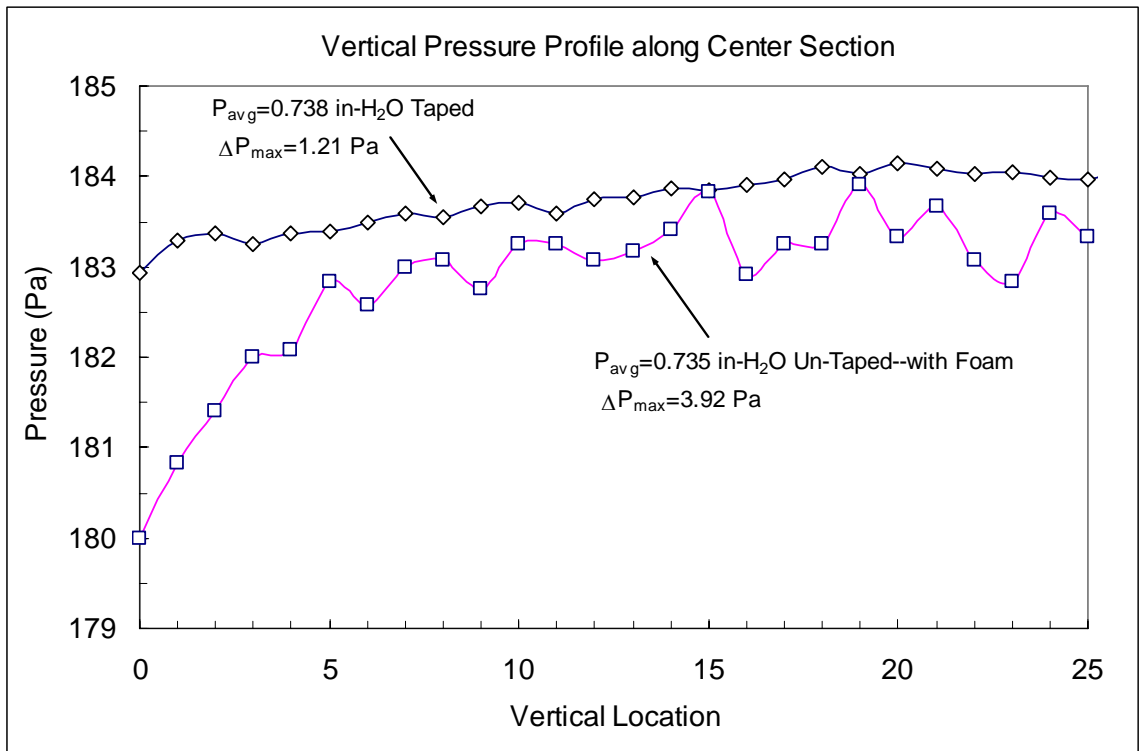pressure difference given in the plot.

Figure 72. Effect of vertical pressure profile from taping pitot slot

VITA

Adam Martin

Candidate for the Degree of

Master of Science

Thesis:
   EXPERIMENTAL STUDY OF DRAG FROM A FLUTTERING FLAG

Major Field: Mechanical Engineering

Biographical:

Personal Data:
   Born in Rapid City, South Dakota, On February 15, 1981, the son of Jeff and Debbie
   Martin.

Education:
   Completed Bachelor of Science degree in Mechanical Engineering Technology from
   Oklahoma State University, Stillwater, Oklahoma in May 2003. Completed the
   requirements for a Master of Science degree with a major in Mechanical Engineering
   at Oklahoma State University in May 2006.

Professional Experience:
   Graduate Research Assistant\Teaching Assistant, School of Mechanical and
   Aerospace Engineering, Oklahoma State University, 2001 to 2006; Honda Research
   & Development Americas, Summer 2005 Co-op, Vehicle Strength and Simulation;
   Halliburton Energy Services, Summer 2003 Intern, Mechanical Surface/Reliability
   Division.

Name: Adam Martin   Date of Degree: May, 2006

Institution: Oklahoma State University   Location: Stillwater, Oklahoma

Title of Study: EXPERIMENTAL STUDY OF DRAG FROM A
                          FLUTTERING FLAG.

Pages in Study: 136   Candidate for the Degree of Master of Science

Major Field: Mechanical Engineering

Scope and Method of Study:

The purpose of this study is to quantify the magnitude of induced drag force that results from a flexible material (flag) fluttering in air stream versus a stiff panel vane with identical dimensions. Wind tunnel experiments were performed to assess component lift and drag forces on both flexible and rigid vanes. Furthermore, a qualitative and quantitative analysis describing flutter modes are supported from waveform data including: frequency, phase, wavelength, and amplitude.

Findings and Conclusions:

As a result of flutter motion, centrifugal forces induce in-plane tension in the fabric. This tension acts to "flatten" the flag thereby opposing the fluid pressure forces which generate the out-of-plane curvature (motion). This dynamically induced tension is felt at the attachment point as increased drag force, above and beyond the magnitude of skin friction drag. It has been shown experimentally that the time-averaged drag depends only on the square of the velocity amplitude and the mass of the fluttering specimen. Experiments suggest that large centrifugal forces, because of large fabric curvature and low material stiffness can generate elevated drag over that of heavier, stiffer materials with identical dimensions. Furthermore, high speed photo data suggests flutter amplitudes are reduced at high wind velocities due to the induced in-plane tension. Additionally the makeup of flutter oscillations in a flexible flag were proven to consist of both traveling and standing waves. Standing wave ratio (SWR) approximations from superimposed photo data suggests an underlying dominance of traveling waves comprising the flutter motion.

ADVISER'S APPROVAL: _____Peter M. Moretti_____